Important Notice

UNIVERSITY OF CALGARY

Well-log validated waveform inversion of reflection seismic data

by

Sergio Jorge Romahn Reynoso

A THESIS

SUBMITTED TO THE FACULTY OF GRADUATE STUDIES

IN PARTIAL FULFILLMENT OF THE REQUIREMENTS FOR THE

DEGREE OF DOCTOR OF PHILOSOPHY

GRADUATE PROGRAM IN GEOLOGY AND GEOPHYSICS

CALGARY, ALBERTA

AUGUST, 2019

Abstract

This thesis develops, examines and refines the basic waveform inversion procedures of reflection seismic data under an alternative perspective that makes an effort to assign to each element of full-waveform inversion (FWI) workflow an element of standard seismic processing. The basic procedures can be summarized as an iterative cycle of modelling, migration and inversion. The modelling part was carried out with a fourth order finite-difference scalar acoustic algorithm, assuming a 2D medium governed by the constant density acoustic wave equation. The two-way wave operators (analogous to reverse-time migration), used as standard engine in FWI to produce the gradient, is replaced with one-way wave operators. The role of the pseudo-Hessian as a gradient preconditioner is substituted with a deconvolution imaging condition. A key element of this methodology is the incorporation of log information to calibrate the update direction (i.e., a well-log validation approach), rather than determining a scalar step-length with a line search (i.e., a data-validation approach). This inversion perspective leads to remarkably accurate results and significant computational savings. Once a well-log validated waveform procedure was set up, I evaluated the scope of well-log validation under several factors (such as geological complexity, well location, log interval, and well-data uncertainty) that may influence the performance of this technique due to the well-log limitation of providing punctual information. I also analyzed the repercussions that the seismic acquisition parameters, the random noise and a deficient initial model would have on the inversion. Having established pros and cons of well-log validated waveform inversion with one-way wave equation migration, I addressed the unknown-wavelet issue. A process of updating both the amplitude and phase of an initial wavelet estimate is set up to produce stable inversions in both synthetic and field environments. In the latter case, profiles extracted from a log-validated waveform inversion of the Hussar land data set, when compared to two blind validation wells, are observed to accurately reproduce structures in zones producing significant reflection energy.

Preface

The material in Chapters 4 and 5 was submitted to the Canadian Journal of Exploration and is currently under review; the material in Chapters 8 was likewise submitted to the journal Geophysics and is also currently under review. Some preliminary results discussed in Chapter 5 were presented at the SEG annual meeting 2017. The material in Chapters 3, 4, 5, and 8 was presented at the CSEG Geoconvention.

Acknowledgements

I wish to thank the sponsors of the Consortium for Research in Elastic Wave Exploration Seismology (CREWES) and NSERC (Natural Science and Engineering Research Council of Canada) through the grant CRDPJ 461179-13, whose financial support is crucial for our research activities.

This research wouldn't have been possible without the scholarship and financial support of the Government of Mexico through CONACYT (Consejo Nacional de Ciencia y Tecnologia) and PEMEX.

I have special gratitude to Dr. Kris Innanen for his supervision, guidance, unfailing encouragement, and invaluable support.

I would also like to thank Dr. Gary Margrave. He was always open for fruitful discussions and provided pertinent suggestions to my project.

Thanks to Dr. Larry Lines, Dr. Don Lawton and Dr. Daniel Trad for their insightful questions in the CREWES meetings.

I want to thank Dr. Sam Gray for his profound examination of the Thesis.

Many thanks to my mentor in PEMEX Damaso Contreras Tebar, who has always been an encouraging example. Thanks to Antonio Escalera Alcocer whose vision and effort to strengthen Pemex propitiated the undertaking of this research.

My sincere appreciation for the diligent proofreading of this thesis by Dr. Aida Cortes.

To my beloved Aida who has been a strong source of motivation and support.

To my loves Abril and Jeronimo who have grown at the rate of this research.

To my parents who have always been there when I need them the most.

Table of Contents

List of Figures and Illustrations

List of Tables

List of Symbols, Abbreviations and Nomenclature

Symbol or abbreviation	Definition
δ	Dirac delta
$\delta v_k^{(w)}$	Velocity residual in the well
$\mathbf{\Delta m}$	Model update or model perturbation
$\mathbf{\Delta p}$	Data residual
$\mathbf{\Delta R}$	Reflectivity residual
$\mathbf{\Delta v}$	Velocity perturbation
ΔU_r	Residual-upgoing receiver wavefield
ϵ	Small positive number
λ	Matched filter
μ	Scalar
η	Small positive contant
φ	Phase rotation angle
Φ	Update direction
∇	Laplace operator
ω	Angular frequency
a	Amplitude scalar
B	Bin size
D_s	Downgoing source wavefield
DR_{norm}	Data residual norm
e	Exponential
E	Objective function
$\mathbf{f}$	Forward modelling operator
f_{dom}	Dominant frequency
$\mathbf{F}$	Derivative operator
F	Fourier transform operator
FWI	Full waveform inversion
$\mathbf{g}$	Gradient
G	Green's function
$\mathbf{H}$	Hessian matrix
i	Complex number
I	Impedance
Im	Reflectivity image

$IMMI$	Iterative modelling, migration and inversion
$Imp(\cdot)$	Impedance inversion operator
k	Iteration number
$LVWI$	Well-log validated waveform inversion
$\mathbf{m}$	Model parameter
$\mathbf{m}_o$	Initial model parameter
M	Dimension of model
$Mig(\cdot)$	Migration operator
MO	Maximum offset
nr	Number of receivers
ns	Number of sources
NC	Number of channels or receiver stations
$\mathbf{p}_{cal}$	Modelled seismic data
$\mathbf{p}_{obs}$	Observed seismic data
$phsrot(\cdot)$	Phase rotation operator
$PSPI$	Phase-shift plus interpolation
R	Reflectivity
RI	Receiver interval
RMS	Root mean square
RTM	Reverse time migration
SI	Source interval
SN	Signal-to-noise ratio
$Stk(\cdot)$	Stack operator
t	Time vector
U_r	Upgoing receiver wavefield
v	Velocity
$v_k^{(w)}$	Model velocity in the well for iteration k
$v^{(w)}$	Well-log velocity
V_{int}	Interval velocity
x_r	Receiver location
x_s	Source location
z	Depth vector
$\cdot_{cc}$	Cross-correlation imaging condition
$\cdot_{dec}$	Deconvolution imaging condition
$\cdot^*$	Complex conjugation
$*$	Convolution operator

Chapter 1

Introduction

1.1 Background

Geophysics is defined by Sheriff (2002) as the study of the Earth by quantitative physical methods, especially by seismic reflection and refraction, gravity, magnetic, electrical and radiation methods. Its purpose is to map the distribution of physical property variations that characterize the geology, geological structure, groundwater, and certain artifacts of interest in the Earth's subsurface. The physical properties are remotely sensed using, most of the time, non-invasive technologies. Exploration geophysics is a sub-discipline that aims for resource exploration, i.e., prospecting petroleum and mineral accumulations. Nowadays, seismic exploration plays a relevant role in this matter and the reflection technique is the most widely used geophysical method in the oil and gas industry (Finkl, 1988). The capability of detecting large-to-small scale subsurface features contributes to the popularity of this method. The reflection seismic method provides an image of the subsurface in two or three dimensions. The basic principle to produce this image is generating, recording and analyzing seismic waves that travel through the Earth (Mondol, 2010). Common seismic sources are air-guns in marine surveys and vibrators or dynamite in land acquisition. The seismic pulse travels through the Earth, where the velocity and density changes reflect the waves back

to the surface. Receiver stations, spread through the surface, record the seismic signal that contains information about those velocity and density variations. The data acquired in this manner will be referred to as "observed shot records". The next step consists in processing the seismic shot records in order to enhance the signal, build the subsurface image, and extract as much information as possible about the property variations that give rise to the recorded data (Yilmaz, 2001). It is in the latter point where processing and interpretation merge and seismic inversion methods play an important role in this purpose.

Seismic inversion aims to find a model of the Earth using seismic measurements as input (Russell, 1988). This model should explain the features in the seismic data. Apprehending the physical process that originates the data is the first step to understand the inversion process. Forward modelling takes the Earth model as input and, through an algorithm that incorporates the physics of the phenomenon, predicts the seismic response. The inverse problem takes the seismic response as input and applies an algorithm that also involves the physics of the problem to generate the Earth model as output. The early seismic inversion techniques transformed the seismic data into P-impedance, i.e., the product of density and P-wave velocity. Lindseth (1979) showed that the impedance model can be obtained from the normal-incidence reflectivity by applying a recursive technique. He recognized that the band-limited wavelet, which removes the low and high frequency components of the reflectivity, limits resolution and the efficient recovery of the P-impedance model. This is a common problem in any type of seismic inversion. Starting from an accurate initial model that incorporates the missing low frequencies in the seismic data is essential for achieving satisfactory results. Another example of seismic inversion incorporates amplitude versus offset analysis, i.e., AVO (Ostrander, 1984; Castagna and Backus, 1993). AVO inversion is based on the linearized version of Zoeppritz equations (Aki and Richards, 2002; Fatti et al., 1994; Shuey, 1985), which describe the mode conversion of an incident P-wave at an angle θ into reflected and transmitted P-and-S waves. This inversion technique can produce density, P-wave and S-wave velocity models.

A different seismic inversion approach is referred to as full waveform inversion (FWI). The purpose of FWI is to infer the distribution of Earth properties in the subsurface by iteratively reducing data residuals, i.e., the differences between observed and synthetic seismic shot records (Virieux and Operto, 2009). Lailly (1983) proposed an inversion procedure constituted by a sequence of pre-stack migrations of the data residuals. Tarantola (1984) showed that the FWI gradient is produced from correlating the forward propagation of the actual sources and the backward propagation of the data residuals. The model update can be obtained by multiplying the gradient by a simple scalar. Virieux and Operto (2009) pointed out that the perturbation model looks like a migrated image obtained by reverse-time migration (RTM). The difference is that the data residual is back propagated in waveform inversion, whereas the recorded wavefield is back propagated in reverse time migration.

FWI has become an attractive topic in academia and industry because of its potential use in velocity model building and reservoir imaging, with some interesting applications especially in offshore environments (Minkoff and Symes, 1997; Shipp and Singh, 2002; Lee and Shin, 2015; Ray et al., 2016; Huang and Schuster, 2018). However, it faces some key remaining technical challenges, including the computational cost of applying it to large datasets, the fitting of model response to noise in data (inaccuracy of data recording not related to geology), as well as convergence issues originating in the incomplete nature of seismic data (Jackson, 1972). Furthermore, in onshore applications, additional challenges based on complex near-surface environments and irregular acquisitions, exist. One of the features of FWI that confers onto it both its power and its exposure to convergence issues, is that it is driven primarily by "data validation". I use this term because the two ingredients of a standard FWI update, namely (1) the gradient, which measures the direction of steepest descent towards the minimum of the norm of the difference between modelled and measured data, and (2) the step-length, which is usually computed by a further analysis of the error norm, are both derived from data misfit.

The alternative waveform inversion approach developed and implemented in this thesis is

based on the FWI workflow. The process has been reformulated following the iterative modelling migration and inversion (IMMI) concept of Margrave et al. (2012a). The philosophy of IMMI consists in recognizing mathematical aspects of FWI that correspond to standard seismic methodology, and replace them if possible with robust examples of standard algorithms. For instance, the gradient calculation is recognizable as the reverse-time migration of the data residuals with a cross-correlation imaging condition; Margrave et al. (2010, 2011b, 2012a) made the case that the two-way wave operators could be replaced by one-way migration operators, e.q., phase-shift plus interpolation migration, or PSPI (Gazdag, 1978; Gazdag and Sguazzero, 1984). A major strength of using PSPI is the natural accommodation of frequency selection strategies in a multiscale approach, e.g., Pratt (1999); Guarido de Andrade (2017). This is because, unlike RTM, PSPI migrates each frequency independently and its cost is directly proportional to how many frequencies are migrated. FWI preconditioning with the diagonal pseudo-Hessian (Shin et al., 2001b), for another example, produces updates similar to those generated by migration with a deconvolution-type imaging condition, and the latter could be used in place of the former. Well-log information is another element that can be incorporated in the waveform inversion process. The existence of well-log data allows including an additional stabilizing component in FWI, which can be referred to as "model-validation". Well logs can be used to support FWI in a number of ways, for instance, by assisting in the creation of accurate starting models (Chen et al., 2016). However, log information can also be more deeply incorporated in FWI, such that it becomes part of the process of iteration and helps to determine step-lengths, at which point I will refer to it as "well-log validation" or "log calibration". Various synthetic analyses of the basic idea have subsequently been carried out (Pan et al., 2014b; Romahn and Innanen, 2017b,a; Romahn et al., 2018), and most recently an altered version of the approach -which included wavelet phase and amplitude updates- has been shown to produce encouraging results on field data acquired at Hussar Canada in 2011 (Romahn et al., 2019). The waveform inversion formulated in this thesis, which incorporates a PSPI update direction and well-log validation, is

referred to as well-log validated waveform inversion (LVWI).

1.2 Structure of the thesis

The starting point of the research is presented in Chapter 2, where the fundamental theory of FWI is described and a synthetic environment is used in order to test the basic workflow. Aspects such as construction and conditioning of the gradient, the multiscale approach and scaling methods based on data validation, are analyzed.

Chapter 3 covers the first modification to the conventional FWI workflow, which plays an important role in shaping the LVWI. It consists in generating the update direction from a combination of PSPI migration and impedance inversion in substitution of the two-way wave operators (RTM). A two-layer model is employed to compare and calibrate the RTM and PSPI migration of the data residual.

In Chapter 4 well-log information is incorporated in the waveform workflow in exchange of data-validation techniques to scale the update direction. A combination of well-log and data validation (calibration+scaling) to produce the velocity perturbation is also investigated. The comparison of conventional FWI and LVWI is provided through numerical examples and the computational burden is analyzed.

From Chapter 5 to 7 a systematic evaluation of the sensitivity of LVWI is carried out by considering aspects such as well location and aperture, geological complexity, well data uncertainty, survey acquisition parameters, random noise and initial model.

In Chapter 8 the most promising results of the research are presented with a new waveform inversion workflow based on LVWI. The methodology incorporates a scheme to iteratively update the amplitude and phase of the wavelet allowing the process to go forward and converge in the true model even with an incorrectly estimated starting wavelet. Synthetic examples and validation on real data are provided.

The objective of this research is to establish a well-log validated waveform inversion

workflow, applicable to real seismic data, that addresses common problems in FWI such as the computational burden, the lack of convergence due to the data validation process, as well as the unknown wavelet.

Chapter 2

Full waveform inversion review

2.1 Introduction

Full waveform inversion is an optimization method whose ultimate goal is to find the model parameters that best reproduce the observed shot records. Lailly (1983) and Tarantola (1984) provided the theoretical framework and described the method as a sequence of pre-stack migrations of the data residuals, which are the difference between observed and modelled shot records. The solution of the inverse problem involves an iterative methodology that consists of a forward propagation of the actual sources and the propagation of the data residuals back in the current model. The correlation of the two wavefields yields to an update of the model parameters. The method was originally developed in the time domain, but it has also been implemented in frequency domain (Ikelle et al., 1986; Pratt et al., 1998). Examples of early applications on synthetic and real data are given by Gauthier (1986), Kolb et al. (1986), Ikelle et al. (1986), Mora (1987, 1988), Crase et al. (1990), Pica et al. (1990), Pratt (1999), etc. Problems such as computational burden, lack of low-frequency information producing cycle skipping, as well as poor convergence, are commonly mentioned through the literature. This section presents the fundamental theory behind FWI as described by Tarantola (1984) and the well-documented papers Pratt et al. (1998) and Virieux and Operto (2009). A

synthetic example, implemented in the time domain to invert for P-wave velocity, was used in order to illustrate the main steps of the FWI workflow.

2.2 An optimization method

FWI is an optimization procedure whose goal is to determine a model of the distribution of Earth properties at depth. The process starts with an initial model $\mathbf{m}_o$ (in this thesis, velocity), which is updated by a model perturbation $\Delta\mathbf{m}$ so that the new model $\mathbf{m}$ is a better representation of the true subsurface model,

$$\mathbf{m} = \mathbf{m}_o + \Delta\mathbf{m}, \tag{2.1}$$

in the sense of being able to produce synthetic data in closer agreement with the observed data.

Let $p(\mathbf{x}_r, \mathbf{x}_s, t)$ be the value of the pressure field measured at observation point $\mathbf{x}_r$, time t, due to a source at position $\mathbf{x}_s$. Suppose the measurement is made at a large number of $\mathbf{x}_r, \mathbf{x}_s, t$ values, and arrange these in a column vector:

$$\mathbf{p} = \begin{bmatrix} p(x_{r1}^1, x_{r1}^2, x_{r1}^3, x_{s1}^1, x_{s1}^2, x_{s1}^3, t_1) \\ p(x_{r1}^1, x_{r1}^2, x_{r1}^3, x_{s1}^1, x_{s1}^2, x_{s1}^3, t_2) \\ p(x_{r1}^1, x_{r1}^2, x_{r1}^3, x_{s1}^1, x_{s1}^2, x_{s1}^3, t_3) \\ \vdots \\ \vdots \\ \vdots \end{bmatrix}. \tag{2.2}$$

Next, consider that we have observed versions of the field, $p_{obs}(\mathbf{x}_r, \mathbf{x}_s, t)$, and computed versions $p_{cal}(\mathbf{x}_r, \mathbf{x}_s, t)$, meaning we have two vectors of the type in equation 2.2, which can be compared with the difference

$$\mathbf{p}_{cal}(\mathbf{m}) - \mathbf{p}_{obs}. \tag{2.3}$$

The computed field $\mathbf{p}_{cal}$ is based on a distribution of velocities $v(\mathbf{x})$, which are the unknowns in this version of FWI. The velocities are also organized into a vector $\mathbf{m}$,

$$\mathbf{m} = \begin{bmatrix} v_1 \\ v_2 \\ v_3 \\ . \\ . \\ . \end{bmatrix} = \begin{bmatrix} v(x_1) \\ v(x_2) \\ v(x_3) \\ . \\ . \\ . \end{bmatrix} \tag{2.4}$$

The vector $\mathbf{p}_{cal}$ is a function of $\mathbf{m}$. We wish to vary $\mathbf{m}$ in order to make some measure of the size of $\mathbf{p}_{cal}(\mathbf{m}) - \mathbf{p}_{obs}$ be minimum. Let this measure be

$$E(\mathbf{m}) = \frac{1}{2}(\mathbf{p}_{cal}(\mathbf{m}) - \mathbf{p}_{obs})^T(\mathbf{p}_{cal}(\mathbf{m}) - \mathbf{p}_{obs}). \tag{2.5}$$

Consider the variation of E when the model goes from some $\mathbf{m}_0$ to $\mathbf{m}_0 + \Delta\mathbf{m}$:

$$E(\mathbf{m}_0 + \Delta\mathbf{m}) \approx E(\mathbf{m}_0) + \frac{\partial E(\mathbf{m}_0)}{\partial \mathbf{m}}\Delta\mathbf{m}, \tag{2.6}$$

where the function has been approximated as a truncated Taylor series. If $\Delta\mathbf{m}$ is a step from $\mathbf{m}_0$ to a minimum, then

$$\frac{\partial E(\mathbf{m}_0 + \Delta\mathbf{m})}{\partial \mathbf{m}} = 0 \tag{2.7}$$

and we have

$$\frac{\partial E(\mathbf{m}_0 + \Delta\mathbf{m})}{\partial \mathbf{m}} \approx \frac{\partial E(\mathbf{m}_0)}{\partial \mathbf{m}} + \frac{\partial^2 E(\mathbf{m}_0)}{\partial \mathbf{m}^2}\Delta\mathbf{m} = 0, \tag{2.8}$$

which are the conditions for a Newton update:

$$\Delta\mathbf{m} = -\mathbf{H}^{-1}\mathbf{g}, \tag{2.9}$$

where

$$\mathbf{H} = \frac{\partial^2 E(\mathbf{m}_0)}{\partial \mathbf{m}^2} \tag{2.10}$$

is the Hessian matrix, and

$$\mathbf{g} = \frac{\partial E(\mathbf{m}_0)}{\partial \mathbf{m}} \tag{2.11}$$

is the gradient. The gradient of equation 2.5 is therefore important:

$$\begin{aligned}
\mathbf{g} &= \frac{1}{2}\frac{\partial}{\partial \mathbf{m}}(\mathbf{p}_{cal}(\mathbf{m}_0) - \mathbf{p}_{obs})^T(\mathbf{p}_{cal}(\mathbf{m}_0) - \mathbf{p}_{obs}) \\
&= \frac{1}{2}\frac{\partial}{\partial \mathbf{m}}(\mathbf{p}_{cal}^T\mathbf{p}_{cal} - \mathbf{p}_{cal}^T\mathbf{p}_{obs} - \mathbf{p}_{obs}^T\mathbf{p}_{cal} + \mathbf{p}_{obs}^T\mathbf{p}_{obs}) \\
&= \frac{1}{2}[2(\frac{\partial}{\partial \mathbf{m}}\mathbf{p}_{cal}^T)\mathbf{p}_{cal} - 2(\frac{\partial}{\partial \mathbf{m}}\mathbf{p}_{cal}^T)\mathbf{p}_{obs}] \\
&= \frac{\partial \mathbf{p}_{cal}}{\partial \mathbf{m}}^T \mathbf{p}_{cal} - \frac{\partial \mathbf{p}_{cal}}{\partial \mathbf{m}}^T \mathbf{p}_{obs} \\
&= \frac{\partial \mathbf{p}_{cal}}{\partial \mathbf{m}}^T (\mathbf{p}_{cal} - \mathbf{p}_{obs}) \\
&= \mathbf{J}_0^T(\mathbf{p}_{cal} - \mathbf{p}_{obs}).
\end{aligned} \tag{2.12}$$

where $\mathbf{J}$ is the sensitivity or the Fréchet derivative matrix.

The Hessian matrix is given by the derivative of the gradient (equation 2.12) with respect to the model parameter (Pratt et al., 1998; Virieux and Operto, 2009):

$$\mathbf{H} = \frac{\partial^2 E(\mathbf{m}_0)}{\partial \mathbf{m}^2} = \mathbf{J}_0^T\mathbf{J}_0 + \left[\frac{\partial \mathbf{J}_0^T}{\partial \mathbf{m}^T}(\mathbf{p}_{cal}(\mathbf{m}_0) - \mathbf{p}_{obs} \;\; \mathbf{p}_{cal}(\mathbf{m}_0) - \mathbf{p}_{obs} \;\; \ldots \;\; \mathbf{p}_{cal}(\mathbf{m}_0) - \mathbf{p}_{obs})\right]. \tag{2.13}$$

Pratt et al. (1998) explain that the second term in the Hessian is zero for linear problems, and most of the time it is neglected for nonlinear problems, leading to the approximate Hessian:

$$\mathbf{H}_a = \mathbf{J}_0^T\mathbf{J}_0. \tag{2.14}$$

A further simplification of the Hessian matrix is the pseudo-Hessian, which is constituted by the diagonal elements of the approximate Hessian (Shin et al., 2001a).

The appropriate derivation of the gradient and the Hessian provides a Newton step

minimization of $E(\mathbf{m})$. If we approximate the inverse of the Hessian by the identity matrix multiplied by a scalar μ, equation 2.9 ends up as a gradient-based step of the form

$$\Delta\mathbf{m} = -\mu\mathbf{g}. \tag{2.15}$$

The gradient and the sensitivity matrix

Equation 2.12 describes the gradient as the multiplication between the sensitivity matrix and the data residual vector. It is convenient at this point to switch from a vector expression to one including explicit sums over experimental variables. The gradient is in the same space as $\mathbf{m}$, so each element of $\mathbf{g}$ and each element of $\mathbf{m}$ refer to the velocity at some point in space $\mathbf{x}$. Meanwhile, the vectors $\mathbf{p}_{cal}$ and $\mathbf{p}_{obs}$ contain all combinations of $\mathbf{x}_r$, $\mathbf{x}_s$ and t values in the experiment, so the inner product in equation 2.12 is the overall sum of $\mathbf{x}_s$, $\mathbf{x}_r$, and t. Altogether, equation 2.12 can be written explicitly as:

$$g(\mathbf{x}) = \sum_{\mathbf{x}_s}\sum_{\mathbf{x}_r}\int_0^{tmax} dt \frac{\partial p_{cal}(\mathbf{x}_r, t; \mathbf{x}_s)}{\partial m(\mathbf{x})}\Big[p_{cal}(\mathbf{x}_r, t; \mathbf{x}_s) - p_{obs}(\mathbf{x}_r, t; \mathbf{x}_s)\Big] \tag{2.16}$$

The next task is to find a form for the sensitivities

$$\frac{\partial p_{cal}(\mathbf{x}_r, t; \mathbf{x}_s)}{\partial m(\mathbf{x})}. \tag{2.17}$$

The following derivation of the sensitivities is based on Tarantola (1984) and Yang et al. (2015).

A constant-density acoustic medium is assumed in the wave equation

$$\frac{1}{m^2(\mathbf{x})}\frac{\partial^2 p_{cal}(\mathbf{x}, t; \mathbf{x}_s)}{\partial t^2} - \nabla^2 p_{cal}(\mathbf{x}, t; \mathbf{x}_s) = f_s(\mathbf{x}, t; \mathbf{x}_s), \tag{2.18}$$

where m is velocity, $f_s(\mathbf{x}, t; \mathbf{x}_s) = f(t - t')\delta(\mathbf{x} - \mathbf{x}_s)$ is the source term, and δ is the Dirac delta function. An important instance of the wave equation is for an impulsive source

$(f(t-t') = \delta(t-t'))$:

$$\frac{1}{m^2(\mathbf{x})}\frac{\partial^2 G(\mathbf{x},t;\mathbf{x}_s,t')}{\partial t^2} - \nabla^2 G(\mathbf{x},t;\mathbf{x}_s,t') = \delta(\mathbf{x}-\mathbf{x}_s)\delta(t-t'), \tag{2.19}$$

which defines G, Green's function. An integral representation of the solution for $p_{cal}(\mathbf{x}_r,t;\mathbf{x}_s)$ is (Tarantola, 1984)

$$\begin{aligned} p_{cal}(\mathbf{x}_r,t;\mathbf{x}_s) &= \int_V d\mathbf{x} \int dt' G(\mathbf{x}_r,t;\mathbf{x},t') f(\mathbf{x},t';\mathbf{x}_s) \\ &= \int_V d\mathbf{x} \int dt' G(\mathbf{x}_r,t-t';\mathbf{x},0) f(\mathbf{x},t';\mathbf{x}_s), \end{aligned} \tag{2.20}$$

or

$$p_{cal}(\mathbf{x}_r,t;\mathbf{x}_s) = \int_V d\mathbf{x} G(\mathbf{x}_r,t;\mathbf{x},0) * f(\mathbf{x},t;\mathbf{x}_s), \tag{2.21}$$

where $*$ denotes temporal convolution.

Following a perturbative approach, where small variations in the model $m(\mathbf{x}) \rightarrow m_0(\mathbf{x}) + \Delta m(\mathbf{x})$ produce small variations in the field $p_{cal}(\mathbf{x},t;\mathbf{x}_s) \rightarrow p_{cal}(\mathbf{x},t;\mathbf{x}_s) + \Delta p_{cal}(\mathbf{x},t;\mathbf{x}_s)$, equation 2.18 becomes

$$\begin{aligned} \frac{1}{[m_0(\mathbf{x}) + \Delta m(\mathbf{x})]^2}\frac{\partial^2 [p_{cal}(\mathbf{x},t;\mathbf{x}_s) + \Delta p_{cal}(\mathbf{x},t;\mathbf{x}_s)]}{\partial t^2} - \nabla^2 [p_{cal}(\mathbf{x},t;\mathbf{x}_s) + \Delta p_{cal}(\mathbf{x},t;\mathbf{x}_s)] \\ = f_s(\mathbf{x},t;\mathbf{x}_s). \end{aligned} \tag{2.22}$$

The term containing the perturbed velocity model in the left-hand side of equation 2.22 can be approximated as the truncated binomial series

$$\frac{1}{[m_0(\mathbf{x}) + \Delta m(\mathbf{x})]^2} \approx \frac{1}{m_0^2(\mathbf{x})} - \frac{2\Delta m(\mathbf{x})}{m_0^3(\mathbf{x})}. \tag{2.23}$$

Substituting equation 2.23 in equation 2.22, we obtain

$$\begin{aligned}\left[\frac{1}{m_0^2(\mathbf{x})}-\frac{2\Delta m(\mathbf{x})}{m_0^3(\mathbf{x})}\right]\frac{\partial^2[p_{cal}(\mathbf{x},t;\mathbf{x}_s)+\Delta p_{cal}(\mathbf{x},t;\mathbf{x}_s)]}{\partial t^2}\\ -\nabla^2[p_{cal}(\mathbf{x},t;\mathbf{x}_s)+\Delta p_{cal}(\mathbf{x},t;\mathbf{x}_s)]\approx f_s(\mathbf{x},t;\mathbf{x}_s).\end{aligned} \tag{2.24}$$

Subtracting equation 2.24 from 2.18 yields

$$\begin{aligned}\frac{1}{m_0^2(\mathbf{x})}\frac{\partial^2\Delta p_{cal}(\mathbf{x},t;\mathbf{x}_s)}{\partial t^2}-\nabla^2\Delta p_{cal}(\mathbf{x},t;\mathbf{x}_s)&\approx\frac{\partial^2[p_{cal}(\mathbf{x},t;\mathbf{x}_s)+\Delta p_{cal}(\mathbf{x},t;\mathbf{x}_s)]}{\partial t^2}\frac{2\Delta m(\mathbf{x})}{m_0^3(\mathbf{x})}\\ &\approx\frac{\partial^2 p_{cal}(\mathbf{x},t;\mathbf{x}_s)}{\partial t^2}\frac{2\Delta m(\mathbf{x})}{m_0^3(\mathbf{x})}+\frac{\partial^2\Delta p_{cal}(\mathbf{x},t;\mathbf{x}_s)}{\partial t^2}\frac{2\Delta m(\mathbf{x})}{m_0^3(\mathbf{x})}\end{aligned} \tag{2.25}$$

The quadratic term in the right-hand side, constituted by the multiplication of the model perturbation and the wavefield perturbation, is assumed to be very small and can be neglected. Retaining only terms that are linear in either perturbation, equation 2.25 becomes

$$\frac{1}{m_0^2(\mathbf{x})}\frac{\partial^2\Delta p_{cal}(\mathbf{x},t;\mathbf{x}_s)}{\partial t^2}-\nabla^2\Delta p_{cal}(\mathbf{x},t;\mathbf{x}_s)\approx\frac{\partial^2 p_{cal}(\mathbf{x},t;\mathbf{x}_s)}{\partial t^2}\frac{2\Delta m(\mathbf{x})}{m_0^3(\mathbf{x})}. \tag{2.26}$$

That is, the perturbed wavefield is excited by the interaction of the unperturbed wavefield with the velocity perturbation.

From analysis of the wave equation, the integral representation of the solution of equation 2.26 is

$$\Delta p_{cal}(\mathbf{x}_r,t;\mathbf{x}_s)\approx\int_V d\mathbf{x}' G(\mathbf{x}_r,t;\mathbf{x}',0)*\frac{\partial^2 p_{cal}(\mathbf{x}',t;\mathbf{x}_s)}{\partial t^2}\frac{2\Delta m(\mathbf{x}')}{m_0^3(\mathbf{x}')}. \tag{2.27}$$

This formula can be used to determine the sensitivity of the wavefield p to a variation in $m(\mathbf{x}')$ at a particular location $\mathbf{x}$. Specifying

$$\Delta m(\mathbf{x}')=\Delta m(\mathbf{x})\delta(\mathbf{x}'-\mathbf{x}), \tag{2.28}$$

and substituting into equation 2.27, we obtain

$$\Delta p_{cal}(\mathbf{x}_r, t; \mathbf{x}_s) \approx G(\mathbf{x}_r, t; \mathbf{x}, 0) * \frac{\partial^2 p_{cal}(\mathbf{x}, t; \mathbf{x}_s)}{\partial t^2} \frac{2\Delta m(\mathbf{x})}{m_0^3(\mathbf{x})}. \tag{2.29}$$

Dividing by $\Delta m(\mathbf{x})$ and taking the limit

$$\begin{aligned} \lim_{\Delta m \to 0} \frac{\Delta p_{cal}(\mathbf{x}_r, t; \mathbf{x}_s)}{\Delta m(\mathbf{x})} &\approx \frac{2}{m_0^3(\mathbf{x})} G(\mathbf{x}_r, t; \mathbf{x}, 0) * \frac{\partial^2 p_{cal}(\mathbf{x}, t; \mathbf{x}_s)}{\partial t^2} \\ &= \frac{\partial p_{cal}(\mathbf{x}_r, t; \mathbf{x}_s)}{\partial m(\mathbf{x})}. \end{aligned} \tag{2.30}$$

Therefore, the gradient 2.16 is

$$g(\mathbf{x}) = \sum_{\mathbf{x}_s} \sum_{\mathbf{x}_r} \int_0^{tmax} dt \frac{2}{m^3(\mathbf{x})} G(\mathbf{x}_r, t; \mathbf{x}, 0) * \frac{\partial^2 p_{cal}(\mathbf{x}, t; \mathbf{x}_s)}{\partial t^2} [p_{cal}(\mathbf{x}_r, t; \mathbf{x}_s) - p_{obs}(\mathbf{x}_r, t; \mathbf{x}_s)]. \tag{2.31}$$

Applying the convolution property

$$\int dt [g(t) * f(t)] h(t) = \int dt f(t) [g(-t) * h(t)], \tag{2.32}$$

we have

$$\begin{aligned} g(\mathbf{x}) &= \sum_{\mathbf{x}_s} \sum_{\mathbf{x}_r} \int_0^{tmax} dt \frac{2}{m^3(\mathbf{x})} \frac{\partial^2 p_{cal}(\mathbf{x}, t; \mathbf{x}_s)}{\partial t^2} \Big[G(\mathbf{x}_r, -t; \mathbf{x}, 0) * [p_{cal}(\mathbf{x}_r, t; \mathbf{x}_s) - p_{obs}(\mathbf{x}_r, t; \mathbf{x}_s)] \Big] \\ &= \sum_{\mathbf{x}_s} \sum_{\mathbf{x}_r} \int_0^{tmax} dt \frac{2}{m^3(\mathbf{x})} \frac{\partial^2 p_{cal}(\mathbf{x}, t; \mathbf{x}_s)}{\partial t^2} \Big[G(\mathbf{x}_r, 0; \mathbf{x}, t) * [p_{cal}(\mathbf{x}_r, t; \mathbf{x}_s) - p_{obs}(\mathbf{x}_r, t; \mathbf{x}_s)] \Big] \\ &= \sum_{\mathbf{x}_s} \sum_{\mathbf{x}_r} \int_0^{tmax} dt \frac{2}{m^3(\mathbf{x})} \frac{\partial^2 p_{cal}(\mathbf{x}, t; \mathbf{x}_s)}{\partial t^2} p_{res}(\mathbf{x}_r, t; \mathbf{x}_s), \end{aligned} \tag{2.33}$$

where $p_{res}(\mathbf{x}_r, t; \mathbf{x}_s) = G(\mathbf{x}_r, 0; \mathbf{x}, t) * [p_{cal}(\mathbf{x}_r, t; \mathbf{x}_s) - p_{obs}(\mathbf{x}_r, t; \mathbf{x}_s)]$ is the back-propagated wavefield using the residual $p_{cal}(\mathbf{x}_r, t; \mathbf{x}_s) - p_{obs}(\mathbf{x}_r, t; \mathbf{x}_s)$. Equation 2.33 shows that the full-waveform inversion gradient is equivalent to a migration of the data residuals using a 2-

way Green's function (RTM). The FWI gradient-based steps are therefore iterated sequences of depth migrations, each time migrating new differences between modelled and measured data through an updated model.

If the data residuals are defined as $\mathbf{p}_{obs} - \mathbf{p}_{cal}$, the gradient in equation 2.16 takes on a negative sign

$$g(\mathbf{x}) = -\sum_{\mathbf{x}_s}\sum_{\mathbf{x}_r}\int_0^{tmax} dt \frac{\partial p_{cal}(\mathbf{x}_r, t; \mathbf{x}_s)}{\partial m(\mathbf{x})}\Big[p_{obs}(\mathbf{x}_r, t; \mathbf{x}_s) - p_{cal}(\mathbf{x}, t; \mathbf{x}_s)\Big] \tag{2.34}$$

and the velocity perturbation becomes

$$\begin{aligned}\Delta m(\mathbf{x}) &= -\mu g(\mathbf{x}) \\ &= \mu \sum_{\mathbf{x}_s}\sum_{\mathbf{x}_r}\int_0^{tmax} dt \frac{\partial p_{cal}(\mathbf{x}_r, t; \mathbf{x}_s)}{\partial m(\mathbf{x})}\Big[p_{obs}(\mathbf{x}_r, t; \mathbf{x}_s) - p_{cal}(\mathbf{x}, t; \mathbf{x}_s)\Big] \\ &= \mu\Phi(\mathbf{x}),\end{aligned} \tag{2.35}$$

where $\mathbf{\Phi}$ is the update direction.

2.2.1 Gradient conditioning

The velocity perturbation in equation 2.35 is obtained by applying the gradient-based method, which approximates the Hessian matrix as an identity matrix, reducing the problem to a scaling of the gradient. The interpretation of the Hessian matrix and its diagonal terms provides an insight into what this simplification implies. Pratt et al. (1998) highlighted the fact that convergence rates in iterative solutions can be improved by preconditioning the gradient with the inverse Hessian, or an approximation of the inverse Hessian. The approximate Hessian (Gauss-Newton method) is more commonly used due to the large computational cost of calculating the full inverse Hessian (Newton method). Pratt et al. (1998) pointed out that the approximate Hessian matrix is diagonally dominant and predicts the defocussing that affects the gradient vector due to the incomplete and uneven illumination of the target. Shin

et al. (2001b) showed that the diagonal terms of the inverse Hessian produce a gain to the gradient estimation; thus they help compensating for the geometrical spreading. Margrave et al. (2012a) described the FWI gradient as a poor migration that lacks gain correction, and discussed reasons why such an update causes slow convergence. They proposed replacing the correlation imaging condition inherent in the FWI gradient with a deconvolution imaging condition (also called illumination compensation). They argued that such a change would produce similar effects to the diagonal terms in the approximate Hessian, with the advantage that it is computationally free of cost. Pan et al. (2014a) analyzed the use of the deconvolution imaging condition as a mean to condition the gradient while comparing the approximate Hessian, the pseudo-Hessian, and the diagonalized pseudo-Hessian (which is analogous to the use of a standard deconvolution imaging condition).

In section 2.2 (equation 2.33), the FWI gradient was shown to be obtained by applying reverse time migration to the data residual. If we express the gradient as the cross-correlation between the forward propagated source wavefield (p_s) and the backward propagated data residuals (p_{res})

$$g_{cc}(\mathbf{x}) = \sum_{\mathbf{x}_s} \int_0^{t_{max}} dt \sum_{\mathbf{x}_r} p_s(\mathbf{x}, t; \mathbf{x}_s) p_{res}(\mathbf{x}, t; \mathbf{x}_r), \tag{2.36}$$

the conditioned gradient with a "deconvolution" imaging condition can be expressed as

$$g_{dec} = \sum_{\mathbf{x}_s} \frac{\int_0^{t_{max}} dt \sum_{\mathbf{x}_r} p_s(\mathbf{x}, t; \mathbf{x}_s) p_{res}(\mathbf{x}, t; \mathbf{x}_r)}{\int_0^{t_{max}} \sum_{\mathbf{x}_r} p_s(\mathbf{x}, t; \mathbf{x}_s) p_s(\mathbf{x}, t; \mathbf{x}_s) + \eta I_{max}}, \tag{2.37}$$

where η is a small positive constant, and $I_{max} = \underset{x}{max}[p_s(\mathbf{x}, t; \mathbf{x}_s) p_s(\mathbf{x}, t; \mathbf{x}_s)]$.

Margrave et al. (2011b) and Wenyong et al. (2013) consider that this approach estimates reflectivity (R), and they propose to obtain the impedance perturbation by applying

$$\Delta I_k \approx 2 I_k R_k, \tag{2.38}$$

where I_k is the impedance in the kth iteration. The term $2I_k$ works mainly as a scalar

factor, and we still need to calculate a step-length to produce a suitable model perturbation (Wenyong et al., 2013). The term $2I_k$ can be absorbed by the step-length μ, and the model perturbation is

$$\Delta I_k \approx \mu R_k. \tag{2.39}$$

Why does a simple scalar applied to R produce the model perturbation? The answer is that R, which is obtained by applying RTM with a deconvolution imaging condition in time domain, is not reflectivity, as shown by the following analysis:

The "deconvolution" imaging condition in time is expressed as

$$i = u/d, \tag{2.40}$$

where i is an image, u is the up-going receiver wavefield and d is the down-going wavefield. Equation 2.40 is a restatement of

$$u = id, \tag{2.41}$$

which is different from the convolutional model given by

$$u = r * d, \tag{2.42}$$

where r is reflectivity. Therefore, i is different from reflectivity, but it works as a preconditioned FWI gradient because this image has been compensated by geometrical spreading.

The numerical example shown in section 2.5 implements the gradient preconditioned with a "deconvolution" imaging condition.

2.3 Scaling the gradient

The purpose of this step is to make the amplitude of the gradient at each spatial point proportional to the velocity change (Vigh et al., 2009), as it is expressed in equation 2.35,

where the model perturbation is produced by multiplying the update direction by a step-length scalar μ. The step-length can be obtained in several ways. Two widely used methods are described below: the first one is based on the minimization of the objective function with respect to the step-length, as proposed by Tarantola (1984) and Pica et al. (1990). This method will be referred to as Tarantola and Pica's approach. The second method corresponds to a line search, which applies backtracking and quadratic interpolation. In this thesis, I will refer as *data validation* to the techniques that compute the step-length by explicitly minimizing the data residuals.

2.3.1 Step-length by minimizing the objective function

Tarantola (1987) and Pica et al. (1990) computed the scalar step-length through the minimization of the objective function with respect to the step-length. They first expressed the objective function for the updated model as

$$E(\mathbf{m}_{k+1}) = E(\mathbf{m}_k + \Delta\mathbf{m}_k) = E(\mathbf{m}_k + \mu_k\mathbf{\Phi}_k), \tag{2.43}$$

where k denotes iteration number, and $\mathbf{\Phi}_k$ is the update direction. The misfit function can be expressed in terms of the observed and modelled data as

$$E(\mathbf{m}_{k+1}) = [\mathbf{p}_{obs} - \mathbf{f}(\mathbf{m}_k + \mu_k\mathbf{\Phi}_k)]^\dagger[\mathbf{p}_{obs} - \mathbf{f}(\mathbf{m}_k + \mu_k\mathbf{\Phi}_k)], \tag{2.44}$$

where $\mathbf{f}(\cdot)$ is a forward modelling operator. The expression $E(\mathbf{m}_{k+1})$ can be written as

$$E(\mathbf{m}_{k+1}) = [\mathbf{p}_{obs} - \mathbf{f}(\mathbf{m}_k) + \mu_k\mathbf{F}_k\mathbf{\Phi}_k)]^\dagger[\mathbf{p}_{obs} - \mathbf{f}(\mathbf{m}_k) + \mu_k\mathbf{F}_k\mathbf{\Phi}_k)], \tag{2.45}$$

where $\mathbf{F}$ is the linear operator that takes the derivative of $\mathbf{f}$ at point $\mathbf{m}_k$,

$$\mathbf{F}\mathbf{\Phi}_k = \lim_{\epsilon\to 0}\frac{\mathbf{f}(\mathbf{m}_k + \epsilon\mathbf{\Phi}_k) - \mathbf{f}(\mathbf{m}_k)}{\epsilon}, \tag{2.46}$$

where ϵ is a small positive constant. $\mathbf{F}\mathbf{\Phi}_k$ describes how the modelled wavefield changes with respect to the step-length given an update direction.

A suitable candidate for epsilon is

$$\epsilon = 0.05\sqrt{\frac{< \mathbf{m}_k, \mathbf{m}_k >}{< \mathbf{\Phi}_k, \mathbf{\Phi}_k >}}, \tag{2.47}$$

where $< \cdot, \cdot >$ means scalar product and provides the square of the magnitude of the model and update-direction vectors. The square root of the ratio between the scalar product of the model and the update-direction vectors produces a convenient factor which, when multiplied by the update direction, sets this vector on the same level of magnitude as the model vector. The small factor 0.05 ensures that the scaled update direction is small enough to be considered a model perturbation.

Setting the derivative of equation 2.45 with respect to μ_k equal to zero and isolating μ_k, we have

$$\mu_k = \frac{[\mathbf{F}_k\mathbf{\Phi}_k]^\dagger[\mathbf{p}_{obs} - \mathbf{f}(\mathbf{m}_k)]}{[\mathbf{F}_k\mathbf{\Phi}_k]^\dagger[\mathbf{F}_k\mathbf{\Phi}_k]}. \tag{2.48}$$

Solving for μ_k requires an extra forward modelling in a medium $\mathbf{m} = \mathbf{m}_k + \epsilon\mathbf{\Phi}_k$.

The multiplication of the update direction Φ_k by the scalar μ_k provides physical units of the model parameter as it is shown next. Denoting the unit operator $[\cdot]_u$, we have that the units of ϵ are

$$[\epsilon]_u = \sqrt{\frac{[m^2]_u}{[\Phi^2]_u}} = \frac{[m]_u}{[\Phi]_u}. \tag{2.49}$$

On the other hand, the units of the operator $\mathbf{F}$ applied to $\mathbf{\Phi}$ are

$$[\mathbf{F}\mathbf{\Phi}]_u = \frac{[data]_u}{[\epsilon]_u} = \frac{[data]_u[\Phi]_u}{[m]_u}. \tag{2.50}$$

Finally, the units of μ_k in equation 2.48 are

$$[\mu_k]_u = \frac{\frac{[data]_u[\Phi]_u}{[m]_u}[data]_u}{\frac{[data]_u[\Phi]_u}{[m]_u}\frac{[data]_u[\Phi]_u}{[m]_u}} = \frac{[data^2]_u[m^2]_u[\Phi]_u}{[data^2]_u[m]_u[\Phi^2]_u} = \frac{[m]_u}{[\Phi]_u}. \tag{2.51}$$

The units that result from multiplying Φ_k by μ_k are

$$[\mu_k \Phi_k]_u = \frac{[m]_u}{[\Phi]_u}[\Phi]_u = [m]_u, \tag{2.52}$$

the model units.

2.3.2 Backtracking line search and quadratic interpolation

A complete explanation of line search methods can be found in Nocedal and Wright (2006). Line search methods compute the step-length, i.e., the distance in model space to be moved in a given update direction. The step-length μ is chosen such that some set of conditions is satisfied. For instance, the *sufficient decrease* or *Armijo condition* is based on the inequality

$$E(\mathbf{m}_k + \mu \mathbf{\Phi}_k) \leq E(\mathbf{m}_k) + c_1 \mu \nabla E_k^T \mathbf{\Phi}_k, \tag{2.53}$$

where c_1 is a constant between 0 and 1. These conditions state that the objective function should be proportional to both the step-length μ and the directional derivative $\nabla E_k^T \mathbf{\Phi}_k$. However, small values of μ may be needed to satisfy the sufficient decrease condition resulting in poor progress. The *curvature condition* rejects unacceptably short steps, requiring μ to satisfy

$$\nabla E(\mathbf{m}_k + \mu_k \mathbf{\Phi}_k)^T \mathbf{\Phi}_k \geq c_2 \nabla E_k^T \mathbf{\Phi}_k. \tag{2.54}$$

The derivative in the left-hand side ensures that the slope of $E(\mathbf{m}_k + \mu_k \mathbf{\Phi}_k)$ at μ_k is greater than c_2, the initial slope, when $\mu = 0$. The sufficient decrease and curvature conditions are known together as the Wolfe conditions. The backtracking approach is based on the sufficient decrease condition and, by providing a proper step-length candidate, it can work without the curvature condition. We start by defining

$$\mu = c\mu_0, \tag{2.55}$$

where a suitable candidate μ_0 is provided by equation 2.47. The next step is to find a value of c that satisfies

$$E(\mathbf{m}_k + c\mu_0\mathbf{\Phi}_k) \leq E(\mathbf{m}_k). \tag{2.56}$$

When $c = c_0 = 0$, we have $E_0 = E(\mathbf{m}_k)$. The point (c_0, E_0) is the residual reference that we want to reduce. We start with an initial guess for c_1, e.g., $c_1 = 0.5$, that will produce a residual $E_1 = E(\mathbf{m}_k + c_1\mu_0\mathbf{\Phi}_k)$. At this point we have two possible scenarios shown in

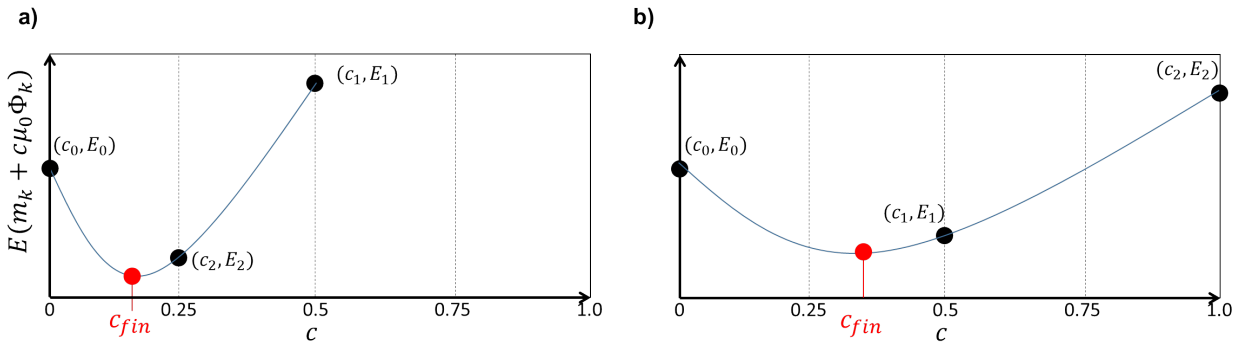

Figure 2.1: Backtracking line search. a) When the initial $c_1 = 0.5$ produces a residual $E_1 \geq E_0 = E(\mathbf{m}_k)$, we progressively reduce the value of c; for instance, $c_2 = 0.5c_1$ until the condition in equation 2.56 is satisfied. b) When the initial $c_1 = 0.5$ provides a residual $E_1 \leq E_0 = E(\mathbf{m}_k)$, we try a larger value of c; for instance, $c_2 = 2c_1$ that will produce a residual $E2$. Having the three points (c_0, E_0), (c_1, E_1) and (c_2, E_2), we can apply a quadratic interpolation to find c_{fin}.

Figure 2.1: a) $E_1 \geq E_0$, or b) $E_1 \leq E_0$. In the first case we progressively decrease the value of c as $c_2 = 0.5c_1$ until we find a c_2 providing a residual E_2 that satisfies the condition in equation 2.56. After the procedure, three points (c_0, E_0), (c_1, E_1) and (c_2, E_2) are available. Assuming that the objective function is locally quadratic and that we are close to the global minimum of E, we can interpolate these points in order to find the c_{fin} that is expected to produce the smallest residual. In the second scenario, when $E_1 \leq E_0$, we try a larger value of c, such as $c_2 = 2c_1$. In this case, E_2 can be smaller or greater than E_0; either way, we will

have three points to set up the quadratic interpolation given by

$$c_{fin} = \frac{1}{2}\frac{E_0(c_2^2 - c_1^2) + E_1(c_0^2 - c_2^2) + E_2(c_1^2 - c_0^2)}{E_0(c_2 - c_1) + E_1(c_0 - c_2) + E_2(c_1 - c_0)}. \tag{2.57}$$

This method requires at least two forward modelling steps to generate the input to the quadratic interpolation. The backtracking process, described in Figure 2.1a, may require more than two forward modelling steps before satisfying the condition in equation 2.56.

Upon completion of this process, the velocity update will be given by

$$\Delta \mathbf{m}_k = c_{fin}\mu_0 \mathbf{\Phi}_k. \tag{2.58}$$

2.4 A numerical example of the FWI workflow

Within a synthetic (numerically simulated) environment, the concepts surrounding FWI are applied. In all algorithms, both explicitly in the simulation, and implicitly in the migration step, a 2D medium governed by the constant density acoustic wave equation is assumed to hold. All simulations in this thesis are carried out with a fourth-order finite difference scalar acoustic algorithm. A detailed description of the forward modelling algorithm is given in Youzwishen and Margrave (1999).

The FWI workflow is illustrated in Figure 2.2. It takes the form of an iterative cycle (Margrave et al., 2010), where the velocity model is updated while reducing the difference between the observed shot records and the modelled shot records. The main steps are:

1. Modelling of synthetic shot records ($\mathbf{p}_{cal}$), which are subtracted from the observed shot records ($\mathbf{p}_{obs}$) to produce the data residuals $\Delta\mathbf{p}$.

2. Construction of the update direction (Φ) by reverse time migration and stack of the data residuals: $Stk[Mig(\Delta\mathbf{p})]$, where $Stk(\cdot)$ and $Mig(\cdot)$ are stack and migration operators. A mute can be applied before stacking in order to remove migration artifacts.

The frequencies to be migrated are windowed by applying a bandpass filter to the data residuals and the wavelet. This is desirable in the implementation of a multiscale approach.

3. Computation of the step-length (μ) that scales the gradient and converts it into a velocity perturbation.

4. Sum of the current model ($\mathbf{m}_k$) and the velocity perturbation ($\Delta\mathbf{m}_k$) to generate a new model ($\mathbf{m}_{k+1}$) that will be used in the next iteration.

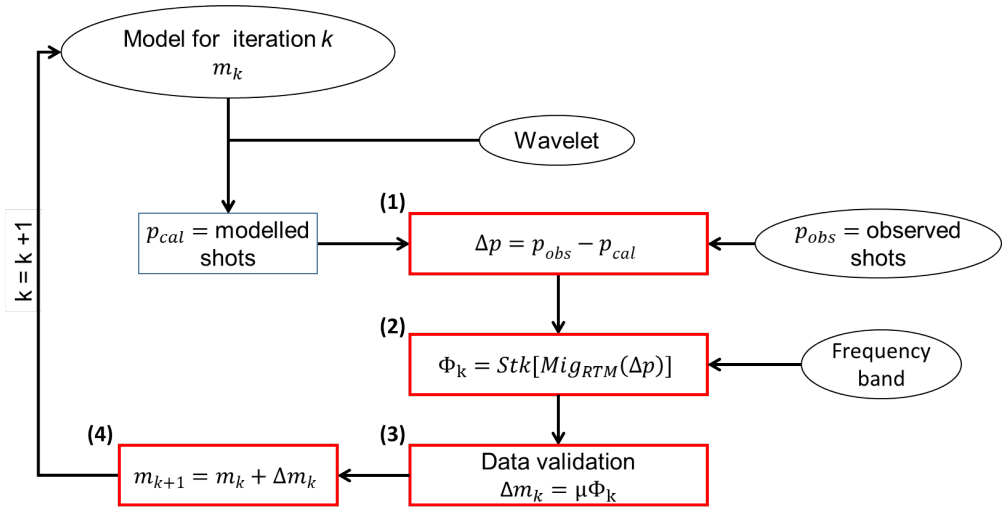

Figure 2.2: The FWI workflow is an iterative cycle of four main steps: (1) generation of the data residuals, (2) construction of the update direction, (3) scaling the update direction to obtain the velocity perturbation, and (4) updating the model. Adapted from Margrave et al. (2010)

2.4.1 True model, initial model and data residuals

The FWI workflow is examined with a synthetic example involving a moderate degree of lateral variability. The model, illustrated in Figure 2.3a, is chosen to be a shallow anticline containing a low-velocity reservoir surrounded by relatively high-velocity rocks. Two features are added in order to test the ability of the algorithm to resolve stratigraphic features: a

low-velocity trap is placed at an 800m depth on the left-hand side of the model, and a high-velocity body is positioned at a 300m depth near the right-hand edge of the model. A minimum-phase wavelet, with a dominant frequency of 10Hz (Figure 2.4a-b), is employed to generate 83 synthetic shot records. These will be referred to as the observed shots. The sources and receivers are positioned at 120m and 10m intervals across the surface. The initial model, plotted in Figure 2.3b, is generated by applying a Gaussian smoother with a half-width of 200m to the true model. Figures 2.5a-b show a comparison between an observed and a modelled shot record located at the center of the model. The correspondent data residual is plotted in Figure 2.5c. The data residual for the first iteration is mainly constituted by the observed shot record with a slightly attenuated direct arrival.

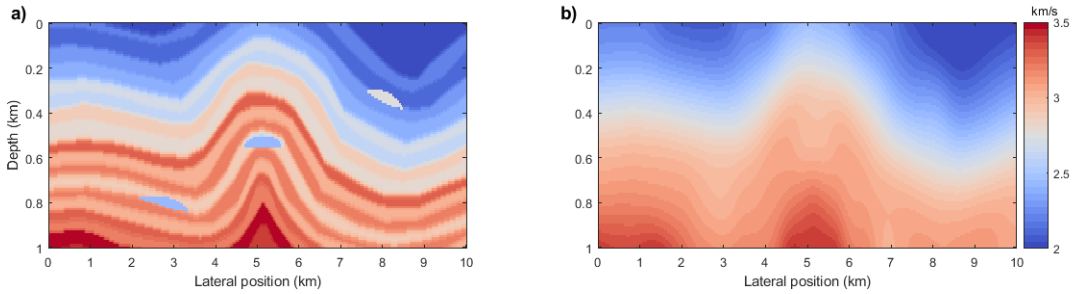

Figure 2.3: (a) True velocity model. (b) Initial velocity model.

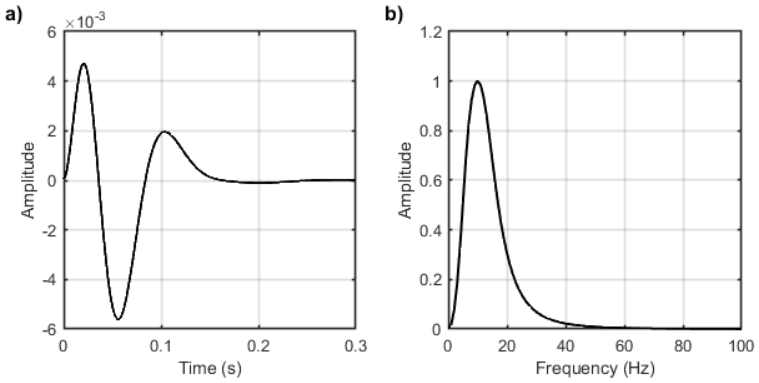

Figure 2.4: (a) Source wavelet. (b) Amplitude spectrum.

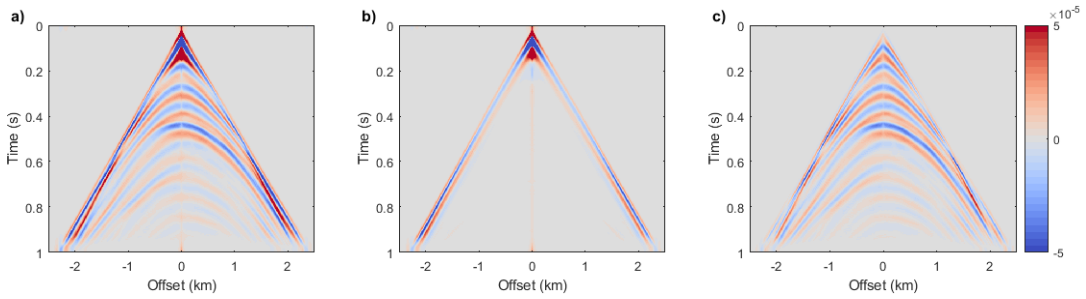

Figure 2.5: (a) Observed shot record. (b) Modelled shot record for iteration 1. (c) Data residual = (a) - (b).

2.4.2 Gradient construction

The construction of the gradient involves the migration of the data residuals (by using the current velocity model) and stack. Optionally, a mute can be applied to the migrated residuals before stacking, as it is shown in Figure 2.6. The gradient with no preconditioning, i.e., using a cross-correlation imaging condition, is plotted in Figure 2.7a. Figure 2.7b shows the gradient with a deconvolution imaging condition. Note that the shallow artifacts in the former have been diminished by compensating the geometrical spreading.

The inversion is carried out using a multi-scale approach (Pratt et al., 1998). The starting migration frequency band is 1-6Hz, which is increased by 1Hz at each iteration. The input frequencies are controlled by a bandpass filter applied to the wavelet and the data residuals before the migration. Table 2.1 shows the frequencies employed at each iteration.

Table 2.1: Frequency strategy for the multiscale approach

Iteration	Frequency band (Hz)
1	1-6
2	2-7
3	3-8
...	...
20	20-26

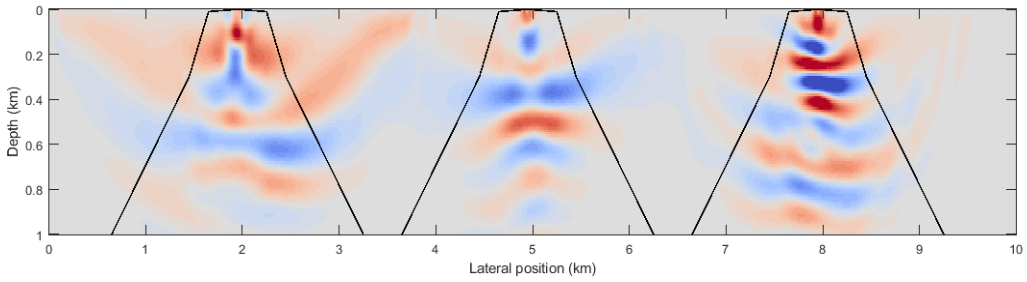

Figure 2.6: Example of three different migrated data residuals for the first iteration. A frequency band from 1-6Hz was used. The black curves represent the mute applied before stacking.

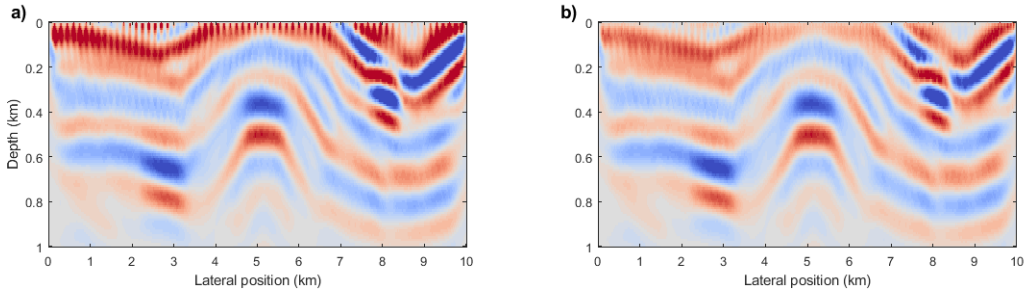

Figure 2.7: The stack of the migrated data residuals produces the gradient. (a) Gradient with cross-correlation imaging condition for iteration 1. (b) Gradient with deconvolution imaging condition for iteration 1.

2.4.3 Scaling the gradient

Two data-validation methods to scale the update direction, described in section 2.4, are compared in this section. The first method corresponds to Tarantola and Pica's approach. It is based on the minimization of the objective function with respect to the step-length and only needs one extra forward modelling. The second approach implements a backtracking line search and quadratic interpolation and needs at least two forward modellings. Five shots, distributed across the model, are used for the computation. The step-lengths, derived by the two methods, produce similar results. Figure 2.8a plots the velocity perturbation obtained by Tarantola and Pica's approach for iterations 1, 5, 10, 15 and 20. Figure 2.8b shows the same for the backtracking method. Since both approaches produce similar step-lengths, the resulting velocity perturbations are alike. An advantage of Tarantola and Picas's method

over backtracking is that the former has a smaller computational burden, as it is shown in Figure 2.9.

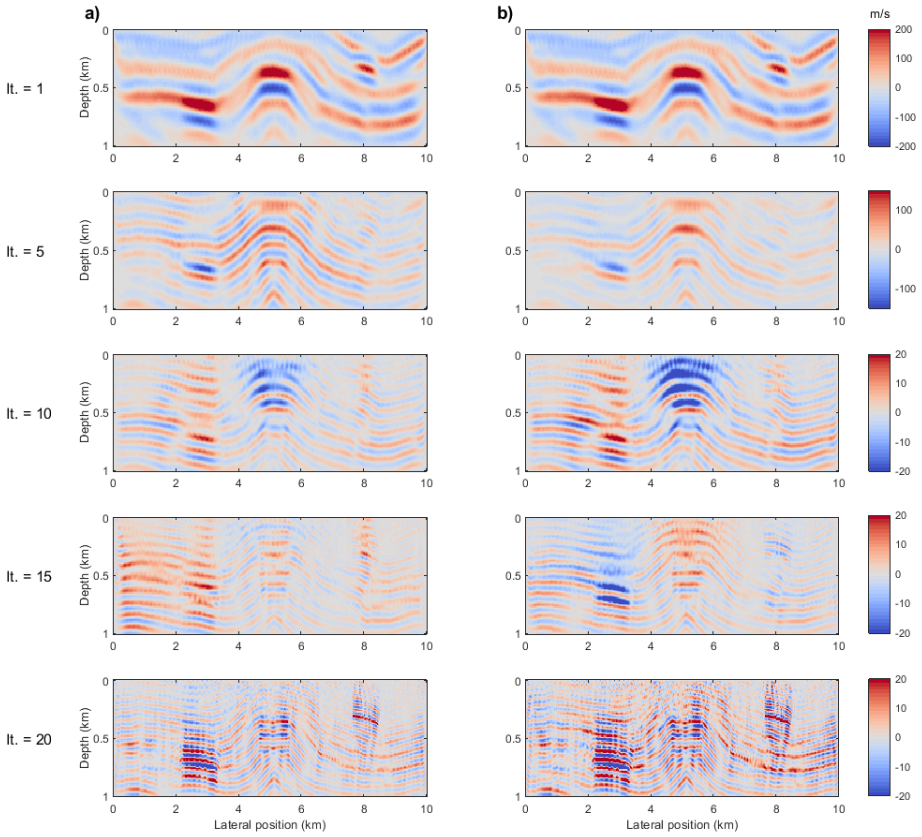

Figure 2.8: Velocity perturbations for iterations 1, 5, 10, 15, and 20, obtained by scaling the gradient using (a) Tarantola-and-Pica's approach, and (b) backtracking line search and quadratic interpolation.

2.4.4 Model updating

Recalling equation 2.1, the sum of the current model and the velocity perturbation generates the updated model. Figure 2.10 shows this process for the first iteration. In this case, I used the update direction scaled by applying Tarantola and Pica's method. The updated model will be the input for the next iteration, as described in the workflow in Figure 2.2.

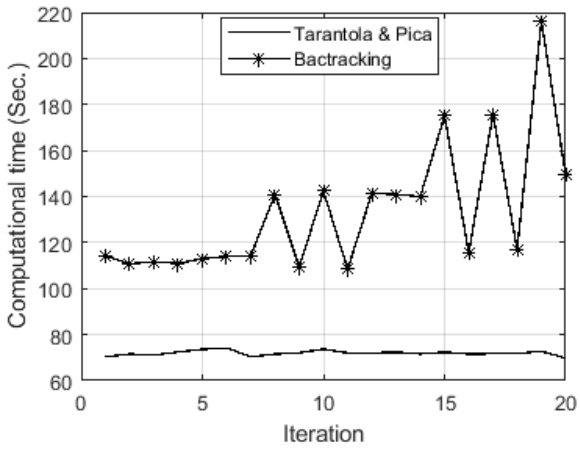

Figure 2.9: Step-length computational time with iteration for (a) Tarantola and Pica's approach, and (b) backtracking line search and quadratic interpolation.

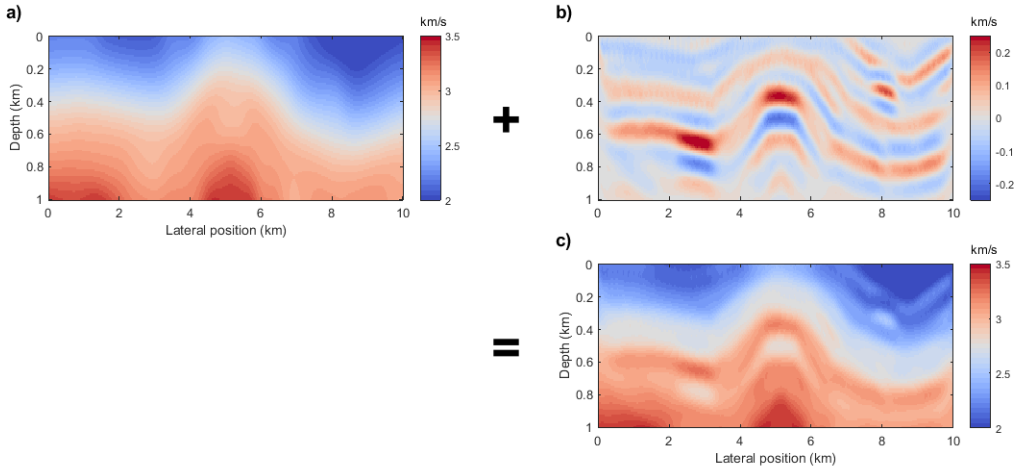

Figure 2.10: Model updating for iteration 1. (a) Initial model. (b) Velocity perturbation. (c) Updated model = (a) + (b).

2.4.5 Results

The final inverted model after 20 iterations, for a gradient scaled by Tarantola and Pica's method, is plotted in Figure 2.11a. Figures 2.11b-d show the inverted velocity at the location of w1, w2, and w3 (simulated wells at the lateral positions of 2850m, 5150m and 8110m). The synthetic example confirms the potential of FWI for recovering information of the subsurface model from seismic reflection shot records. Figure 2.12a-b shows the comparison between

the observed and the final modelled shot records. The data residual, plotted in Figure 2.12c, has been drastically reduced after 20 iterations. The standard RTM-based FWI uses all data in the residuals: narrow and wide-angle reflections and refractions, which are minimized as we iterate. I will use the model error and the data residual norms to analyze the inversion results throughout this thesis. The model error is defined as

$$Error^m = \frac{\sum |v_{true} - v_{inverted}|}{nx}, \tag{2.59}$$

where nx is the number of lateral positions. The data residual norm is

$$\mathrm{DR}_{\mathrm{norm}} = \sum_{r=1}^{nr} \sum_{s=1}^{ns} \int_0^{t_{max}} dt |\mathbf{p}_{cal}(x_r, t; x_s) - \mathbf{p}_{obs}(x_r, t; x_s)|^2. \tag{2.60}$$

The error in the model and the data residual norms, plotted in 2.13a-b, continuously decrease with iteration, showing that the process is stable and converge in this simple synthetic environment.

Figure 2.14 shows the evolution of the inverted-model reflectivity amplitude spectrum with iteration (red curve). The true-model (blue curve) and initial-model (discontinuous black curve) reflectivity amplitude spectra are also plotted as a reference. The model reflectivities were obtained by applying the definition of normal-incidence reflection coefficient:

$$R_k = \frac{I_{n+1} - I_n}{I_{n+1} + I_n} \tag{2.61}$$

where R_n is the reflection coefficient of the nth interface, I_n is the acoustic impedance ($I = density \cdot velocity = \rho v$) of the nth layer (Lines and Newrick, 2004). If density is assumed constant, we have

$$R_k = \frac{v_{n+1} - v_n}{v_{n+1} + v_n} \tag{2.62}$$

We observed how the selected frequency bands gradually inject information until reconstructing the meaningful frequencies of the true model. The frequency multiscale scheme

shows to be stable during the process.

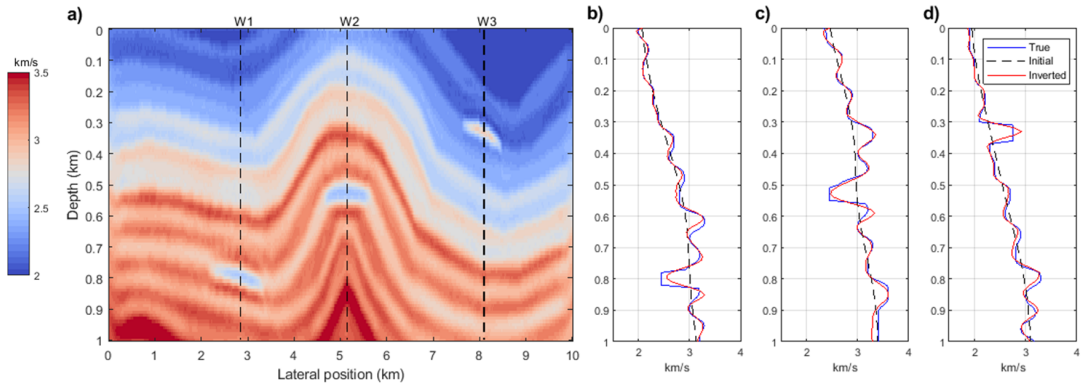

Figure 2.11: (a) Final model after 20 iterations. (b) Inverted velocity at the location of W1. (c) Inverted velocity at the location of W2. (d) Inverted velocity at the location of W3.

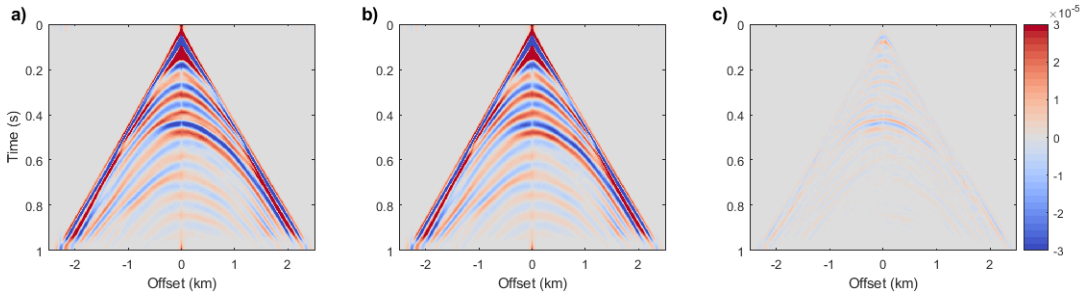

Figure 2.12: (a) Observed shot record. (b) Modelled shot record after 20 iterations. (c) Data residual = (a) - (b).

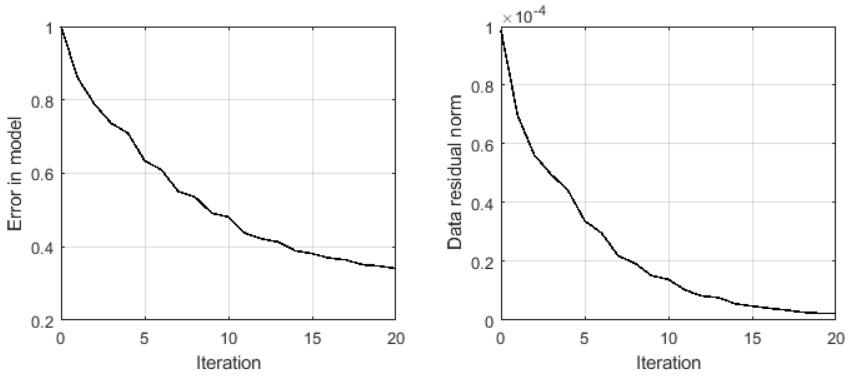

Figure 2.13: (a) Model error. (b) Data residual norms.

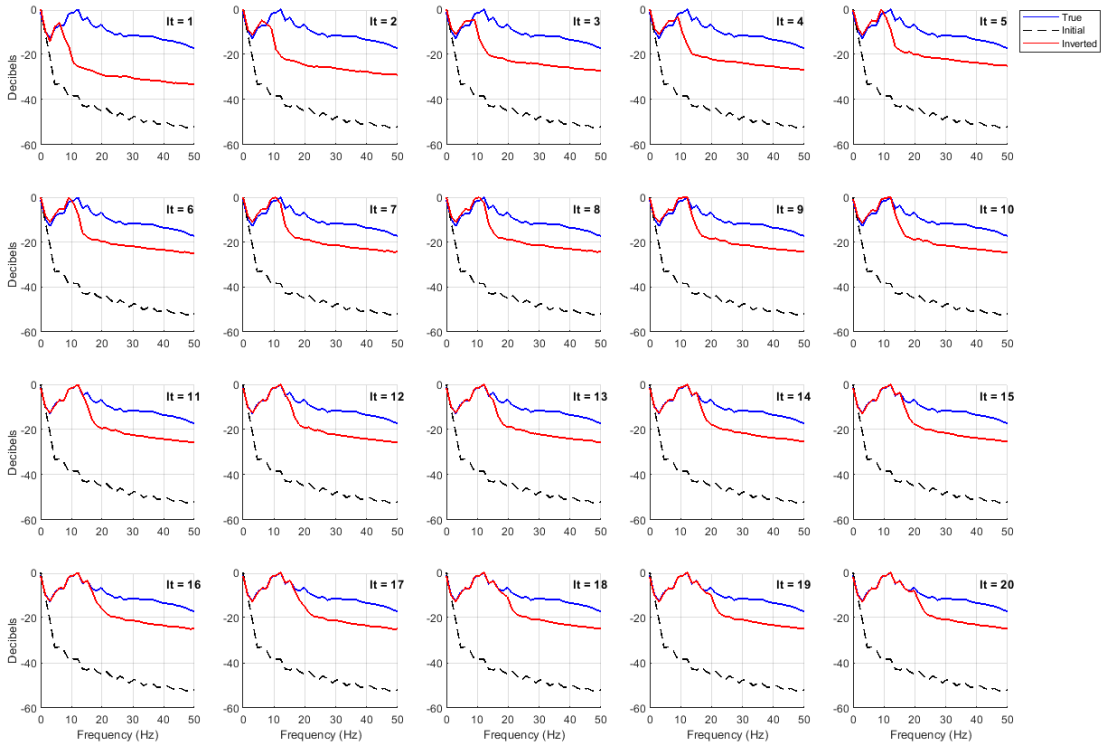

Figure 2.14: Evolution of the inverted-model reflectivity amplitude spectrum (red) with iteration. The true-model (blue) and initial-model (discontinuous black) reflectivity amplitude spectra are plotted as a reference.

How many shots are needed to compute the step-length?

In principle, we would have to employ all the available shots to compute the step-length that scales the gradient, which may be time-consuming depending on the computational resources. In this exercise, I take the first-iteration update direction and compute the step-length by employing a different number of shots. When one shot is used, it is located in the middle of the model. When more than one shot is employed, the shots are distributed evenly along the surface. The computed step-length with number of shots is plotted in Figure 2.15a. The model error with number of shots is plotted in Figure 2.15b. The step-length and the error in the model behave unstable when fewer than 20 shots are employed. In order to find out if these variations are meaningful, I compared the inverted model after 20 iterations for

the scenarios when 5 shots and 83 shots are used (Figure 2.16a-b). The model error and the data residual norms are plotted in Figure 2.17. The results show that whether we use 5 or 83 shots to compute the step-length is not relevant in regards to an impact on the final result for this small example, suggesting that the stability of the step-length and/or the model error may not be a useful diagnostic. A condition, when selecting the number of shots for the scaling process, would be to have enough shots that are able to sense the lateral variations across the model.

When I used a reduced number of shots, the same set of shots was employed in each iteration. Another possible approach would be to employ a different set of shots in each iteration. This would be helpful for the usage of more information across the model, which may be important for the case of complex models.

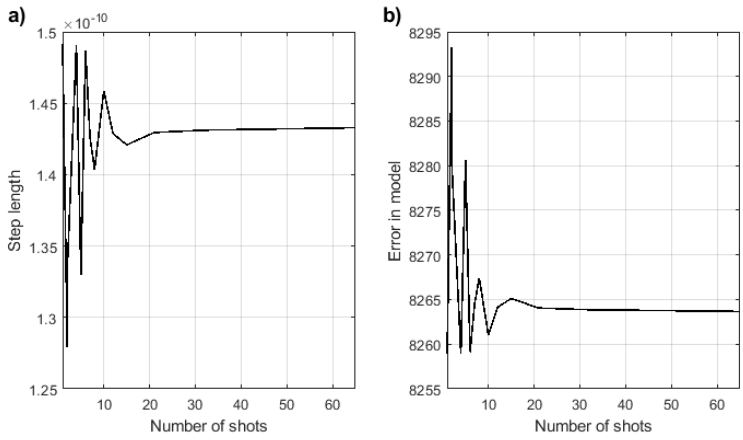

Figure 2.15: (a) Variation of the step-length with number of shots employed for its computation. (b) Model error obtained with the step-lengths in (a). The computations correspond to the first iteration.

Multiscale approach

The local minimization nature of FWI and the oscillatory character of the seismic data leave the waveform inversion exposed to cycle skipping. This phenomenon occurs when predicted and observed data differ by more than half a cycle (Warner et al., 2013). As a consequence of cycle skipping the inversion could become stuck in a local minimum. A good starting

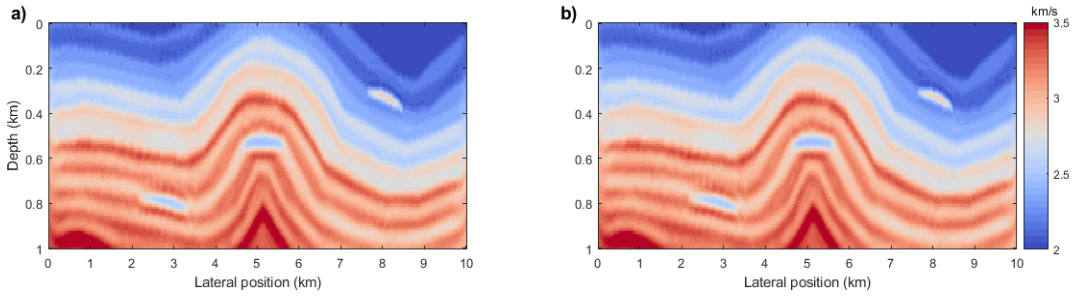

Figure 2.16: Inverted model after 20 iterations by using (a) 5 shots and (b) 83 shots to compute the step-length.

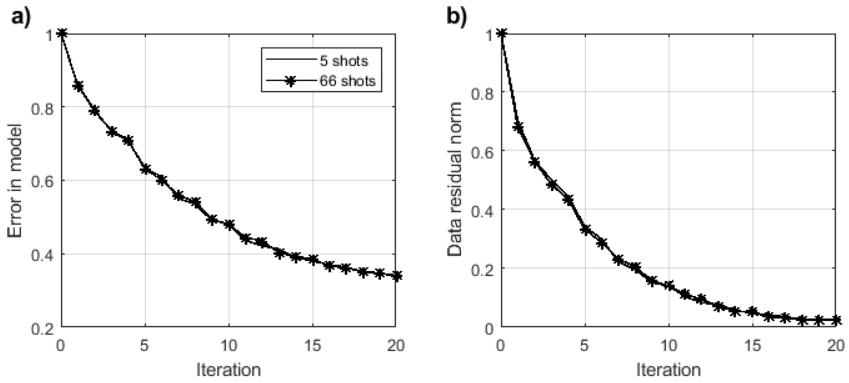

Figure 2.17: (a) Model error and (b) data residual norms by using 5 shots and all 83 shots to compute the step-length.

model, as well as seismic data with enough low-frequency content, are needed to avoid this problem. Pratt et al. (1998) showed that a multiscale approach can also help to mitigate this issue. A multiscale approach consists in starting the inversion with low frequencies and then introducing higher frequencies as we iterate. I have implemented a multiscale inversion in the previous example. In this section, the previous result is compared to the case when the inversion is carried out by employing all frequencies in each iteration. Figure 2.18 plots the inverted model for the multiscale approach and by employing all frequencies. A close look at the inverted velocity in three different positions in the model shows a superior performance of the multiscale approach. This is confirmed by the the model error and the data residual norms for both scenarios, which are plotted in Figure 2.19a-b. When the multiscale approach is applied, errors and norms tend to decrease with iteration, leading to

an overall convergence. On the other hand, when all frequencies are used in each iteration, the errors in the model and the data residual norms decrease at a higher rate in the first iterations, but after iteration 7 they become stuck.

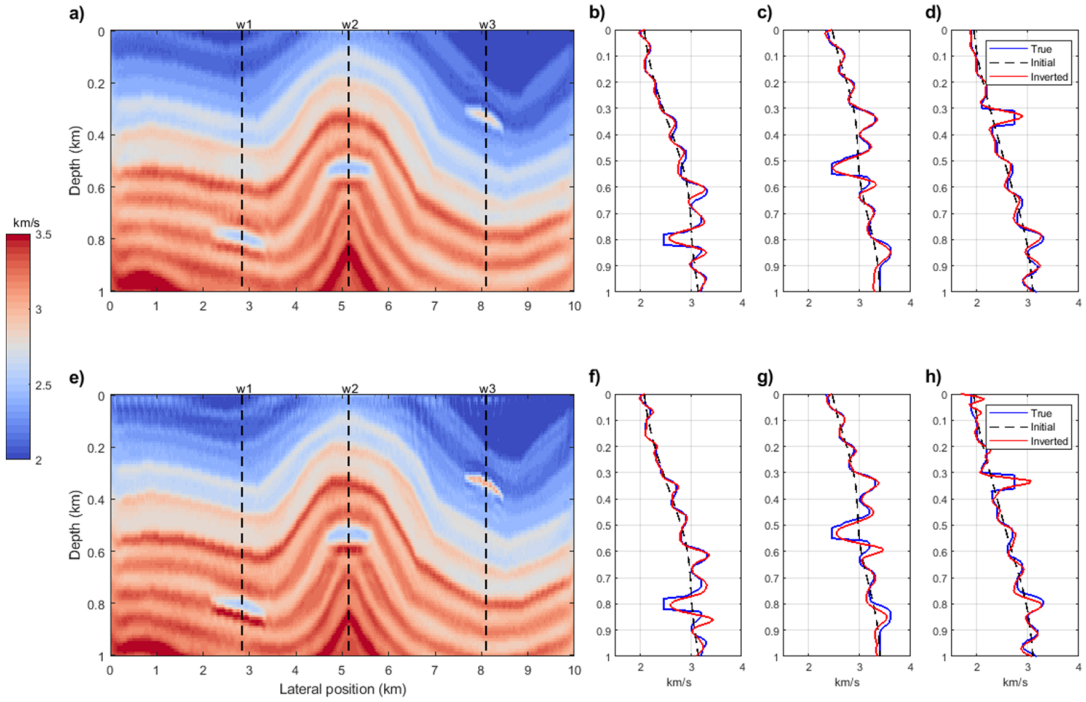

Figure 2.18: Result for a multiscale inversion: (a) inverted model, (b) inverted velocity at location of w1, (c) inverted velocity at location of w2, (d) inverted velocity at location of w3. Result obtained by employing all frequencies in each iteration: (e) inverted model, (f) inverted velocity at location of w1, (g) inverted velocity at location of w2, (h) inverted velocity at location of w3.

2.5 Conclusions

The theoretical framework of full waveform inversion under a constant-density acoustic approach was presented. The workflow recovers the P-wave velocity model from reflection seismic shot records. The process can be described as an iterative cycle that involves four main steps. First, synthetic shots are modelled and subtracted to the observed shot records

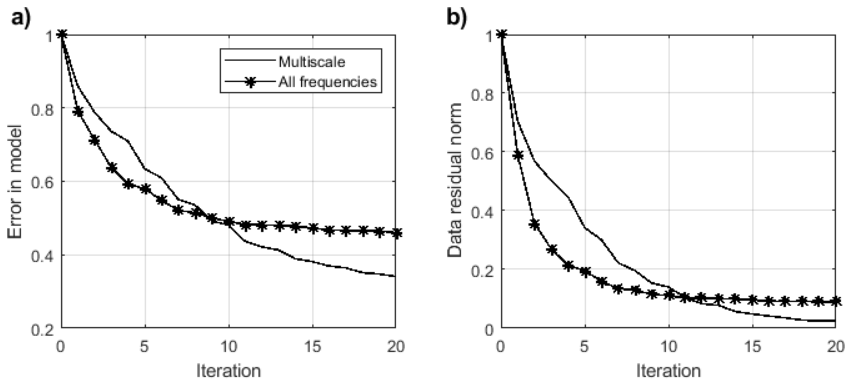

Figure 2.19: (a) Model error for the multiscale approach and by employing all frequencies. (b) Data residual norms for the multiscale approach and by employing all frequencies.

to produce the data residuals. Second, the gradient is generated by applying reverse time migration to the data residuals. A gradient-based step scheme was adopted as a consequence of approximating the inverse Hessian matrix by the identity matrix multiplied by a scalar. This simplification implies the necessity of preconditioning the gradient, which was done by applying the "deconvolution" imaging condition. The latter plays the role of the diagonal terms in the approximate Hessian, i.e., it compensates for the geometrical spreading. In order to avoid being stuck in a local minimum in the inversion, a multiscale approach was carried out and (in my example) showed to produce superior results when compared to the case when all frequencies are employed in each iteration. The third step consists in computing the step-length that scales the update direction to produce a velocity perturbation. Two methods were compared, one based on minimizing the objective function with respect to the step-length (Tarantola and Pica's approach), and another one consisting in backtracking line search and quadratic interpolation. Both methods produced similar results; however, the former only needs one forward modelling which leads to a smaller computational burden. Experiments on the number of shots needed to compute the step-length suggest that the operation is more stable as more shots are included. However, the uncertainty introduced by using only 5 shots did not have a significant impact on the final result for the model used in my example. I recommend employing enough shots distributed along the surface to allow

sensing lateral velocity changes in the model. In the fourth step, a new model is obtained by adding the velocity perturbation and the initial model. This new model is the input for the next iteration. A numerical example with a shallow anticline model corroborated the potential of FWI to estimate the subsurface velocity from seismic reflection shot records.

Chapter 3

Waveform inversion with one-way wave equation migration

3.1 Introduction

Virieux and Operto (2009), in their overview of FWI, pointed out that the difference between reverse time migration and full waveform inversion is that the seismic wavefield recorded at the receiver is backpropagated in the former, whereas the data residual is backpropagated in the latter. The RTM engine is commonly referred to in the process of the gradient calculation (Ma et al., 2012; Liu et al., 2012; AlTheyab et al., 2013; Guitton et al., 2012). Following this idea in the previous chapter, the FWI update direction was produced as the reverse time migration of the data residuals. The high computational cost of this process, which has to be iteratively repeated to update the model, represents an issue that may prevent the application of waveform inversion on real seismic surveys, where thousands of seismic shot records are commonly acquired. Therefore, finding alternatives to avoid the expense of RTM as the gradient engine is a strong motivation, central to the current chapter. Tarantola (1984) pointed out that the solution of the linearized seismic reflection inverse problem can be obtained by using the classical methods of migration and forward modelling. Margrave et al.

(2012a) retake this idea and propose iterative modelling, migration and inversion (IMMI), which aims to incorporate standard processing tools into the FWI workflow. In this sense, the gradient calculation can be performed with any convenient depth migration scheme, as it is proposed by Margrave et al. (2010), who employed phase-shift plus interpolation (PSPI) migration (Gazdag and Sguazzero, 1984). Gazdag and Sguazzero (1984) pointed out the superiority of PSPI over other one-way equation methods based on finite differences when migrating events have 60^o dips. PSPI has advantages and disadvantages when compared to RTM, a two-way wave equation migration method. The computational efficiency of PSPI and its relatively low memory requirements are important advantages over RTM (Etgen et al., 2009). A major strength of using PSPI, or frequency-domain migration in general, is the natural accommodation of frequency selection strategies which is very convenient in a multiscale inversion approach (Pratt et al., 1998). In the numerical example in Chapter 2, the inversion was carried out by using bandwidths of 5 Hz, starting from low frequencies and progressively increasing the frequencies as we iterate. Under this scheme, PSPI will be significantly faster than RTM, because PSPI migrates each frequency independently and the cost is directly proportional to how many frequencies are migrated. Another advantage of one-way propagators is pointed out by Margrave et al. (2010). One-way depth-stepping methods such as PSPI only correlate events moving down against those moving up, hence not producing artifacts such as the ones originated during the cross-correlation process in RTM. For example, events generated by the forward propagated source traveling in a certain direction may coincide with events generated by the backpropagated data moving nearly in the same direction. As these events are moving in the same direction, one cannot be the reflection of the other, but the cross-correlation between them may generate artifacts and produce a blurry character in the image (Margrave et al., 2010). Etgen et al. (2009) also mention that the RTM image contains significant amount of interbedded multiple energy and upward-scattered energy that may be considered as noise. A major advantage of RTM over PSPI is that the former can handle any spatial velocity variation to produce all kinds of

waves: reflections, refractions, diffractions, multiples (Etgen et al., 2009). This is important in FWI, because RTM can use the diving waves to recover long wavelengths (Kazei et al., 2013). Such disadvantage of PSPI will be discussed in Chapter 7, where I analyze the sensitivity of the waveform inversion to the initial model.

The following questions will be addressed in this chapter:

1) How do the RTM and the PSPI migrated data residual compare?

2) How can we make the PSPI migrated data residual similar to the reverse-time migrated data residual?

A single interface model will be used to answer these questions in a calibration exercise. We will observe that the PSPI migrated data residual has a phase difference with respect to the RTM result. I will show that this phase difference can be mitigated by applying two approaches for the PSPI migrated data residual: a) by using the integrated source wavelet to generate the source wavefield, or b) by using the original wavelet to generate the source wavefield and then applying impedance inversion. In the latter approach, I assume that the migrated stack approximates to normal-incidence reflectivity. The implications of this assumption will be discussed.

3.2 Altering the update direction calculation

Having described an FWI workflow in Chapter 2, I next set up a specific alteration in which the update direction is generated with a one-way wave migration method, rather than using the two-way wave operators in reverse time migration.

3.2.1 PSPI update direction

Following the ideas proposed by Margrave et al. (2012a), I make use of PSPI migration to generate the update direction. PSPI is a one-way wave equation migration that works in the frequency-space/wavenumber domain (Gazdag, 1978; Gazdag and Sguazzero, 1984).

The stack of the migration of the observed shots recorded at the receiver locations produces the migrated image (Im). The process consists in cross-correlating the upgoing receiver wavefield (U_r) and the downgoing source wavefield (D_s),

$$Im_{cc} = \int d\omega \sum_{s,r} U_r(\mathbf{x},\omega) D_s^*(\mathbf{x},\omega), \tag{3.1}$$

where * is complex conjugation. Margrave et al. (2010) showed that a deconvolution imaging condition compensates for the geometrical spreading and generates a better estimation of the reflectivity. The deconvolution imaging condition is given by

$$Im_{dec} = \int d\omega \sum_{s,r} \frac{U_r(\mathbf{x},\omega) D_s^*(\mathbf{x},\omega)}{D_s(\mathbf{x},\omega) D_s^*(\mathbf{x},\omega) + \eta I_{max}}, \tag{3.2}$$

where η is a small positive constant (typically 1%), and $I_{max} = \underset{x}{max}[D_s(\mathbf{x},\omega) D_s^*(\mathbf{x},\omega)]$.

In waveform inversion, we migrate the data residuals ($\Delta\mathbf{p} = p_{obs} - p_{cal}$), so that U_r corresponds to the upgoing data residual wavefield (ΔU_r) and the result is a reflectivity residual ($\Delta\mathbf{R}$):

$$\Delta\mathbf{R} = \int d\omega \sum_{s,r} \frac{\Delta U_r(\mathbf{x},\omega) D_s^*(\mathbf{x},\omega)}{D_s(\mathbf{x},\omega) D_s^*(\mathbf{x},\omega) + \eta I_{max}}. \tag{3.3}$$

In the previous section, I showed that the reverse-time migration with a deconvolution imaging condition in time domain applied to the data residuals produces a preconditioned gradient. In this section, I will apply PSPI migration with a deconvolution imaging condition in frequency domain, which produces reflectivity. This is shown in the following analysis:

In frequency domain, the deconvolution imaging condition is given by Claerbout (1971)

$$R = U/D, \tag{3.4}$$

where R is reflectivity, U is the downward continued recorded wavefield and D is the downward continued source wavefield (the upper cases imply Fourier domain). Equation 3.4 is a

restatement of

$$U = RD. \tag{3.5}$$

Equation 3.5 can be expressed in the time domain as a convolution,

$$u = r * d, \tag{3.6}$$

where the lowercase implies time domain. The deconvolution imaging condition in frequency domain is directly related to the convolutional model, where the recorded wavefield is produced by the convolution between the reflectivity and the source wavefield.

3.2.2 Calibrating the PSPI migration of the data residual

The following numerical example has the purpose of comparing the result of migrating the data residual by employing RTM and PSPI. This comparison will help calibrating the PSPI result.

The single horizontal interface model and the homogeneous model plotted in Figure 3.1a and b, respectively, were used for generating the observed and modelled shot records whose difference produce the data residual in Figure 3.3. Figure 3.2a plots the minimum-phase wavelet that was propagated through the models in order to generate the shot records. A fourth order finite-difference modelling algorithm, assuming constant-density and an acoustic framework, was used in the forward modelling process.

The result of migrating the data residual with a deconvolution imaging condition by applying RTM and PSPI is shown in Figure 3.4. The original wavelet (Figure 3.2) employed for generating the shot records, was used to produce the source wavefield in both cases. A comparison within the normalized migrated trace from the middle of the section shows a phase difference (approximately -60^o) between the RTM and the PSPI result. This phase difference is significantly reduced if we apply impedance inversion to the PSPI-migrated data residuals (Figure 3.5). The impedance inversion integrates the migrated traces over

depth. Alternatively, we can also use the negative integrated wavelet to generate the source wavefield for the case of PSPI, and obtain a similar result (Figure 3.6).

In this thesis, I will generate the PSPI update direction by employing the original wavelet to produce the source wavefield during the migration process and then applying impedance inversion to the stack of the migrated shots. This approach assumes that the migrated stack obtained by applying PSPI migration with a deconvolution imaging condition approximates to normal-incidence reflectivity. The implications of this approximation will be discussed later.

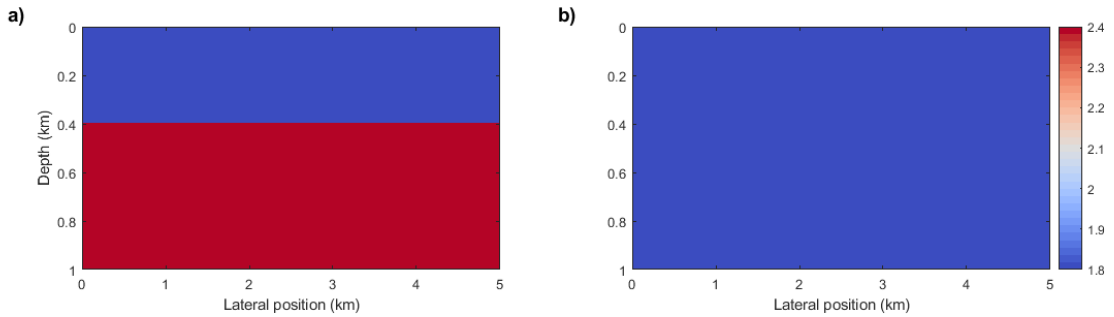

Figure 3.1: (a) Single horizontal interface model. (b) Homogeneous initial model with the velocity of the first layer in the model (a).

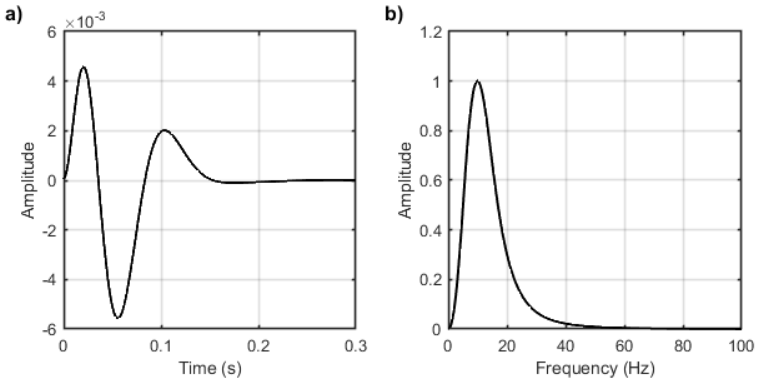

Figure 3.2: (a) Minimum-phase wavelet. (b) Amplitude spectrum.

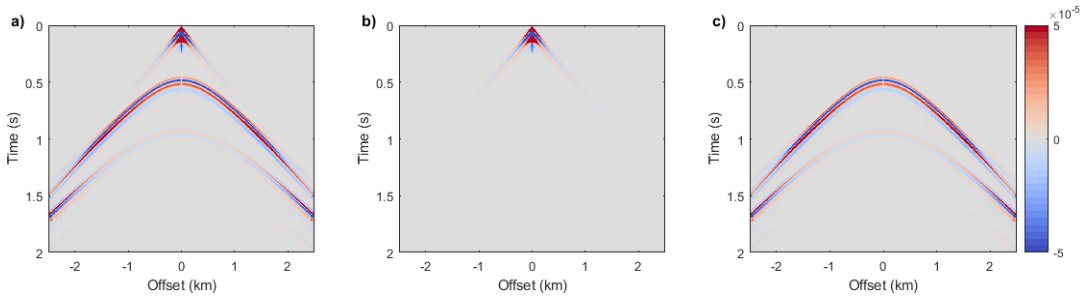

Figure 3.3: (a) Observed shot record obtained by propagating the wavelet in Figure 3.2 through the model in Figure 3.1a. (b) Modelled shot record obtained by propagating the wavelet in Figure 3.2 through the model in Figure 3.1b. (c) Data residual = (a) - (b).

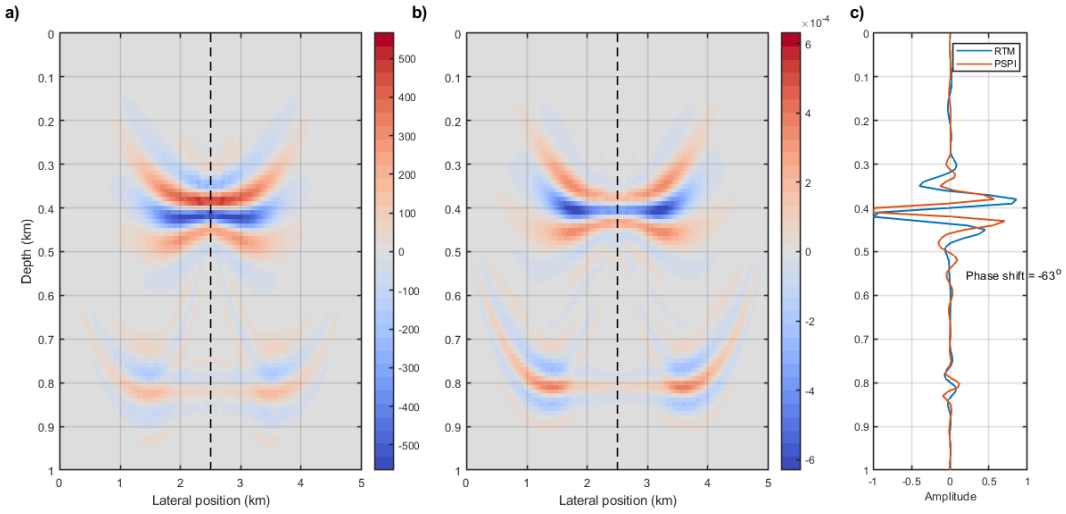

Figure 3.4: (a) Migrated data residual by applying RTM and using the wavelet in Figure 3.2 to generate the source wavefield. (b) Migrated data residual by applying PSPI migration and using the wavelet in Figure 3.2 to generate the source wavefield. (c) Normalized migrated trace taken from the middle of the section for RTM (blue) and PSPI (red).

3.2.3 Impedance inversion

Since the reflectivity residual is estimated after applying PSPI migration with a deconvolution imaging condition to the data residuals, we require an impedance inversion in order to derive the impedance update, which corresponds to a velocity update in the constant density acoustic approximation.

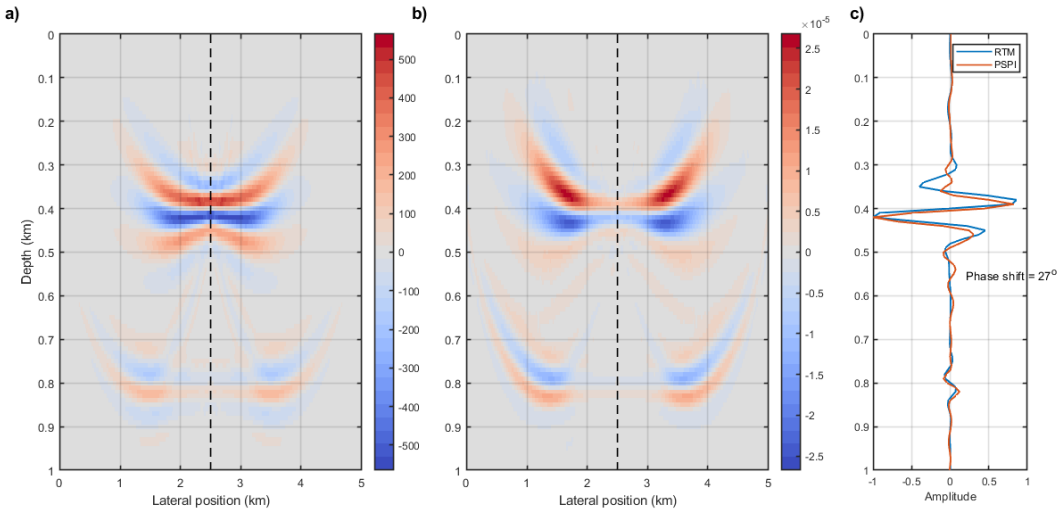

Figure 3.5: (a) Migrated data residual by applying RTM and using the wavelet in Figure 3.2 to generate the source wavefield. (b) Migrated data residual by applying PSPI migration, using the wavelet in Figure 3.2 to generate the source wavefield and applying impedance inversion. (c) Normalized migrated trace taken from the middle of the section for RTM (blue) and PSPI (red).

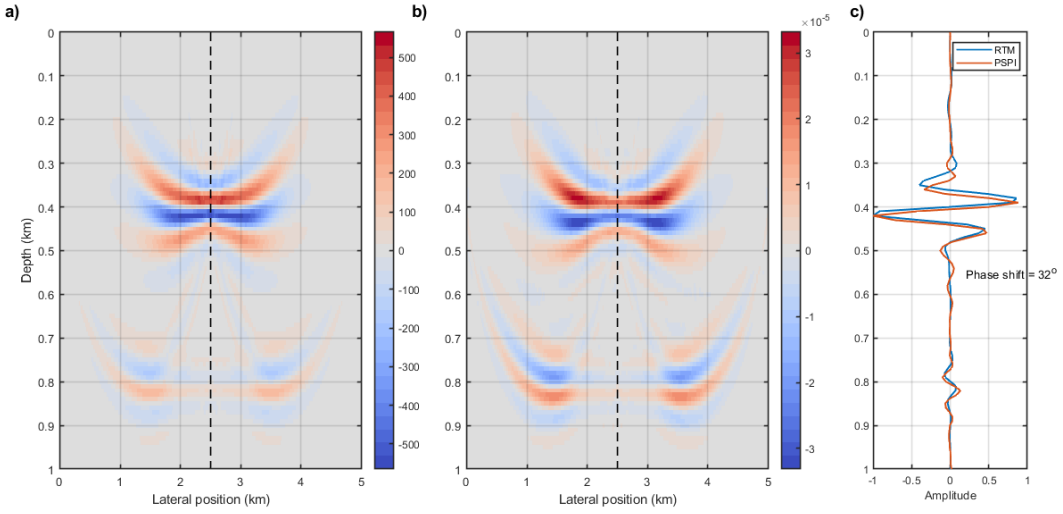

Figure 3.6: (a) Migrated data residual by applying RTM and using the wavelet in Figure 3.2 to generate the source wavefield. (b) Migrated data residual by applying PSPI migration and using the negative of the integrated wavelet in Figure 3.2 to generate the source wavefield. (c) Normalized migrated trace taken from the middle of the section for RTM (blue) and PSPI (red).

We start from the definition of the normal-incidence reflectivity normalized by Δz

$$R(z) = \frac{I(z + \frac{\Delta z}{2}) - I(z - \frac{\Delta z}{2})}{[I(z + \frac{\Delta z}{2}) + I(z - \frac{\Delta z}{2})]\Delta z}, \tag{3.7}$$

where $I(z + \frac{\Delta z}{2})$ and $I(z - \frac{\Delta z}{2})$ are the impedances above and below the interface, and $R(z)$ is the reflectivity at the interface. The term Δz that appears in the divisor part in equation 3.7 is explained by Waters (1987), who pointed out that the reflection coefficients are obtained at constant sampling rates. They really represent the product of the reflectivity and the sampling rate.

Assuming small impedance contrast, equation 3.7 can be approximated as

$$R(z) = \frac{\Delta I(z)}{2I(z)\Delta z}. \tag{3.8}$$

Rearranging equation 3.8

$$\frac{\Delta I(z)}{I(z)\Delta z} = 2R(z), \tag{3.9}$$

if this difference is considered to be infinitesimal, using

$$\frac{d}{dz}\log u = \frac{1}{u}\frac{du}{dz}, \tag{3.10}$$

we can rewrite equation 3.9 as

$$d\log I(z) = 2R(z)dz, \tag{3.11}$$

which is integrated to obtain

$$\log I(z) = 2\int_0^z dz' R(z') + \log I_0. \tag{3.12}$$

Raising e to the power of the right-hand side, we finally arrive at

$$I(z) = I_0 e^{(2\int_0^z dz' R(z'))}. \tag{3.13}$$

Three ways of applying equation 3.13 are considered:

1. Impedance inversion in depth domain, in which case we integrate the reflectivity in depth domain as it is stated in equation 3.13.

2. Impedance inversion in time domain, in which case we integrate the reflectivity in time domain, requiring to convert the reflectivity from depth to time by employing the velocity model. Depth and time are related through two-way propagation via

$$t(z) = 2\int_0^z \frac{dz'}{v(z')}. \tag{3.14}$$

   Thus, the time expression of equation 3.13 is

$$I(t) = I_0 e^{(2\int_0^t dt' R(t'))}. \tag{3.15}$$

3. Impedance inversion in frequency domain, in which case the reflectivity is integrated in the frequency domain, according to Waters (1987), Ferguson and Margrave (1996). The reflectivity in frequency domain is expressed as

$$\hat{R}(\omega) = F[(R(t)] \tag{3.16}$$

   where the $\hat{(\cdot)}$ specifies a variable in frequency domain, and $F(\cdot)$ is a Fourier transform operator. The integration of the reflectivity is done through spectral division by the first power of frequency and an appropriate phase shift

$$\int_0^t dt' R(t')) = F^-\left(\hat{R(\omega)}\frac{-i}{\omega}\right), \tag{3.17}$$

   where $F^-(\cdot)$ is the inverse Fourier operator. Thus, the impedance inversion is

$$I(t) = I_0 e^{\left(2F^-\left(\hat{R(\omega)}\frac{-i}{\omega}\right)\right)}. \tag{3.18}$$

The impedance inversion in depth, time and frequency domains (equations 3.13, 3.15, and 3.18) were compared using a 1D synthetic example. We assumed constant density, so that the impedance inversion produces velocity as an output. The true and initial velocities are plotted in Figure 3.7a, and their correspondent reflectivities are plotted in Figure 3.7b. The reflectivity residual (ΔR), i.e., difference between the true and initial reflectivity, is plotted in Figure 3.7c. Figure 3.7d shows the reflectivity residual with random noise (S/N=5).

The update direction is obtained in a two-step process that consists in applying impedance inversion to the reflectivity residual ($Imp(\Delta R)$) and subtracting the mean value of $Imp(\Delta R)$. The latter operation preserves the relative velocity variations. The velocity perturbation is produced by scaling the update direction. In this case, I directly computed a scalar that minimizes the differences between the update direction and the velocity residual (true - initial velocities). The updated velocity model is the sum of the velocity perturbation and the initial model. The updated velocities computed from the reflectivity residual with and without noise are plotted in Figures 3.8a-b. The indexes 1, 2 and 3 correspond to the integration part in depth, time and frequency domains, respectively. The inverted velocity error is plotted in Figure 3.9. The results with no noise show that the implementation in depth domain is able to reproduce better the true velocity; however, in the presence of noise, the frequency domain implementation is more stable and produces the best result. For this reason, I chose to employ the impedance inversion in the frequency domain when implementing the waveform inversion with one-way wave equation migration.

3.3 Numerical example

The synthetic data set used in the numerical example in Chapter 2 is employed in this section in order to compare the PSPI to the RTM update direction in the first iteration. An example of the application of PSPI migration with a deconvolution imaging condition to the data residuals is plotted in Figure 3.10a. The same is plotted for the case of RTM in Figure

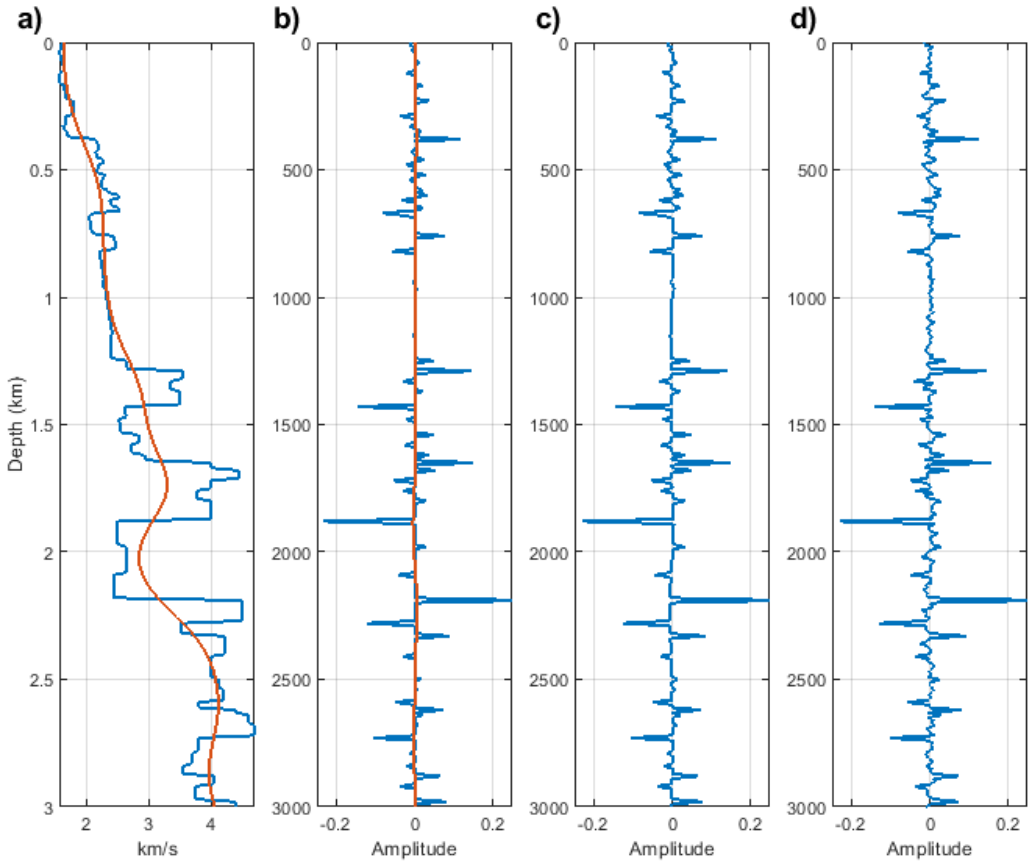

Figure 3.7: (a) True (blue curve) and initial (red curve) velocities. (b) True (blue curve) and initial (red curve) reflectivities. (c) Reflectivity residual = true reflectivity - initial reflectivity. (d) Reflectivity residual with random noise.

3.11b. The amplitudes have been normalized to facilitate the comparison. Although there are changes in the amplitude across the model, the most relevant difference is the phase shift (similar to what was reported in the calibration exercise). This is better described in Figure 3.11a, where a trace located in the middle of the model is plotted for each case. Figure 3.11b plots the result of applying impedance inversion to the PSPI-migrated data residuals (red curve), and compares this curve to the result of applying RTM (blue curve). The phase difference of the PSPI update direction with respect to the RTM update direction has been reduced, and we can proceed to scale the PSPI update direction by using a line search method to obtain the velocity perturbation.

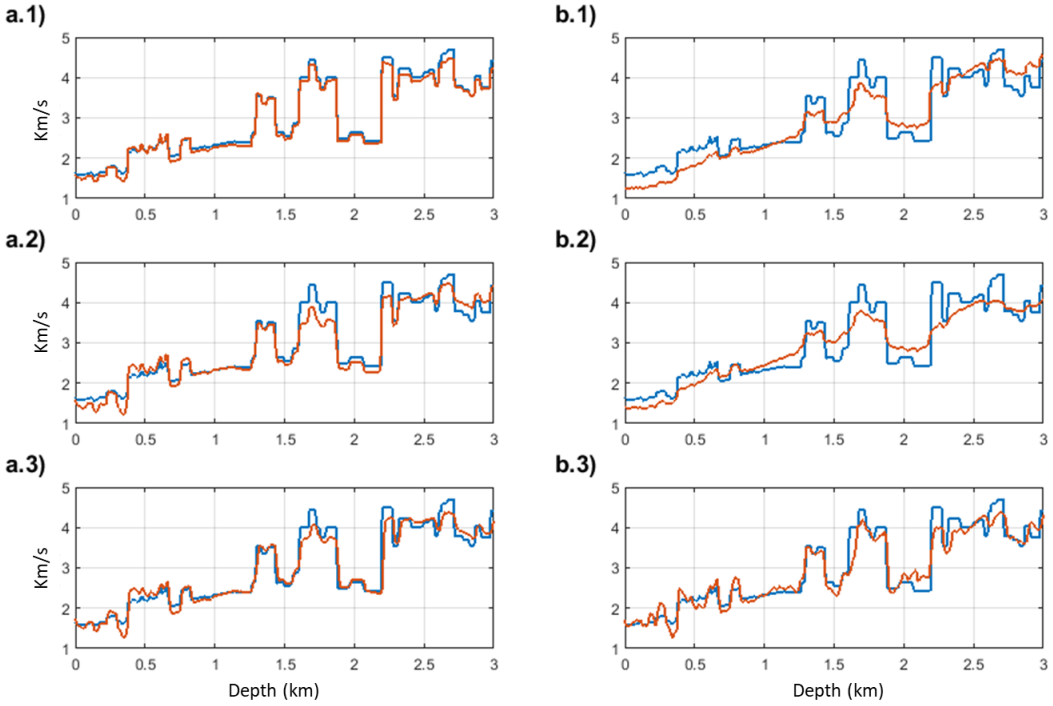

Figure 3.8: Velocity updates (red curve) computed from a reflectivity residual (a) without and (b) with random noise. The indexes 1, 2 and 3, correspond to the integration part in depth, time and frequency domains. The blue curve represents the true velocity update, i.e., the difference between the true and initial velocities.

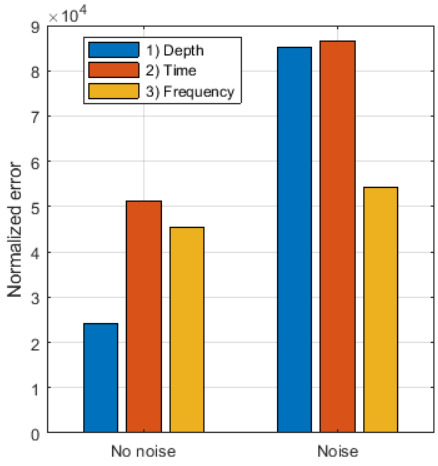

Figure 3.9: Velocity error for the scenarios without and with noise. The depth, time and frequency domain implementations are plotted in blue, red and orange, respectively.

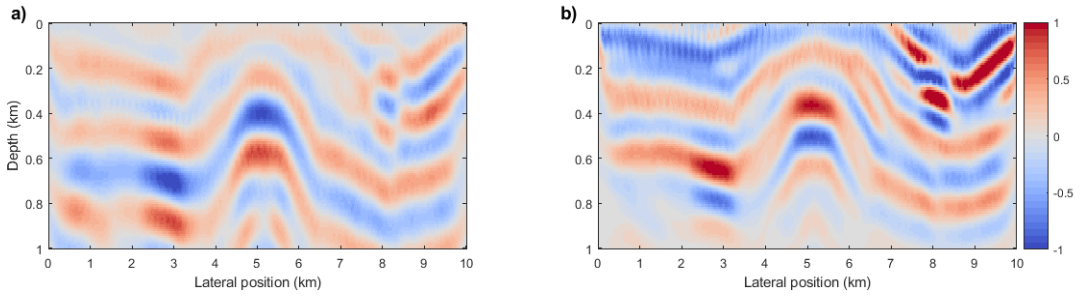

Figure 3.10: (a) Normalized data residuals migrated with (a) PSPI and (b) RTM.

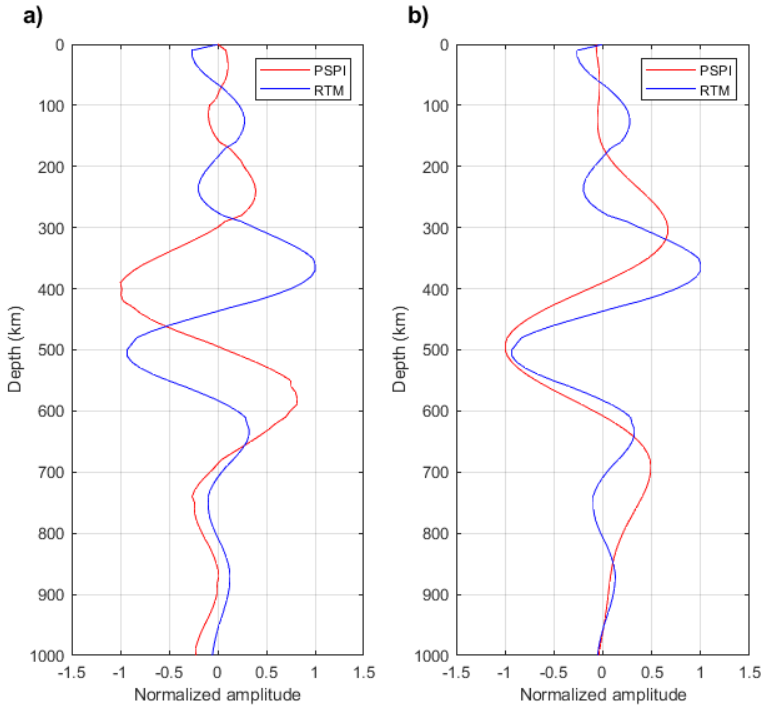

Figure 3.11: (a) Migrated data residual for PSPI ($Stk[Mig_{PSPI}(\Delta p)]$) and RTM ($Stk[Mig_{RTM}(\Delta p)]$). (b) Migrated data residual for PSPI with impedance inversion ($Imp[Stk[Mig_{PSPI}(\Delta p)]]$) and migrated data residual for RTM ($Stk[Mig_{RTM}(\Delta p)]$). $Stk(\cdot)$, $Mig(\cdot)$ and $Imp(\cdot)$, indicate stack, migration and impedance inversion operators, respectively.

3.3.1 Scaling the PSPI update direction

The data validation technique based on Tarantola and Pica's approach (Section 2.3.1) was employed to scale the PSPI update direction. In this case, the update direction already has

model units after applying the impedance inversion, so that the step-length μ is dimensionless as it is shown next.

Recalling equations 2.45, 2.46 and 2.47 stated in Section 2.3.1, the step-length μ, the derivative operator $\mathbf{F}$ and ϵ are

$$\mu_k = \frac{[\mathbf{F}_k\mathbf{\Phi}_k]^\dagger[\mathbf{p}_{obs} - \mathbf{f}(\mathbf{m}_k)]}{[\mathbf{F}_k\mathbf{\Phi}_k]^\dagger[\mathbf{F}_k\mathbf{\Phi}_k]}.$$

$$\mathbf{F}\mathbf{\Phi}_k = \lim_{\epsilon\to 0}\frac{\mathbf{f}(\mathbf{m}_k + \epsilon\mathbf{\Phi}_k) - \mathbf{f}(\mathbf{m}_k)}{\epsilon},$$

$$\epsilon = 0.05\sqrt{\frac{< \mathbf{m}_k, \mathbf{m}_k >}{< \mathbf{\Phi}_k, \mathbf{\Phi}_k >}}.$$

Denoting the units operator by $[\cdot]_u$, we have that the units of ϵ are

$$[\epsilon]_u = \sqrt{\frac{[m^2]_u}{[\Phi^2]_u}} = \frac{[m]_u}{[m]_u} = [1]_u. \tag{3.19}$$

On the other hand, the units of the operator $\mathbf{F}$ applied to $\mathbf{\Phi}$ are

$$[\mathbf{F}\mathbf{\Phi}]_u = \frac{[data]_u}{[\epsilon]_u} = \frac{[data]_u}{[1]_u} = [data]_u. \tag{3.20}$$

Finally, the units of μ_k in equation 2.48 are

$$[\mu_k]_u = \frac{[data]_u[data]_u}{[data]_u[data]_u} = \frac{[data^2]_u}{[data^2]_u} = [1]_u. \tag{3.21}$$

The units that result from multiplying Φ_k by μ_k are

$$[\mu_k\Phi_k]_u = [1]_u[\Phi]_u = [m]_u, \tag{3.22}$$

the model units.

3.3.2 Inversion workflow and results

The workflow that incorporates the PSPI update direction is shown in Figure 3.12. The main changes, concerning the FWI workflow in Chapter 2 (Figure 2.2), are highlighted in red boxes. The depth-to-time and time-to-depth conversions are accomplished by using the current velocity model. The scalar μ, which multiplies the update direction to produce the velocity perturbation, was computed by Tarantola and Pica's approach (section 2.3.1). The same multiscale approach, implemented in the example shown in Chapter 2, was applied so that low frequency bands are migrated in the first iterations and higher frequencies are introduced as we iterate (Table 2.1). The inverted model after 20 iterations for the RTM and the PSPI cases are plotted in Figures 3.13a and 3.13e, respectively. Figures 3.13b-d plot the inverted velocity at the lateral position of well w1 (2840m), w2 (5140m) and w3 (8100m) for the RTM case. The same is plotted for the case of PSPI in Figures 3.13f-h. Apparently the outcomes are similar; however, the comparison between the data residual after 20 iterations (Figures 3.14c and 3.14f) reports significant differences that are more evident in the comparison of the model error and the data residual norms plotted in Figure 3.15a and 3.15b.

We observe that the data residuals are significantly affected by the first arrivals that include the direct wave, refracted waves and diving waves. These waves are handled by RTM migration, which incorporates long wavelength information from the diving waves (Kazei et al., 2013), improving in turn, the forward modelling of the first arrivals producing smaller data residuals. On the other hand, PSPI uses mainly primary reflections to reconstruct the velocity model, which limits its capability to recover low frequency components. Without such information the first arrivals are not properly modelled and diminished in the data residuals. This aspect will be further analyzed in Chapter 7.

Another aspect that explains the poor performance of PSPI is the remnant phase dif-

ference that persists between the RTM and PSPI update directions even after applying the impedance inversion (Figure 3.5). I will show in Chapter 4 that the incorporation of well-log information helps to overcome the remnant phase shift of the PSPI update direction.

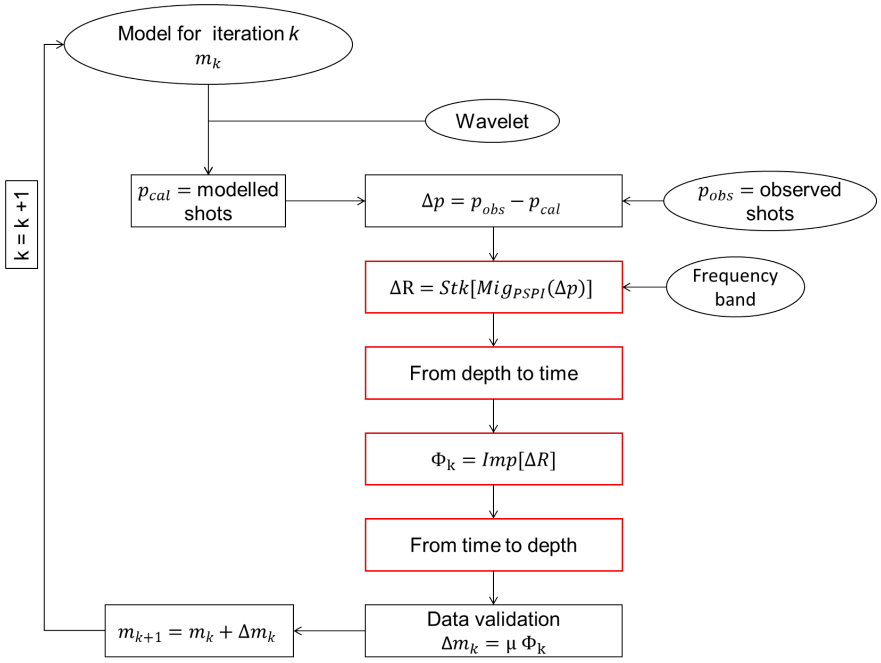

Figure 3.12: Workflow for waveform inversion with one-way wave equation migration. The PSPI migration and stack of the data residuals (Δp) produces the reflectivity residual (ΔR), which is converted into an update direction (Φ) via impedance inversion. Jumps from depth to time and vice versa are carried out by employing the current model.

3.4 Discussion

The process adopted in this thesis, for generating the update direction, consists in applying PSPI migration with a deconvolution imaging condition to the data residuals, stack, and then impedance inversion. This approach assumes that the migrated stack approximates to normal-incidence reflectivity. Approximating reflectivity by normal-incidence reflection coefficient normalized by Δz (equation 3.7) implies two separate approximations:

1. Approximating angle-dependent reflection coefficient with normal-incidence reflection coefficient.

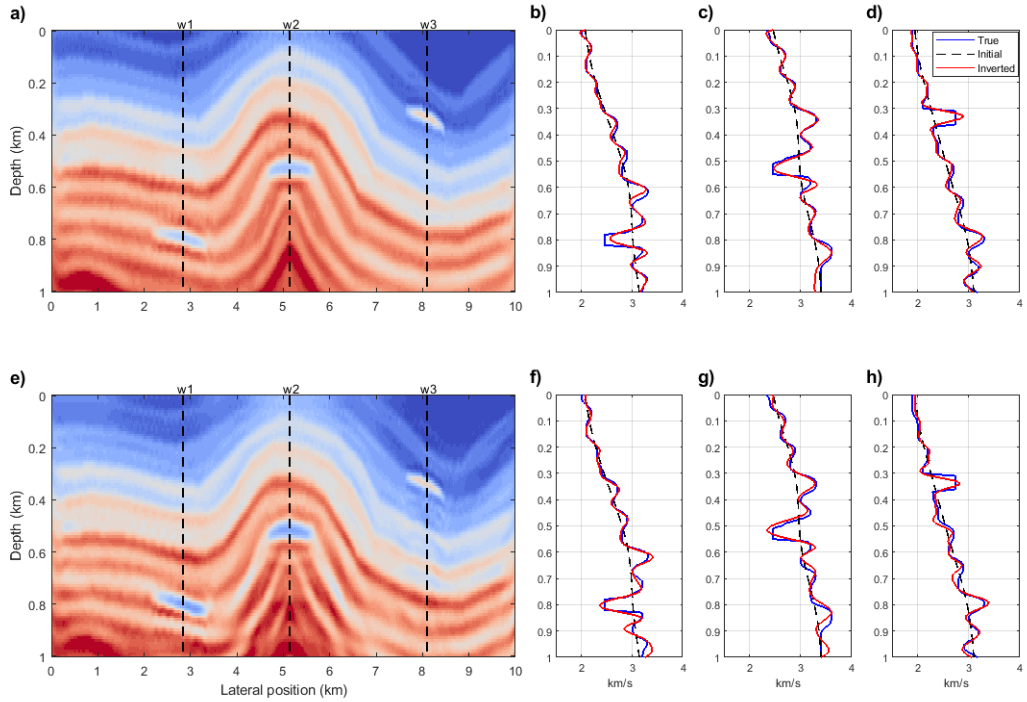

Figure 3.13: Inverted model after 20 iterations and inverted velocity at the locations of w1, w2 and w3 for (a-d) RTM update directions and (e-f) PSPI update directions.

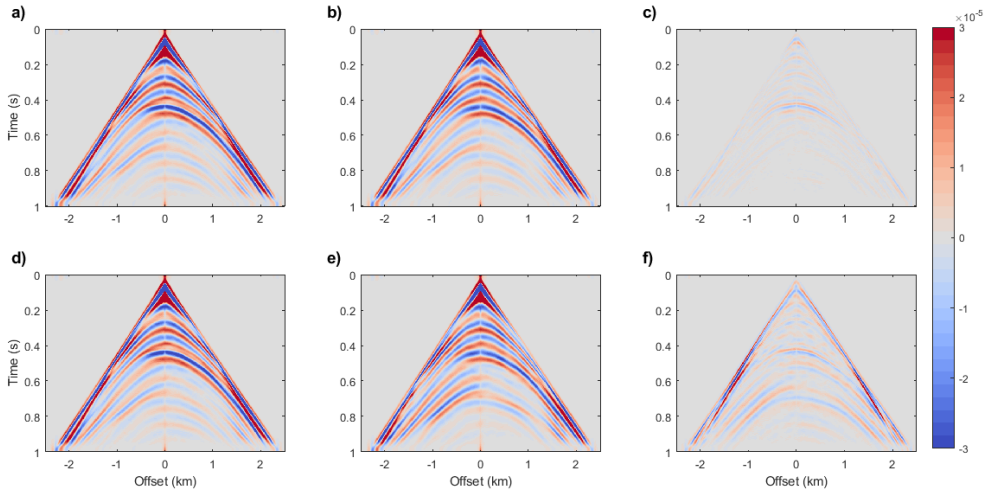

Figure 3.14: True shot record, Modelled shot record and data residual after 20 iterations for (a-c) RTM update directions and for (d-f) PSPI update directions.

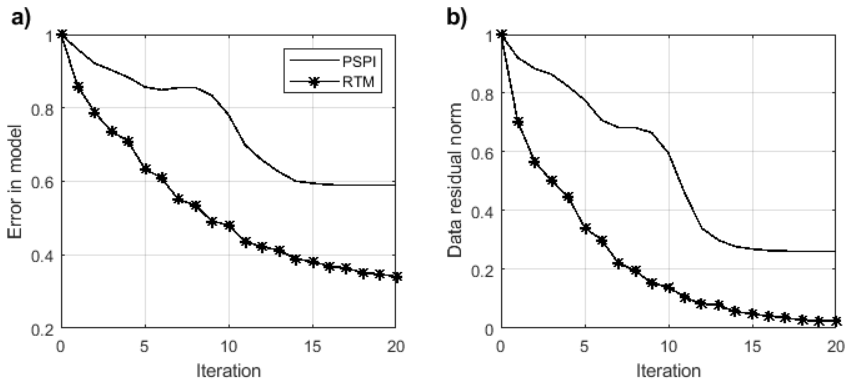

Figure 3.15: (a) Model error for RTM and PSPI update directions. (b) Data residual norms for RTM and PSPI update directions.

This approximation ignores the amplitude changes with angle (AVA) that actually describe the reflectivity as a distribution which is an angle-dependent reflection coefficient. The implication of this approximation can be better explained by Figure 3.16, taken from Zhang et al. (2007). It shows angle-domain, common-image gathers from five locations at the Sigsbee2a model data set (Paffenholz et al., 2002). It is clear that the amplitude corresponding to short-range angles differs from middle-range and far-range angles. This is demonstrated by the stacked images of different angle ranges plotted in Figure 3.17, also taken from Zhang et al. (2007). It follows that the full stack will be different than the stack of the short-range angles. Approximating the migrated stack to a zero-offset reflectivity will possibly introduce errors that are beyond the scope of this research. One possible way to deal with this problem, in future work, can be the use of true-amplitude common-angle, common-image gathers, such as the ones produced by Zhang et al. (2007), and select only short-range angles to produce the stack. Another possibility is directly applying impedance inversion in the angle gathers, as it is done in AVO/AVA inversion.

2. Approximating dipping reflectors to locally-horizontal reflectors.

   Equation 3.13 obtains impedance from normal-incidence reflection coefficients normalized by dz, which demands that the subsurface is constituted by horizontal layers. This

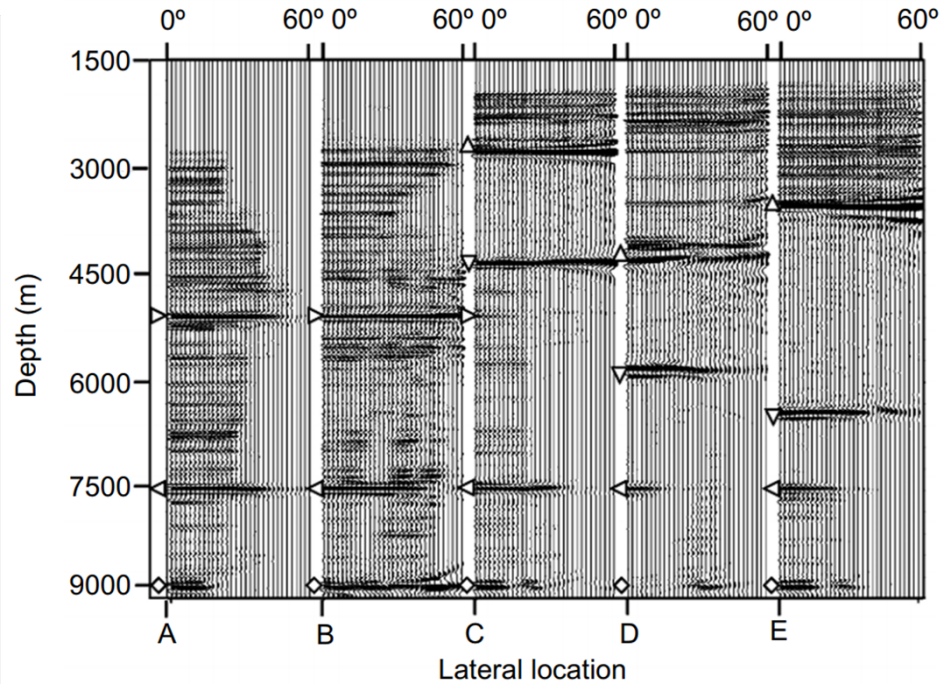

Figure 3.16: Examples of true-amplitude migrated angle-domain, common-image gathers taken from Zhang et al. (2007).

assumption is contravened in the presence of dipping layers, which may introduce a bias in the result of impedance inversion. This problem can be mitigated by dividing the reflectivity by cosine(dip) before integrating for impedance. This operation projects the reflectivity from the vector dz to the vector dn, normal to the dipping reflector. Another way to address this problem is given by Karimi (2015), who implemented impedance inversion in the stratigraphic coordinate system, where the vertical direction is normal to reflectors and seismic traces represent normal incidence seismograms.

3.5 Conclusions

In Chapter 2, the update direction in the FWI workflow was obtained by applying reverse time migration to the data residuals with a deconvolution imaging condition as a preconditioner. This update direction only needs to be multiplied by a scale factor to be converted

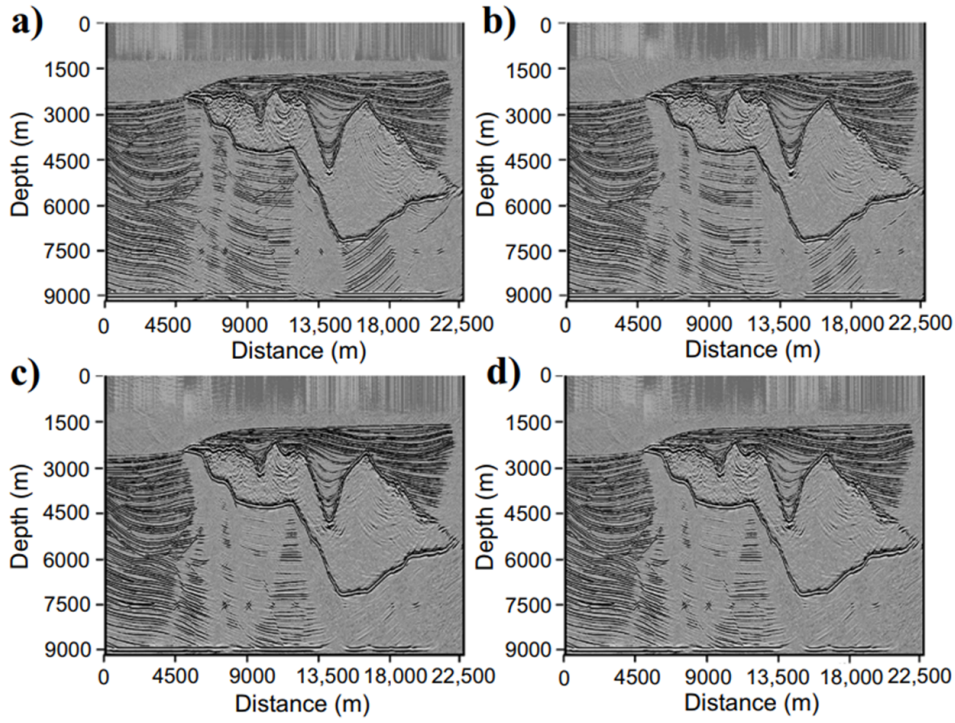

Figure 3.17: The stacked Sigsbee2a images of different angle ranges. (a):0^o-10^0; (b):10^o-20^0; (c):20^o-30^0; (d):30^o-40^0. Figure taken from Zhang et al. (2007).

into a velocity perturbation. In this chapter, in contrast, based on certain concepts of Margrave, such as iterated modeling, migration and inversion, a row update direction is obtained by applying a one-way wave-equation migration, i.e., PSPI. A calibration exercise using a single interface model showed that the stack of PSPI-migrated data residuals has a phase difference with respect to the RTM update direction that may prevent its direct use to generate the model perturbation. It was shown that this phase difference is reduced by applying impedance inversion to the PSPI result. A similar effect can be obtained by using the integrated source wavelet to generate the source wavefield during the PSPI migration process. In this research, I adopted the impedance inversion approach to generate the PSPI update direction. I compared three impedance inversion approaches that can be classified according to the domain where the integration part is done: depth, time and frequency. In a 1D noise-free synthetic example, depth impedance inversion produced the best result. But

in the presence of noise, the depth and time approaches become unstable, which does not happen in the frequency domain. The latter was chosen to be implemented in the waveform inversion. The synthetic examples showed that even after applying impedance inversion to the PSPI migrated data residuals, there is a remnant phase difference between the PSPI and RTM update directions that affects the convergence when PSPI is implemented. I will show in the next chapter that the incorporation of log information provides the elements for further correction of the phase during the scaling step.

Chapter 4

Well-log validated waveform inversion

4.1 Introduction

In Chapter 3, I introduced a waveform inversion employing one-way wave equation migration (PSPI) to generate the update direction. This perspective is based on the IMMI idea (Margrave et al., 2012a), which proposes substituting key elements of the FWI workflow by standard processing techniques already available in the industry. The potential of the PSPI update direction was shown with a numerical example, and the role of the impedance inversion to partially correct the update direction phase was pointed out. However, there is a remnant phase that prevents the method from effective convergence. The incorporation of well-log data allows us to include in FWI an additional stabilizing component. The incorporation of well-log information is a relevant contribution of IMMI, as a substitute for the step-length computed by data validation methods. Margrave et al. (2010) suggest to call this process "calibrating the update direction" or "well calibration", which is comparable to the standard process of impedance inversion by matching to well control. I will interchangeably use the terms "well-log validation" and "log calibration" in this thesis. The current Chapter will describe the process of well-log validation. It will be shown that this technique not only reduces the computational burden in the waveform inversion, but also overcomes the

remnant phase problem of the PSPI update direction.

4.2 Well-log validation process

I retake the synthetic data set employed in the numerical examples in Chapters 2 and 3. A well-log, simulated at the middle of the anticline model (Figure 4.1a), provides the P-wave velocity, denoted as $v^{(w)}$, that will be used in the calibration process. The log aperture goes from 400 to 900m. The implementation of log validation makes use of the velocity residual in the well location defined as

$$\delta v_k^{(w)} = v^{(w)} - v_k^{(w)}, \tag{4.1}$$

where $v_k^{(w)}$ is the velocity at the well location extracted from the current model and k is the iteration number.

I will describe the well-log validation process for the first iteration of the waveform inversion with one-way wave equation migration so that the current model is the initial model in Figure 4.1b, and the update direction is the one generated by applying PSPI migration and impedance inversion to the data residuals (Figure 4.2). The frequency band for iteration 1 is 1-6Hz. The velocity residual at the well location is plotted in Figure 4.3c. The process can occur in time or depth domains. I chose time because the velocity update is generated in this domain after applying impedance inversion in the frequency domain. Furthermore, in time domain we can directly apply a filter to $\delta v^{(w)}$ with the same frequency band employed to generate the update direction during the migration. The objective is to make the update direction in the well location, $\Phi_k^{((w)}$ (Figure 4.4a), look similar to $\delta v^{(w)}$ (Figure 4.4b). To do so, we estimate the least-squares amplitude scalar a and the least-squares constant-phase rotation φ that minimize the quantity

$$\int [\delta v_k^{(w)} - a\ phsrot(\Phi_k^{(w)}, \varphi)]^2 dt, \tag{4.2}$$

where $phsrot(\cdot)$ is an operator that rotates the phase of $\Phi_k^{((w)}$ by an angle φ.

With the scalar a and the phase rotation angle φ we can obtain a matched filter λ (Figure 4.4c), so that a velocity perturbation (Figure 4.4d) is produced when λ is convolved with the update direction. Since this process is done in time, we use the current velocity model to take the velocity perturbation to depth (Figure 4.5), where the model update is done.

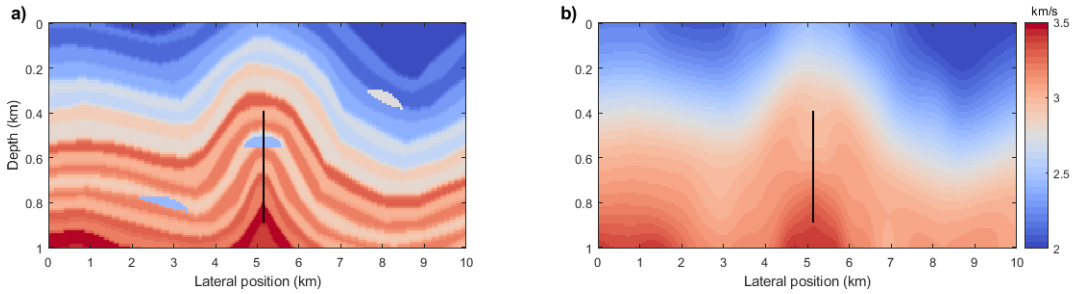

Figure 4.1: (a) True velocity model. (b) Initial velocity model. The black line represents the well aperture used in the well-log validation process.

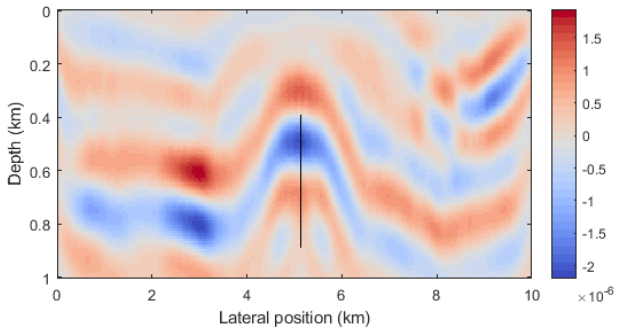

Figure 4.2: Update direction for the first iteration. The black line represents the well aperture used in the well-log calibration process.

4.3 Workflow of log-validated waveform inversion

Figure 4.6 shows the workflow for log-validated waveform inversion with one-way equation migration. The inversion follows the basic structure of the FWI workflow, but two important changes include the PSPI update direction and the log calibration. Jumps from depth to

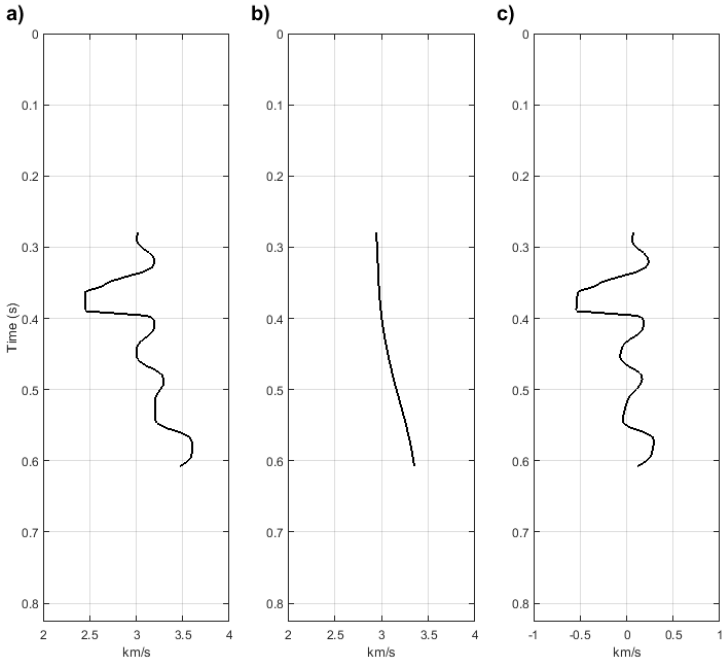

Figure 4.3: (a) $v^{(w)}$ = velocity log. (b) $v_k^{(w)}$ = velocity model in the well location. (c) $\delta v_k^{(w)}$ = velocity residual in well location. The subindex k denotes iteration number.

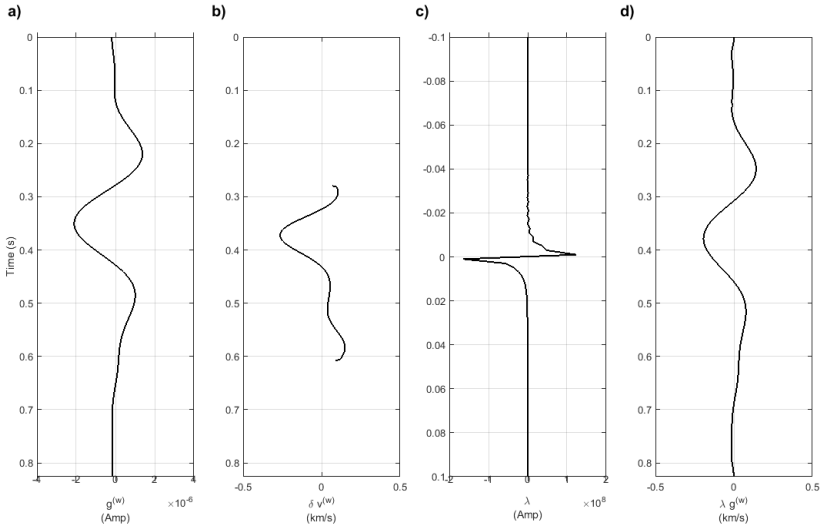

Figure 4.4: Log calibration in time domain for iteration $k = 1$. (a) Update direction in the well location ($\Phi_k^{(w)}$). (b) Velocity residual ($\delta v_k^{(w)}$) in the well location with a 1-6Hz band-pass frequency filtering. (c) Matched filter λ that makes (a) similar to (b). (d) Velocity perturbation in the well location produced by convolving (a) and (c).

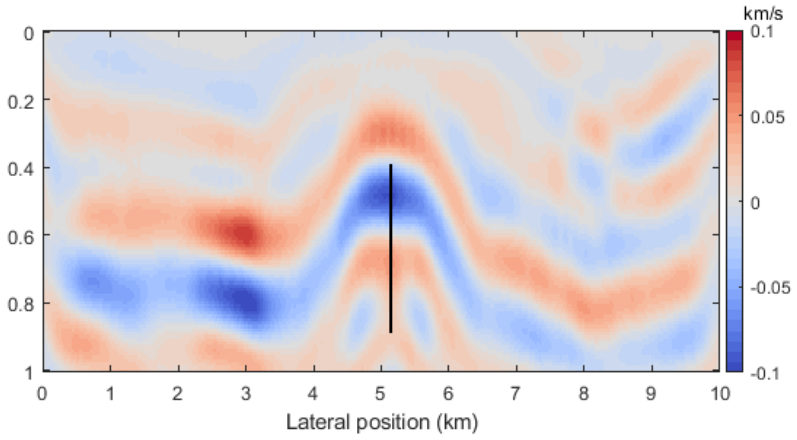

Figure 4.5: Velocity perturbation produced with well-log validation for the first iteration.

time and vice versa are done via the current velocity model (m_k). I implemented a multiscale approach, similar to what was applied in the previous numerical examples. The frequency band, naturally accommodated in PSPI migration, was started as 1-6Hz for iteration 1, and moved up by 1Hz in the following iterations (Table 2.1).

The RTM update direction can also be scaled by using well-log information as it is shown in the workflow in Figure 4.7. Since the RTM update direction is converted into a velocity perturbation when multiplied by a simple step-length, we only need to compute the scalar a that makes Φ_k similar to $\delta v_k^{(w)}$. In that sense, the quantity

$$\int [\delta v_k^{(w)} - a\Phi_k]^2 dz \tag{4.3}$$

is minimized. The scalar a is obtained as

$$a = \frac{\Phi_k^T \delta v_k^{(w)}}{\Phi_k^T \Phi_k}. \tag{4.4}$$

It is important to apply a band-pass filter to $\delta v_k^{(w)}$ in order to be comparable to Φ_k and compute meaningful values of a.

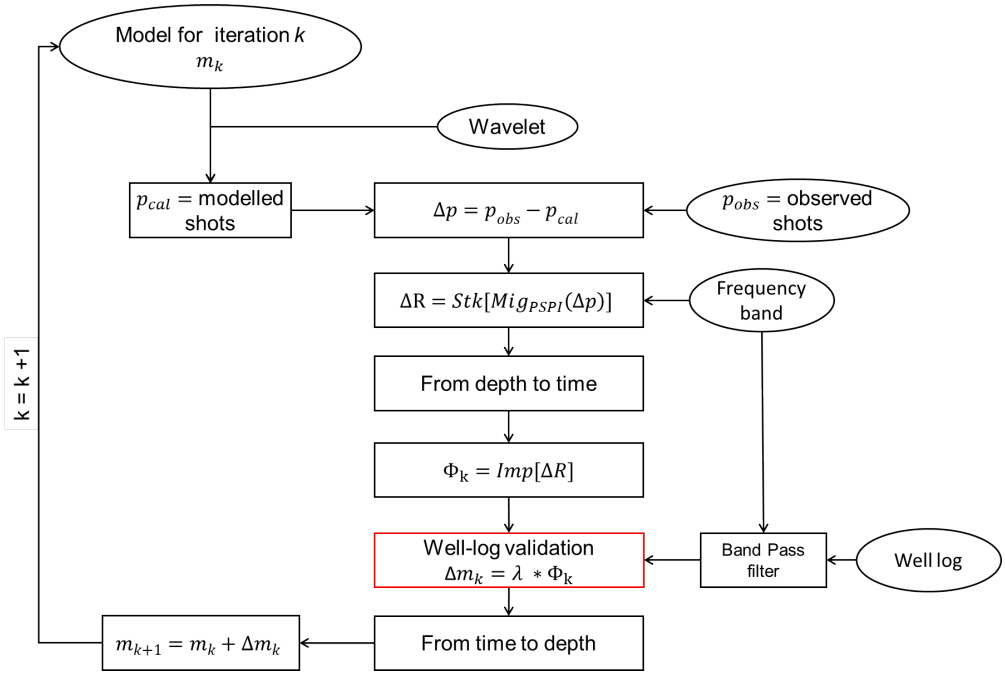

Figure 4.6: Workflow for log-validated waveform inversion with one-way equation migration.

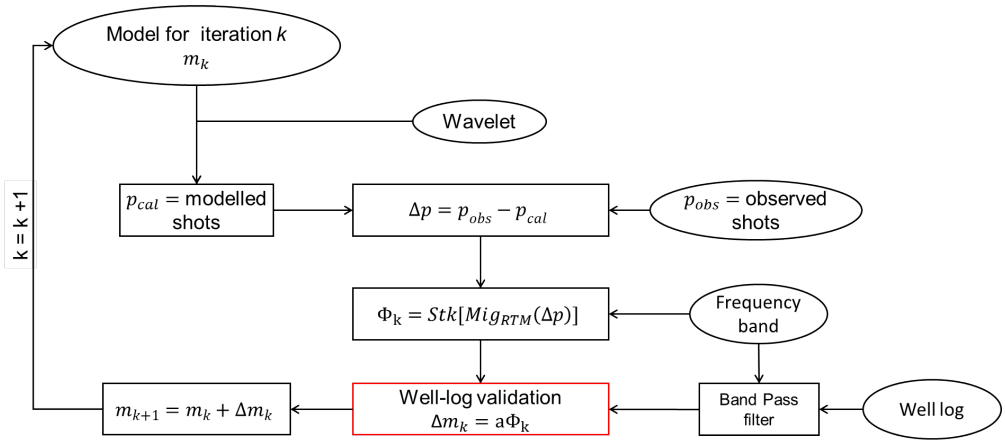

Figure 4.7: Workflow for log-validated waveform inversion with RTM update directions.

4.4 Numerical test

Figure 4.8 plots the inverted model after 20 iterations that results from applying four waveform inversion approaches: (a) RTM updated direction with data validation (standard FWI workflow in Figure 2.2), (b) RTM update direction with well-log validation (workflow in Figure 4.7), (c) PSPI update direction with data validation (workflow in Figure 3.12), and

(d) PSPI update direction with well-log validation (workflow in Figure 4.6). The inverted velocities in the calibration well and the data residuals, for the four cases, are plotted in Figure 4.9 and Figure 4.10, respectively. The model error (equation 2.59), the velocity error in the calibration well, and the data residual norms (equation 2.60) with iteration are plotted in Figure 4.11. The error in the well is measured as

$$Error^w = \sum |v^w_{true} - v^w_{inverted}|, \tag{4.5}$$

where v^w_{true} and $v^w_{inverted}$ are the true and inverted velocities in the well location.

The four waveform inversion methods produce similar inverted models. They are able to recover the main features of the subsurface including the small stratigraphic bodies in the right-and-left hand sides and at the middle of the section. The model error reports that RTM with data and well-log validation produce the smallest error, being both similar results. PSPI with data validation has the poorest performance, while PSPI with well-log validation has a remarkable improvement and the error moves closer to the RTM results. The comparison of the inverted velocity in the well location for PSPI with data validation (Figure 4.9c) and PSPI with well-log validation (Figure 4.9d), shows that the remnant update-direction phase problem of the former has been diminished in the latter. A close look at the inverted velocities in the well and the data residuals reveals important differences between the RTM and PSPI outcomes. The former can better retrieve the shallow velocities, which in turn allows predicting the direct and refracted waves more properly. This is reflected in highly attenuated first arrivals in the data residuals. On the other hand, the PSPI data residuals exhibit a strong signature of the first arrivals, which affects the reduction of the data residual norms and may have an impact in the implementation of data validation procedures. A close look to the data residuals for the PSPI update direction with and without well-log validation (Figures 4.10c-d), shows that the reflections are significantly diminished when log calibration is employed; however, the first arrivals persist and dominate in both cases, which results in

similar data residual norms (Figure 4.11c). The reason of this is that PSPI uses mainly the primary reflections to reconstruct the velocity model. PSPI cannot handle the diving waves as RTM does to recover the low-frequency components of the model, and without this information the first arrival are not properly modelled. The implications of this is examined in Chapter 7, where the sensibility of the waveform inversion to the initial model is analyzed. We also observe in Figure 4.11b that the error in the well location does not always decrease as we iterate. This happens because the well-log validation technique does not explicitly minimize the error between the velocity in the well and the velocity in the model, what this technique does is to minimize the difference between the velocity residual in the well location and the update direction.

It is relevant to consider the computational burden in the comparison of the waveform inversion workflows (Table 4.1), because this factor may determine their application on a large volume of data. Figure 4.12 plots the time that takes the main step in the inversion workflow (forward modelling, update direction construction which involves migration, and scaling) for different combinations of migration methods (RTM or PSPI) and data or well-log validation. The times were measured considering the processing of one single shot. The times are normalized taking as a reference the most expensive workflow which is (a) the standard FWI that involves RTM migration and backtracking data validation. Workflow (b) is similar than (a) but with Tarantola-and-Pica's data validation. Workflow (c) is similar than (a) but with well-log validation. Workflow (d) corresponds to PSPI migration with backtracking data validation. Workflow (e) is similar than (d) but with Tarantola-and-Pica data validation. The cheapest workflow is (f), which involves PSPI migration and well-log validation. Weighing up computational time and inversion results, PSPI may be considered for real large volume data applications.

Table 4.1: Inversion workflows with a different combination of update-direction types and scaling methods

Option	Update direction	Scaling method
a	RTM	Backtracking
b	RTM	Tarantola-and-Pica
c	RTM	Well-log calibration
d	PSPI	Backtracking
e	PSPI	Tarantola-and-Pica
f	PSPI	Well-log calibration

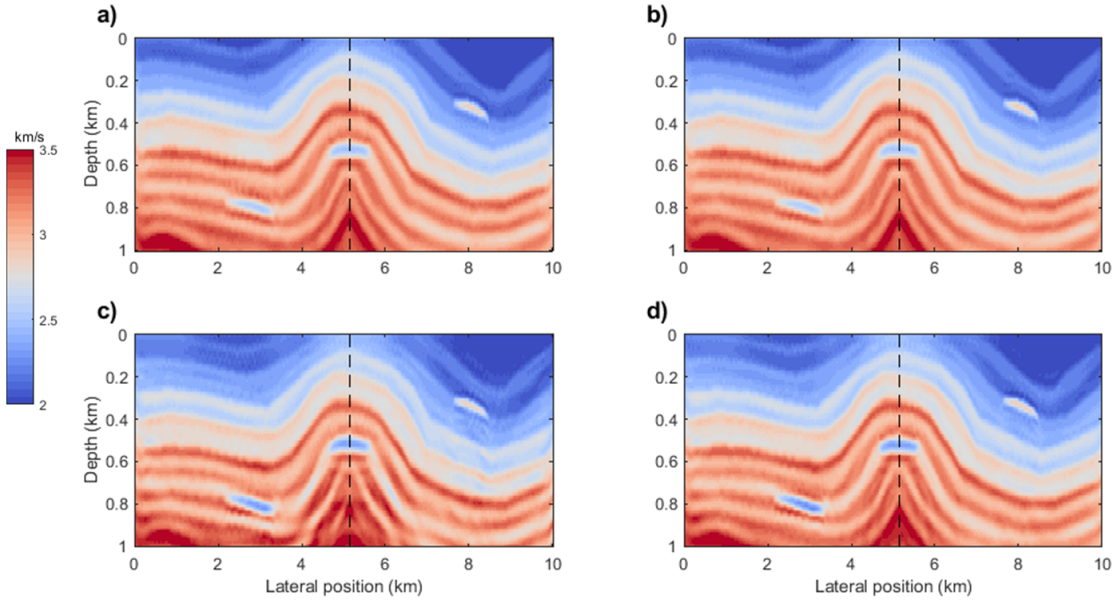

Figure 4.8: Inverted model after 20 iterations for (a) RTM update direction with data validation, (b) RTM update direction with well-log validation, (c) PSPI update directions with data validation, and (d) PSPI update directions with well-log validation.

4.5 Combining well-log and data validation

I have implemented two methods to scale or calibrate the update direction in waveform inversion. The computation of the step-length while explicitly minimizing the data residual is called data validation method. When well-log information is employed to convert the update direction into a velocity perturbation, the method classifies as well-log validation. The workflow, shown in Figure 4.13, poses a combination of these two methods, where the update direction is firstly calibrated with well-log information and then data validation is

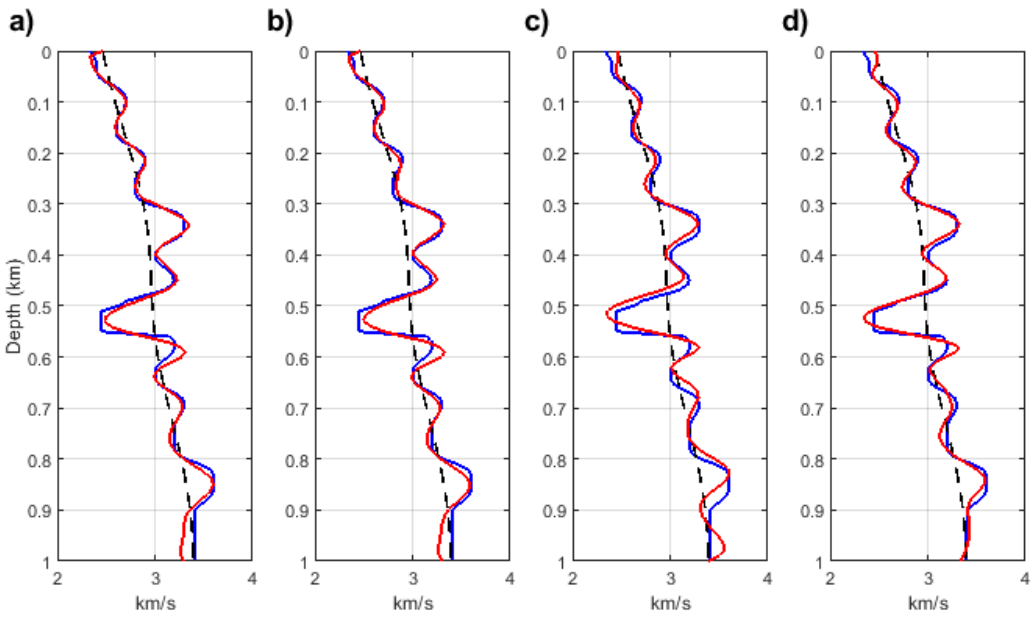

Figure 4.9: Inverted velocity in the calibration well after 20 iterations for (a) RTM update direction with data validation, (b) RTM update direction with well-log validation, (c) PSPI update directions with data validation, and (d) PSPI update directions with well-log validation.

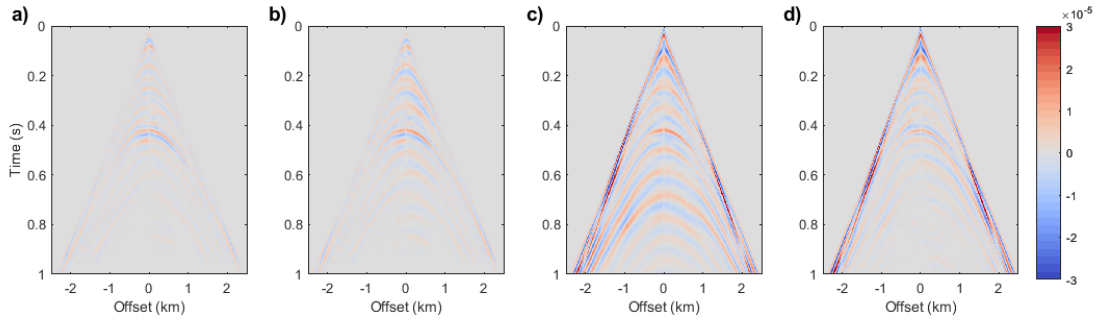

Figure 4.10: Data residual after 20 iterations for (a) RTM update directions with data validation, (b) RTM update directions with well-log validation, (c) PSPI update directions with data validation, and (d) PSPI update directions with well-log validation.

applied. The comparison of the inverted model derived by (a) data validation, (b) well-log validation and (c) the combination of the methods, is plotted in Figure 4.14. The model error and the data residual norms with iterations for the three scenarios are plotted in Figure 4.15. I conclude that for a simple model, well-log validation, and the combination of well-log and data validation, produce a similar outcome, being the data residual norms of the latter

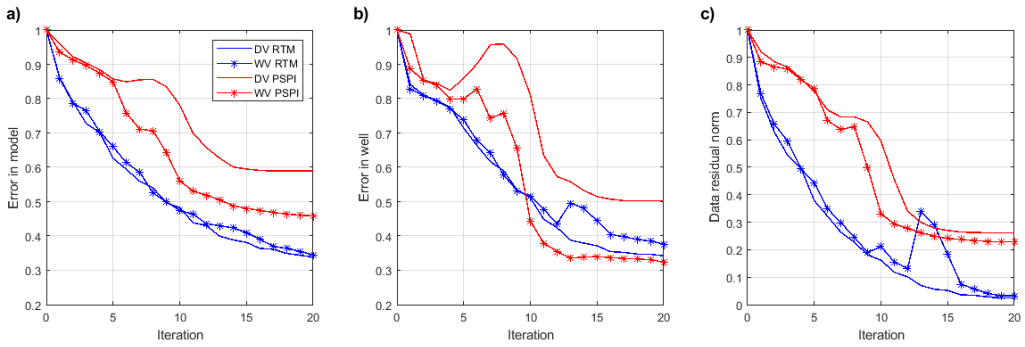

Figure 4.11: (a) Model error, (b) error in the calibration well location, and (c) data residual norms for RTM and PSPI update directions with data validation (DV) and well-log validation (WV).

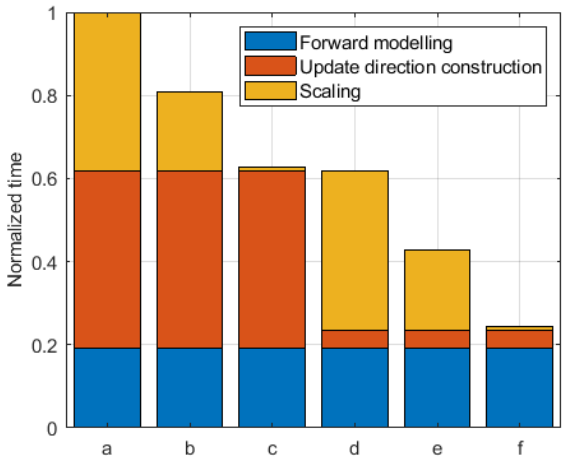

Figure 4.12: Computational burden for the main steps in the waveform inversion. One shot was considered in the process and the total time is normalized. (a) RTM update direction and backtracking data validation. (b) RTM update direction and Tarantola-and-Pica's data validation. (c) RTM update direction and well-log validation. (d) PSPI update direction and backtracking data validation. (e) PSPI update direction and Tarantola-and-Pica's data validation. (f) PSPI update direction and well-log validation.

method slightly smaller. I would recommend the use of well-log validation in the case of moderate complex models because of the low computational cost.

I compared the three scaling techniques with the more complex Marmousi model (Figure 4.16a). The "observed" shot records are generated with a minimum phase wavelet under a dominant frequency of 10Hz. The source and receiver intervals are 500 and 10 meters,

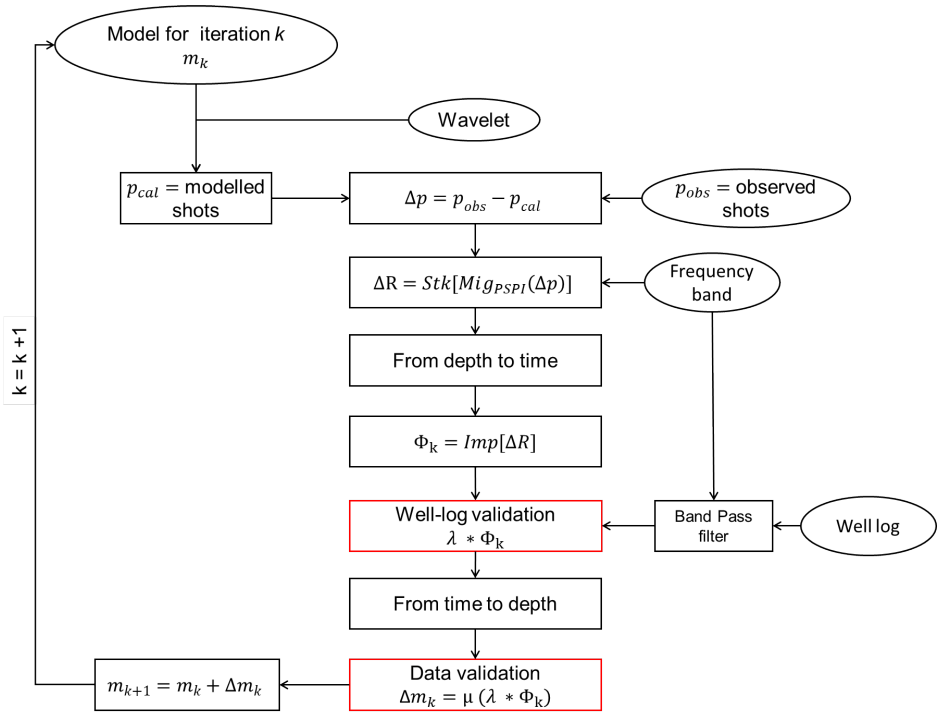

Figure 4.13: Workflow of waveform inversion with a combination of well-log validation and data validation.

respectively. The total number of shots is 20. The initial model for the inversion is generated by applying a Gaussian smoother with a half-width of 200m to the true model (Figure 4.16b). The frequency band goes from 1 to 5Hz for the first iteration, then it is moved up by 1Hz in each iteration. The calibration well is located at the middle of the model cutting an anticline at a depth of 2500 m. The top and base of this well are 400 and 2700 m, respectively. Five shots, distributed along the surface, were used for the data validation. The comparison of the inverted model produced by (a) data validation, (b) well-log validation and (c) the combination of the methods is plotted in Figure 4.17. The model error and the data residual norms with iterations for the three scenarios are plotted in Figure 4.18. A blurry character dominates the data validation version, and the velocities tend to be underestimated from the shallow to the central zone. The phase correction provided by well-log validation generates an improved model with a better fault definition; however, there are some flaws at the deeper part of the model (pointed out by arrows), such as an extra layer at the right-hand side of

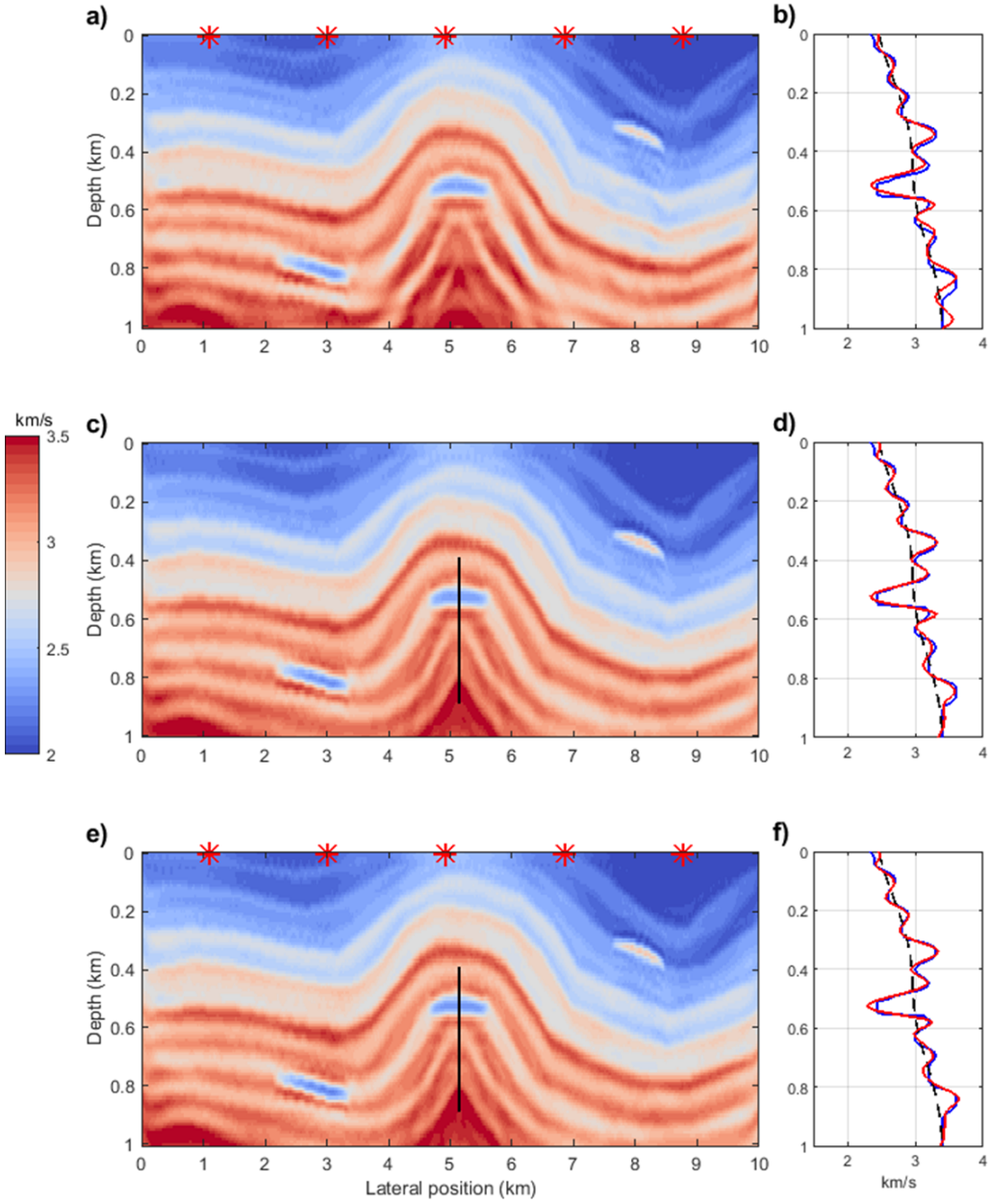

Figure 4.14: Inversion result for the anticline model and inverted velocity at the calibration well location after 20 iterations for (a-b) data validation, (c-d) log validation and (e-f) log-and- data validation. The red stars represent the shots used in the data validation process. The black line represents the well-log information used for the well-log validation.

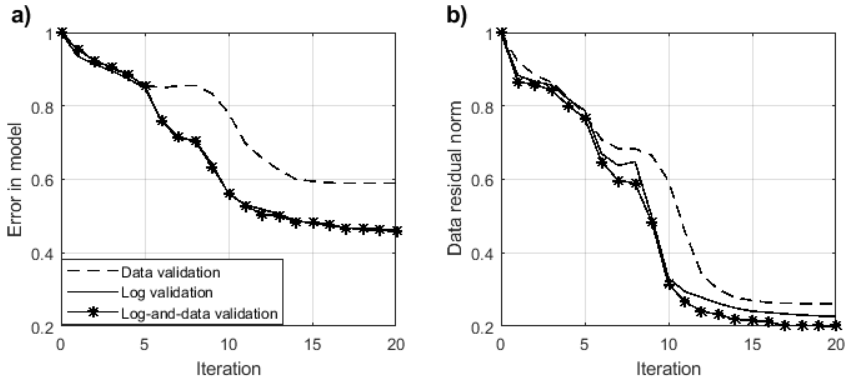

Figure 4.15: (a) Error through the anticline model and (b) data residual norms for data, log, and log-and-data validation.

the model and the overextension of the low-velocity body close to the well. The combination of well-log validation and data validation produces the overall best result as it is confirmed by the model error and the data residual norms. This technique provides a good definition of the faulty zone and corrects some of the defects in the deeper part of the model. I would recommend using the combined method for complex models.

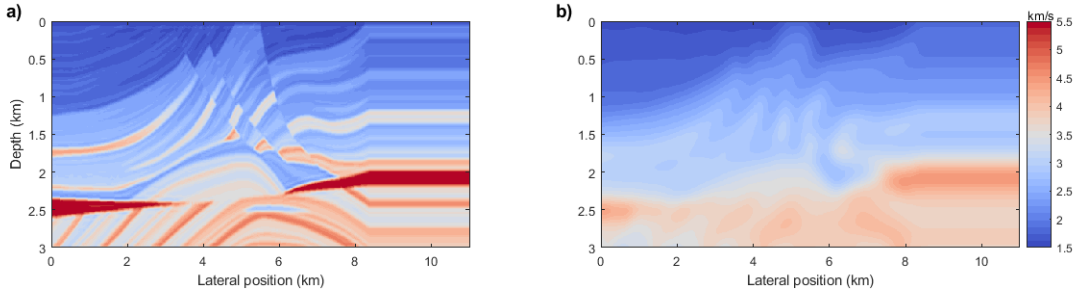

Figure 4.16: (a) Marmousi model. (b) Initial model.

4.6 Conclusions

Based on the FWI workflow, an alternative perspective of waveform inversion has been set up. The new workflow replaces the conventional RTM by PSPI update directions. The latter has a different phase compared to the former. This phase shift is partially corrected

by implementing impedance inversion. However, there is a remnant phase that may prevent the convergence of the method. This issue is overcome by introducing well-log validation. The technique consists in computing a matched filter that minimizes the difference between the update direction and the velocity residual at the well location. A simplified version of well-log validation was also proposed to be used with the RTM update directions. In all the numerical tests, well-log validation tends to reduce the data residual norms, which is relevant because they are not explicitly minimized in this method. The cost-benefit analysis of FWI and well-log validated waveform inversion puts the latter in a favorable place because it can deliver similar results (considering simple geological settings such as the anticline model) with a lower computational burden. Finally, a workflow that combines well-log and data validation was proposed. Tests in simple geological settings do not report any advantage with the combined technique; however, the implementation in the complex Marmousi model resulted in a better convergence to the model.

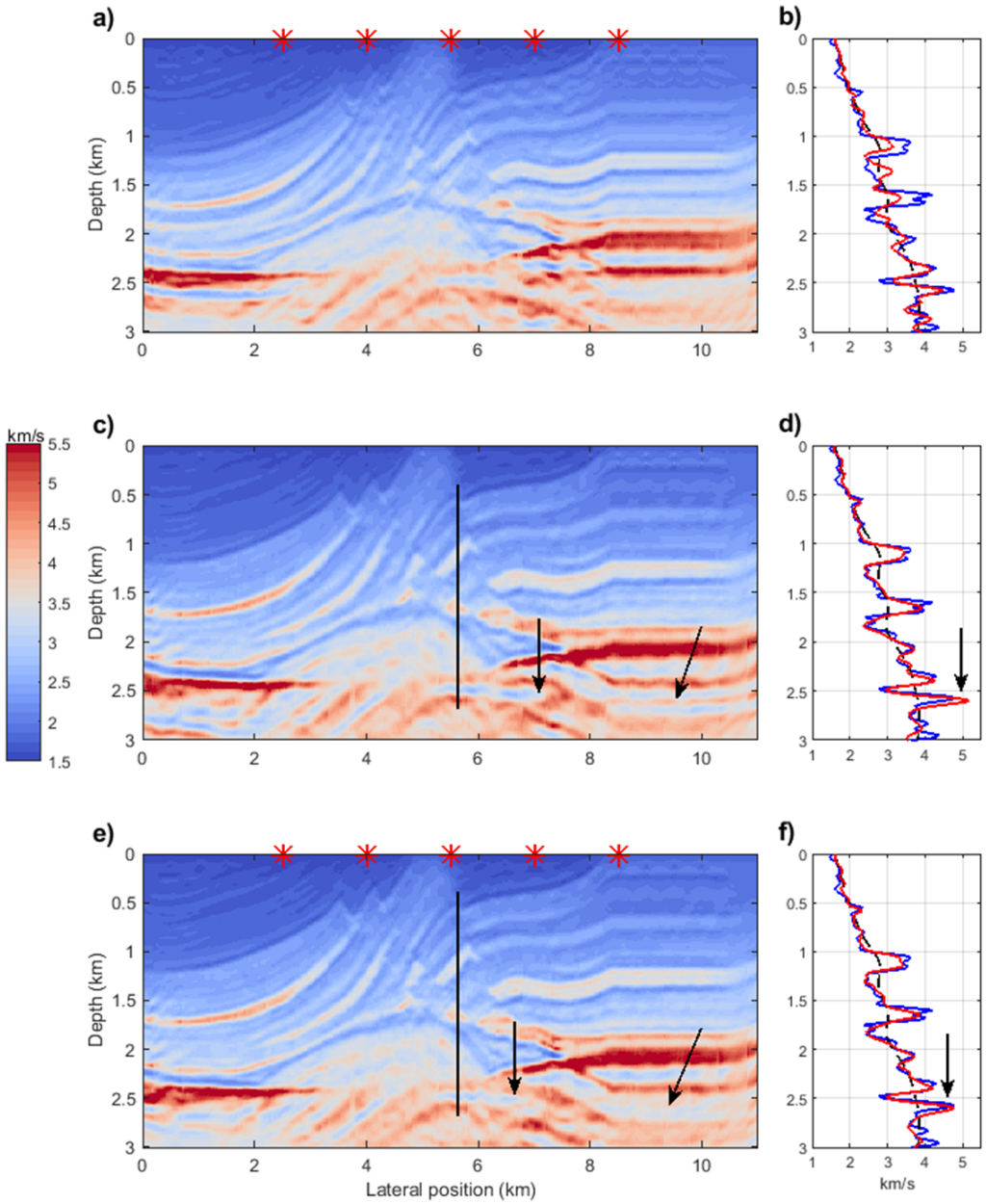

Figure 4.17: Inversion result for the Marmousi model and inverted velocity at the calibration well location after 20 iterations for (a-b) data validation, (c-d) log validation and (e-f) log-and- data validation. The red stars represent the shots used in the data validation process. The black line represents the well-log information used for the well-log validation. The arrows point out improvements in (e) with respect to (c).

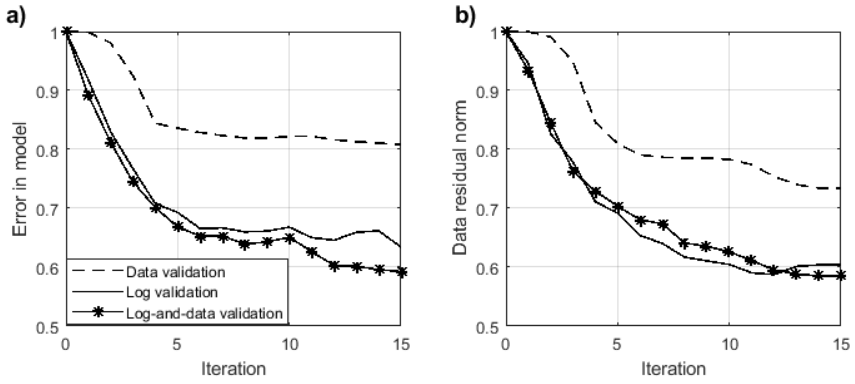

Figure 4.18: (a) Error through the Marmousi model and (b) data residual norms for data, log, and log-and-data validation.

Chapter 5

Sensitivity of well-log validated waveform inversion to well location and aperture, geological complexity, and data uncertainty

5.1 Introduction

I showed in Chapter 2 the suitability of FWI to recover the distribution of Earth properties in the subsurface by iteratively reducing data residuals, i.e., the differences between observed and synthetic seismic shot records. The model update was produced from a calculation of the reverse-time migration (RTM) of the data residual multiplied by a simple scalar. The application of this method faces some key remaining technical challenges, including the computational cost of applying it to large datasets, and convergence issues originating with the incomplete nature of seismic data (Jackson, 1972). Margrave et al. (2012a) introduced an inversion formulation referred to as iterated modeling, migration and inversion (IMMI), whose main internal features were the use of one-way migration operators (PSPI migration)

to obtain the gradient and well-log model validation to scale it. The former and the latter implementations were discussed in Chapters 3 and 4, respectively. Intuitively, in a medium with limited horizontal variation in its properties, the information provided by a well-log at one location would be expected to carry over to other regions of the medium well. It is less clear how accurately well-log data stabilizes waveform inversion in media with moderate to large lateral variability. Also, well-log data are finite, with shallow and deep truncation points that may differ significantly from case to case. Well-log aperture must influence the effectiveness of the model-validation, but at present, this has not been quantified. The purpose of this Chapter is to summarize a study in which these questions are answered through systematic synthetic testing.

5.2 Testing of log-validated waveform inversion

The numerical examples in this section were designed to permit relatively broad conclusions to be made concerning the limits and possibilities of the log-validated inversion. All follow the procedure described in the workflow shown in Figure 4.6.

5.2.1 Geological complexity

An important source of subsurface information is provided by well-logs. However, this information is limited to the well location and may not be valid as we go away from the well; this is true especially in complex geological settings. In this section, I examine the accuracy of models generated with log-validated waveform inversion as the degree of geological complexity changes. Three velocity models are used for this purpose. The first model is the simplest one (Figure 5.1a). It is a modification of the Marmousi model, where the shallow faults have been replaced by horizontal layers. The second model includes moderate lateral velocity variations in the shallow zone (Figure 5.1b). In this case, the shallow faults of the Marmousi model are replaced by folded layers. The original Marmousi model is employed in

the third case (Figure 5.1c) to represent the greatest geological complexity in our tests. The well, used for generating the velocity perturbation, is located in the middle of each model; it is assumed to provide information from 400 to 2700m. In order for the variations in the detailed information coming from the logs not be a factor in the comparison, the models were set up such that the velocity log is unchanged for the three models (Figure 5.3). In Figure 5.1d-f the initial velocity models, generated by applying a Gaussian smoother with a half-window of 200m to the true models, are plotted. Inverted models after 15 iterations are plotted in Figure 5.1g-i. We are able to obtain interpretable models in all three scenarios, and the main geological features appear to be successfully recovered. However, the errors in the inverted models, plotted in Figure 5.2, show that a clear decrease in accuracy occurs as the geological complexity increases. The inverted velocity in the well location, for the three scenarios, is plotted in 5.3a-c. For the simplest model, we are able to resolve thinner details of the velocity; however, as the complexity increases, the inverted velocity tends to be smoother. This has an impact on the error in the well location, which tends to grow with higher complexity (Figure 5.4). The observed and modelled shot records, and the data residuals after 15 iterations are shown in Figure 5.5. The norms of the data residuals are plotted in Figure 5.6. For models 1 and 2, these norms are very similar and decrease with iteration. For the most complex model 3, the norms are larger per iteration and do not decrease beyond iteration 12. I conclude that there exist ranges of lateral variation and geological complexity within which log-validated waveform inversion experiences little extra error; however, when the medium involves discontinuous lateral changes (e.g., significant faulting) errors accrue, a problem that should be taken into account in interpretation.

5.2.2 Well location

Intuitively, the precise positioning of a well-log might be expected to cause variations in inversion accuracy in media with moderate to large lateral variability. To examine this, I used the Marmousi and the initial velocity models plotted in Figures 5.1c and 5.1f to

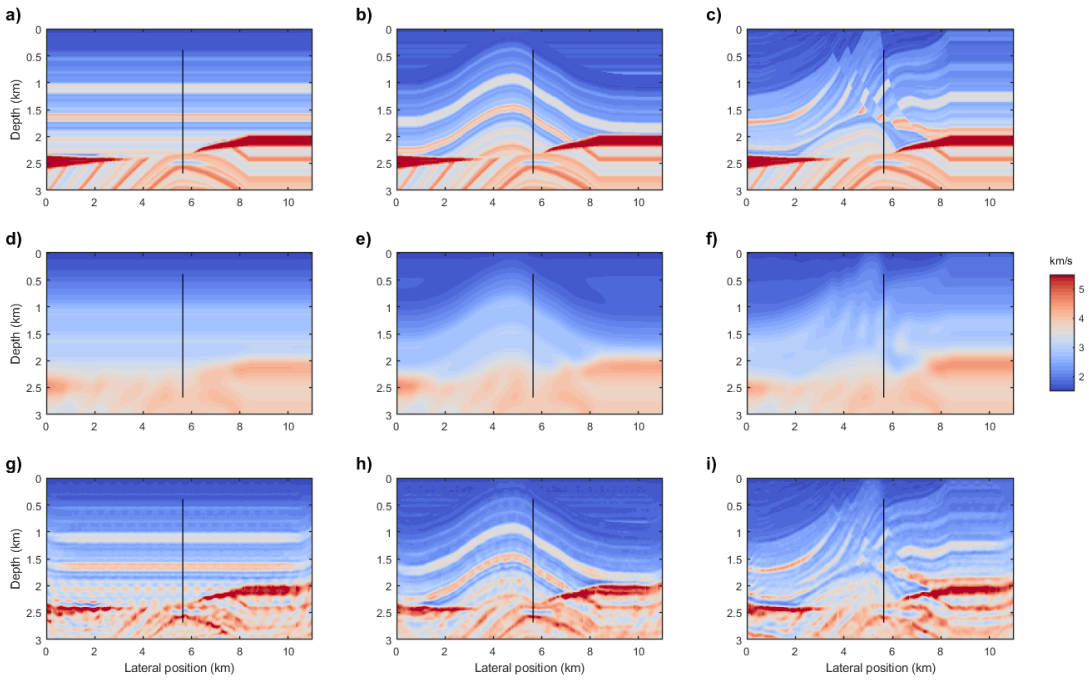

Figure 5.1: Inversion results with three different models from simple to complex geology. (a) Model 1: modified Marmousi model with horizontal layers in the shallow zone. (b) Model 2: modified Marmousi model with folded layers in the shallow zone. (c) Model 3: original Marmousi model. (d-f) Initial velocity for models 1, 2 and 3. (g-i) Inversion result for models 1, 2 and 3.

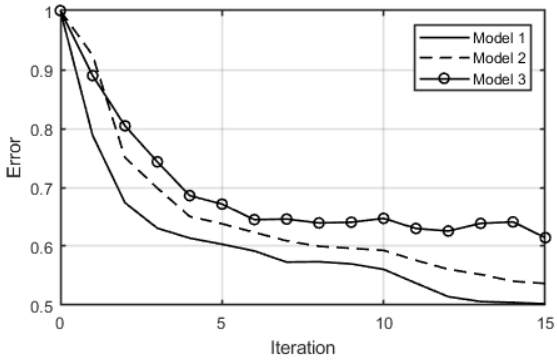

Figure 5.2: Error in the inverted models in Figures 5.1g-i.

estimate the matched filters that would calibrate the update direction by if velocity logs were available at every single lateral position of the model (Figure 5.7). The wells have the

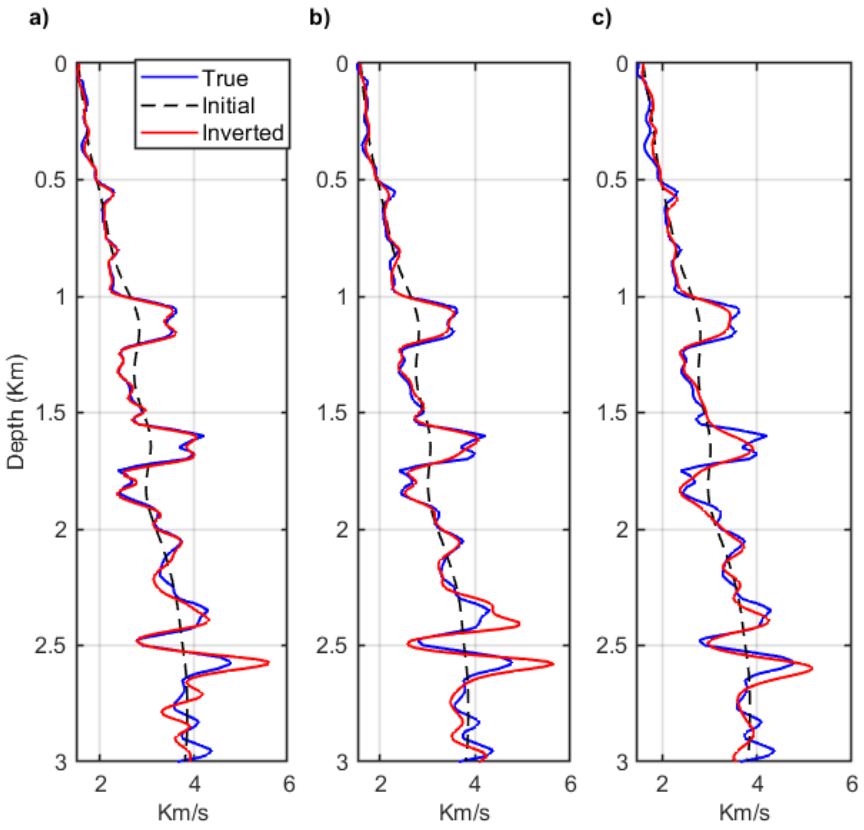

Figure 5.3: Inversion results in the calibration well location for (a) model 1, (b) model 2, and (c) model 3.

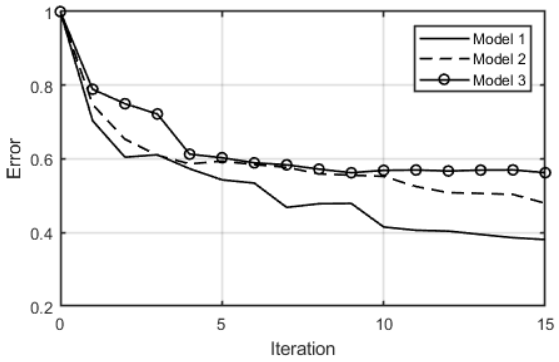

Figure 5.4: Velocity error in the well location for model 1, 2 and 3.

same depth interval (400-2700m), and I considered a 1-5Hz frequency band matching that of the first iteration. In Figures 5.7b-d the matched filters for wells C1, C2, and C3, at lateral positions 3.6km, 5.65km and 8.2km, respectively, are plotted. We observe significant

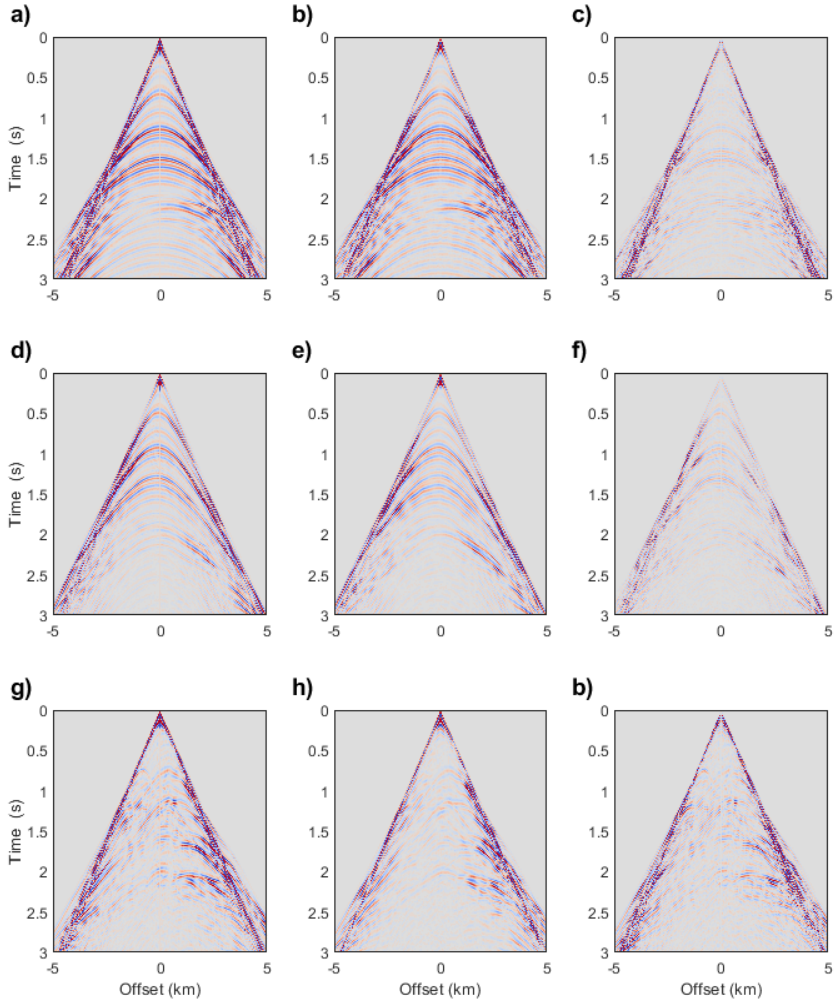

Figure 5.5: Observed and modelled shot records, and data residual after 15 iterations for (a-c) model 1, (d-f) model 2, and (g-i) model 3

differences in the filters at each well location. In order to evaluate how the location of the well affects the inversion result, I performed three inversions, using one of C1, C2, and C3 as calibration wells each time. I also investigated the possibility of using all three wells to generate a matched filter λ as a function of the lateral position x:

$$\lambda(x) = W_{C1}(x)\lambda_{C1} + W_{C2}(x)\lambda_{C2} + W_{C3}(x)\lambda_{C3}, \tag{5.1}$$

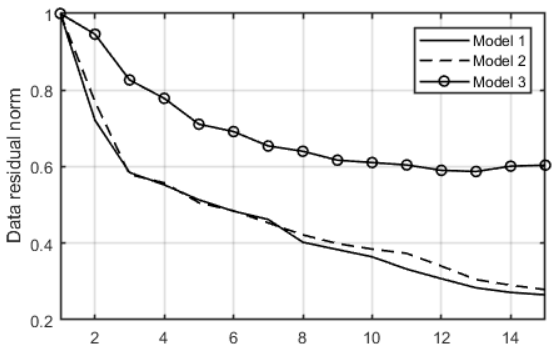

Figure 5.6: Data residual norms after 15 iterations for models 1, 2 and 3.

where λ_{C1}, λ_{C2} and λ_{C3} are the matched filters for wells C1, C2 and C3, respectively. $W_{C1}(x)$, $W_{C2}(x)$ and $W_{C3}(x)$ are weighting functions (Figure 5.8) determining the influence of each matched filter for a specific position x. The weighting functions are obtained as:

$$\begin{aligned} W_{c1}(x) &= \frac{\max(x) - |x - x_{c1}|}{3\max(x) - |x - x_{c1}| - |x - x_{c2}| - |x - x_{c3}|}, \\ W_{c2}(x) &= \frac{\max(x) - |x - x_{c2}|}{3\max(x) - |x - x_{c1}| - |x - x_{c2}| - |x - x_{c3}|}, \\ W_{c3}(x) &= \frac{\max(x) - |x - x_{c3}|}{3\max(x) - |x - x_{c1}| - |x - x_{c2}| - |x - x_{c3}|}, \end{aligned} \tag{5.2}$$

subject to:

$$W_{C1}(x) + W_{C2}(x) + W_{C3}(x) = 1. \tag{5.3}$$

where x_{c1}, x_{c2} and x_{c3} are the well locations.

The inverted models are plotted in Figures 5.9a-d. The results counter-intuitively suggest that the procedure has little sensitivity to the well location, even though the matched filter may change from one position to another. In Figure 5.10a the error in the inverted models is plotted. The smallest and greatest errors are associated with C3 and C2, respectively, and the simultaneous use of three wells produces an average result. C3 produces the best result, indicating that this well is, of the three, the most representative of the velocity across

the model. This latter statement can be confirmed by cross-correlating the reflectivity in each well with the reflectivity of the rest of the model, from which the greatest similarity is obtained for well C3 and the least for well C2. In Figure 5.10b the data residual norm is observed to be similar for all four scenarios, which is a further indication that the inversion is insignificantly affected by the well location.

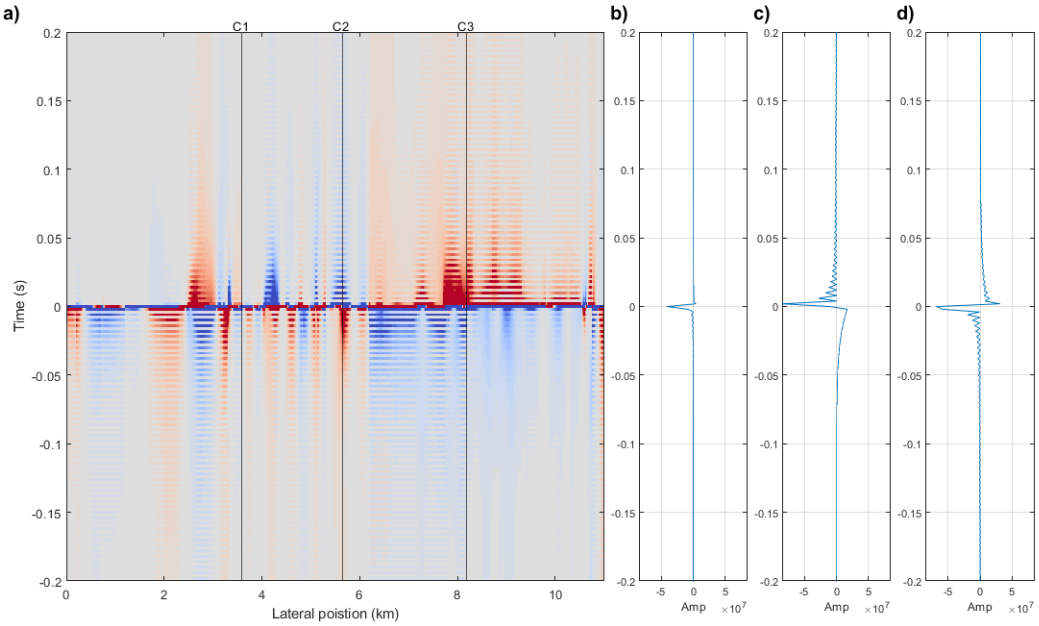

Figure 5.7: (a) Matched filters estimated by assuming the presence of a calibration well at every lateral position of the model. (b) Matched filter for well C1 at lateral position 3.6km. (c) Matched filter for well C2 at lateral position 5.65km. (d) Matched filter for well C3 at lateral position 8.2km.

5.2.3 Log interval

Well-logs differ significantly from reservoir to reservoir in their vertical extent. To analyze the influence of the log interval on the accuracy of inversions, I set up a well in the middle of the Marmousi model, and extracted log information from four intervals: 1) 400-2700m, 2) 1300-2700m, 3) 1700-2700m and 4) 2100-2700m (Figure 5.11a). To measure the size of these intervals in a meaningful way, I take the average wavelength in the first iteration as a

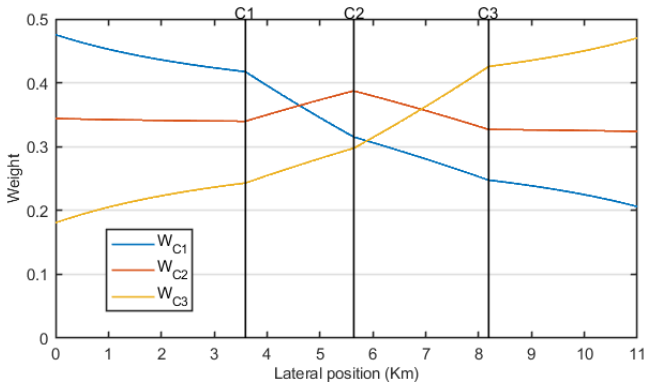

Figure 5.8: Details from the use of aggregate information from three wells to obtain the matched filter. The contribution of each well to the matched filter at every lateral position is defined by the weighted functions $W_{C1}(x)$, $W_{C2}(x)$ and $W_{C3}(x)$.

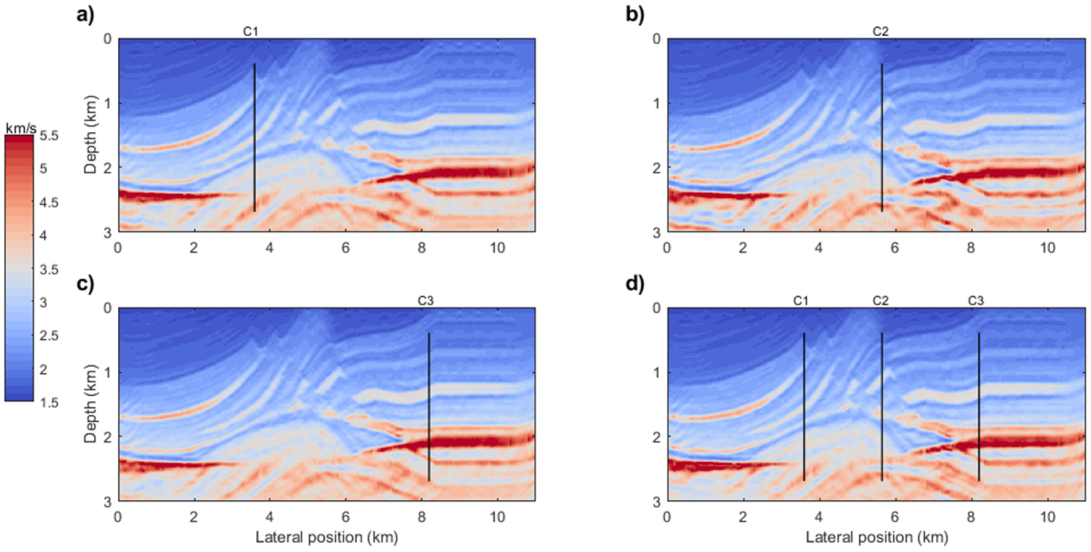

Figure 5.9: Inverted model after 15 iterations for (a) calibration well C1, (b) calibration well C2, (c) calibration well C3, and (d) the combined used of all of them.

reference length-scale. The average velocity in the well is 2900 m/s, and the center frequency in the 1-5Hz band is 3Hz; therefore, the average wavelength is 957m. For cases 1 and 2, the log intervals are equal to or larger than 1.5 times the average wavelength. For case 3, the log interval is close to one average wavelength. For case 4, the log interval is close to half the average wavelength. In Figure 5.11b the segment of the update-direction vector at the well-location that is used for calibration in each case is plotted. In Figure 5.11c the

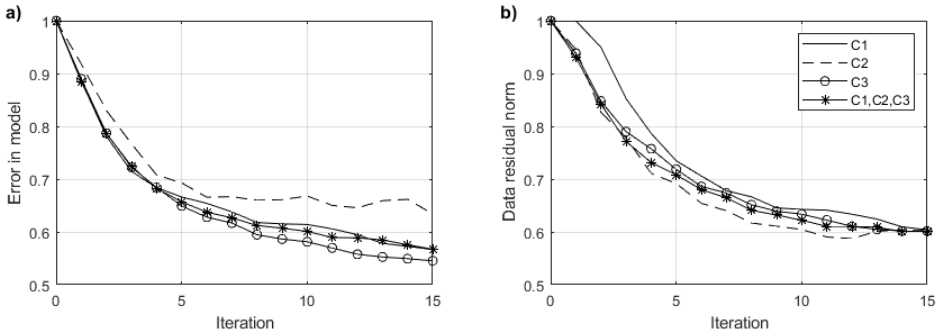

Figure 5.10: (a) Error in inverted models and (b) data residual norms for different calibration well locations and the combined used of all of them.

matched filters produced in each case are plotted. The velocity perturbations, obtained by convolving the matched filters and the update direction at the well location, are plotted in Figure 5.11d. When the log interval is small (half the average wavelength), such as in case 4, the amplitude scalar and phase rotation angle are inaccurately estimated, which negatively affects the computed velocity perturbation. Inversion results for all four scenarios are plotted in Figure 5.12. The errors associated with the inverted models and the data residual norms are plotted in Figure 5.13a and 5.13b, respectively. Cases 1 and 2 produce essentially the same result, and the errors in the model and the data residual norms tend to decrease as we iterate. In case 3, the errors and data residual norms are unstable after iteration 7 and the inverted model has a ringing character. In case 4, the result has a blurry character with an over- or under-estimation of the velocity across the model. In this fourth case, the process is entirely unstable, leading to the highest errors in the model and the data residuals. These results suggest that the log calibration may need a log interval equal to or greater than 1.5 times the average wavelength determined for the first iteration when the smallest frequency band is employed to start the inversion.

5.2.4 Log noise

Other sources of inaccuracies with sonic logs may be caused by mud invasion, cycle skipping, hole conditions, instrument problems or noisy recording conditions (Lines and Daley, 2009).

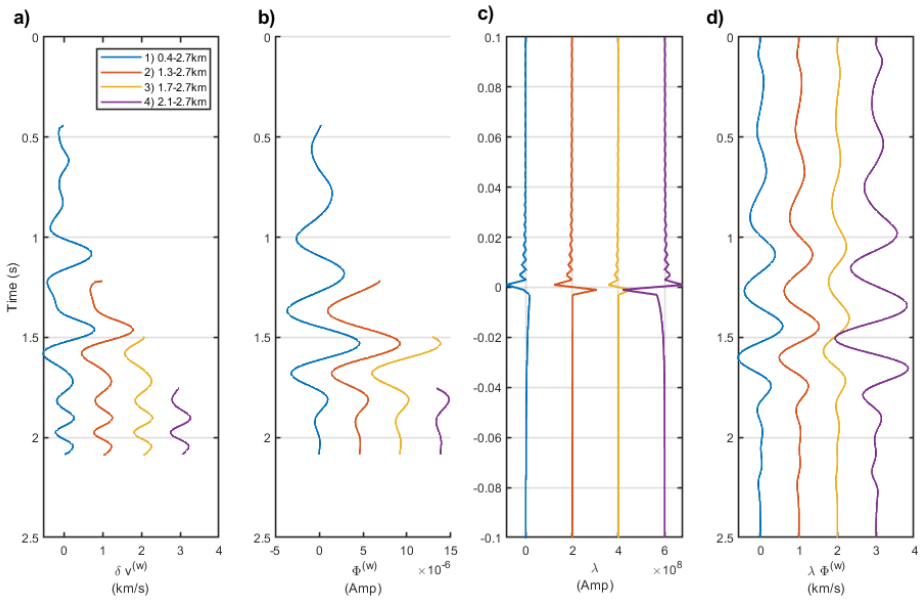

Figure 5.11: Calibration of update direction for different log intervals: 1) 400-2700m, 2) 1300-2700m, 3) 1700-2700m, and 4) 2100-2700m. (a) Velocity residuals. (b) Update direction interval used for the calibration. (c) Matched filters λ. (d) Velocity perturbations at the well location.

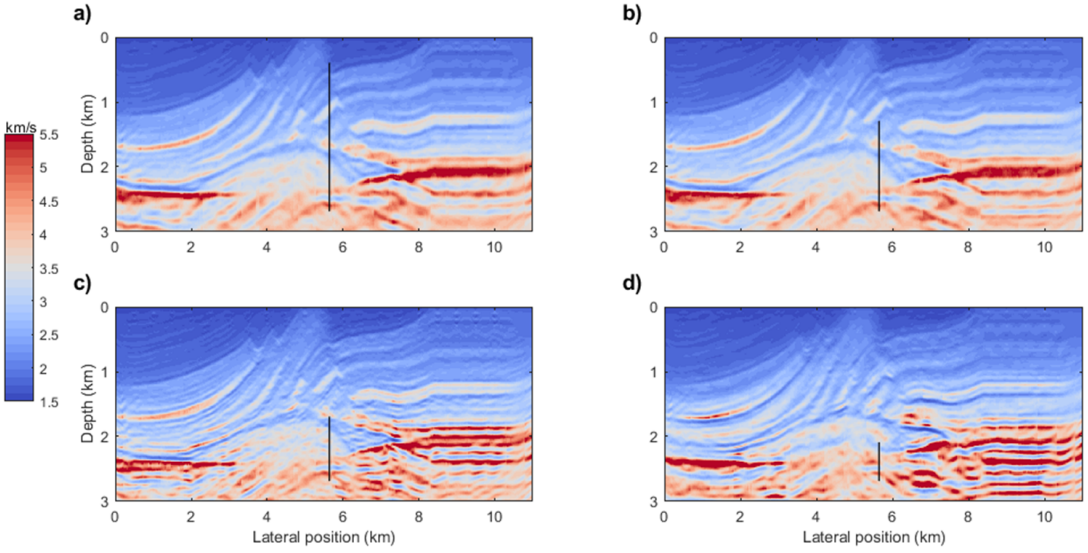

Figure 5.12: Impact of the log interval in the inversion result. Inverted model after 15 iterations for log interval: (a) 400-2700m, (b) 1300-2700m, (c) 1700-2700m, and (d) 2100-2700m.

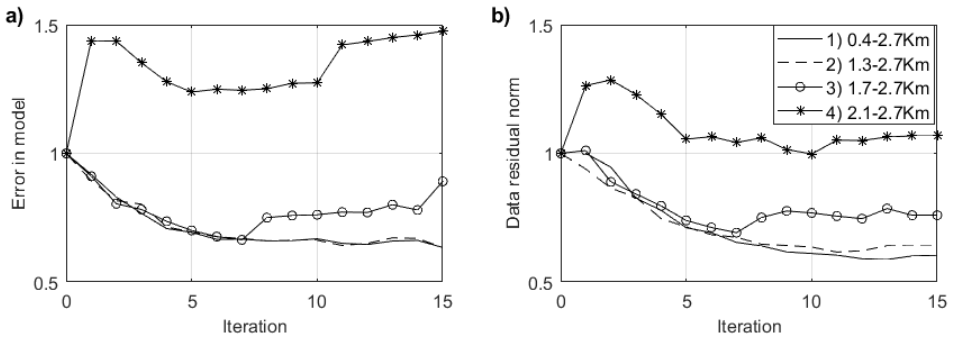

Figure 5.13: (a) Error in model and (b) data residual norm for different log intervals: 1) 400-2700m, 2) 1300-2700m, 3) 1700-2700m, and 4) 2100-2700m.

In this section, I evaluate the consequences for the inversion of uncertainty within the log data due to random noise. The root mean squared amplitude of the noise (RMS_{noise}) is set up by dividing the root mean squared amplitude in the velocity log (RMS_{log}) by the desired signal-to-noise ratio (SN)

$$RMS_{noise} = (RMS_{log})/SN. \tag{5.4}$$

When I refer to moderate and strong noise, I imply a $SN = 4$ and $SN = 2$, respectively. The Marmousi model and a well located in the middle of the model with a depth interval from 400 to 2700m are used in the following tests. The velocity log with moderate noise is plotted in Figure 5.14b, and the log with strong noise is plotted in Figure 5.14c.

In Figure 5.15 the inverted model in the case of no noise is compared to those determined using noisy logs. In Figure 5.16a the error in the inverted models is plotted, and in Figure 5.16b the velocity error at the well location is plotted. For the case of moderate noise, the log validation is still able to produce meaningful velocity perturbations resulting in an inverted model very similar to the case with no noise. The error in the model slightly increases after iteration 8 when we are including higher frequencies to the inversion. When the log is affected by a strong amount of noise, the inverted model has a ringing and blurry character (Figure 5.15e). The inversion becomes unstable after iteration 8 when error abruptly increases. In Figure 5.17 the data errors for the three scenarios are plotted. The data residuals tend to

be similar when the log has no noise and with moderate noise; however, the presence of strong noise strongly impacts the data residuals, which rapidly increase after iteration 8. I conclude that a moderate degree of uncertainty within the well-log can be accommodated by the waveform inversion, but strong random noise should be expected to limit the stabilizing effect of the model validation.

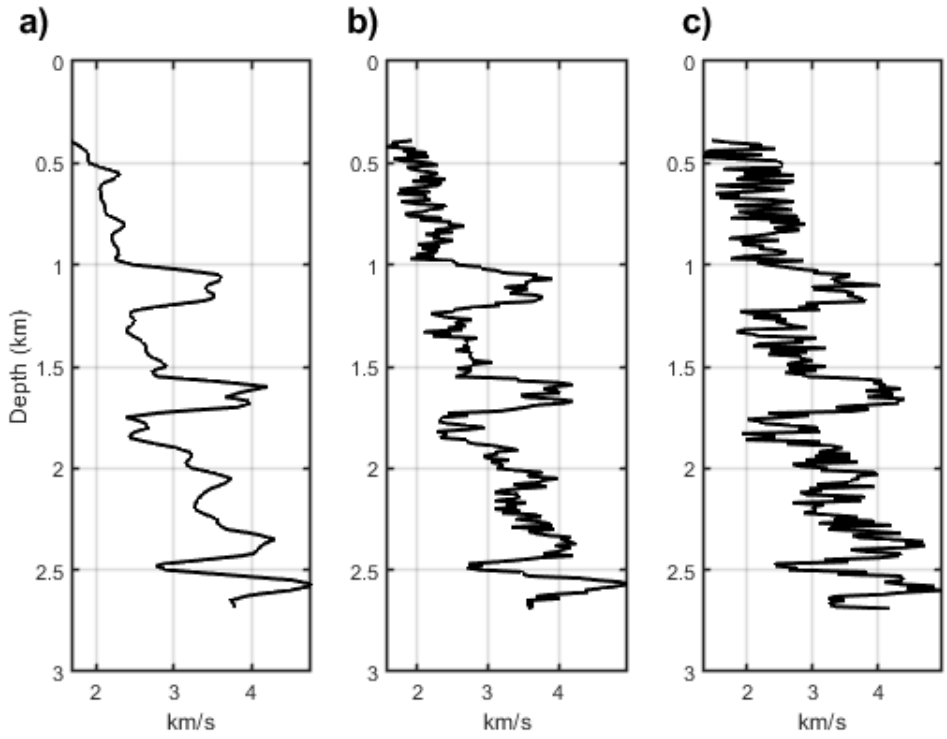

Figure 5.14: ((a) Velocity log with no noise. (b) Velocity log with moderate random noise. (c) Velocity log with strong random noise.

5.3 Conclusions

I have formulated a log-validated waveform inversion methodology which is substantially different from FWI in two main ways: 1) the update direction is obtained through one-way wave operators as a substitution for the RTM gradient, and 2) log validation is applied iteratively in order to generate the velocity perturbation, as a substitution for line search or

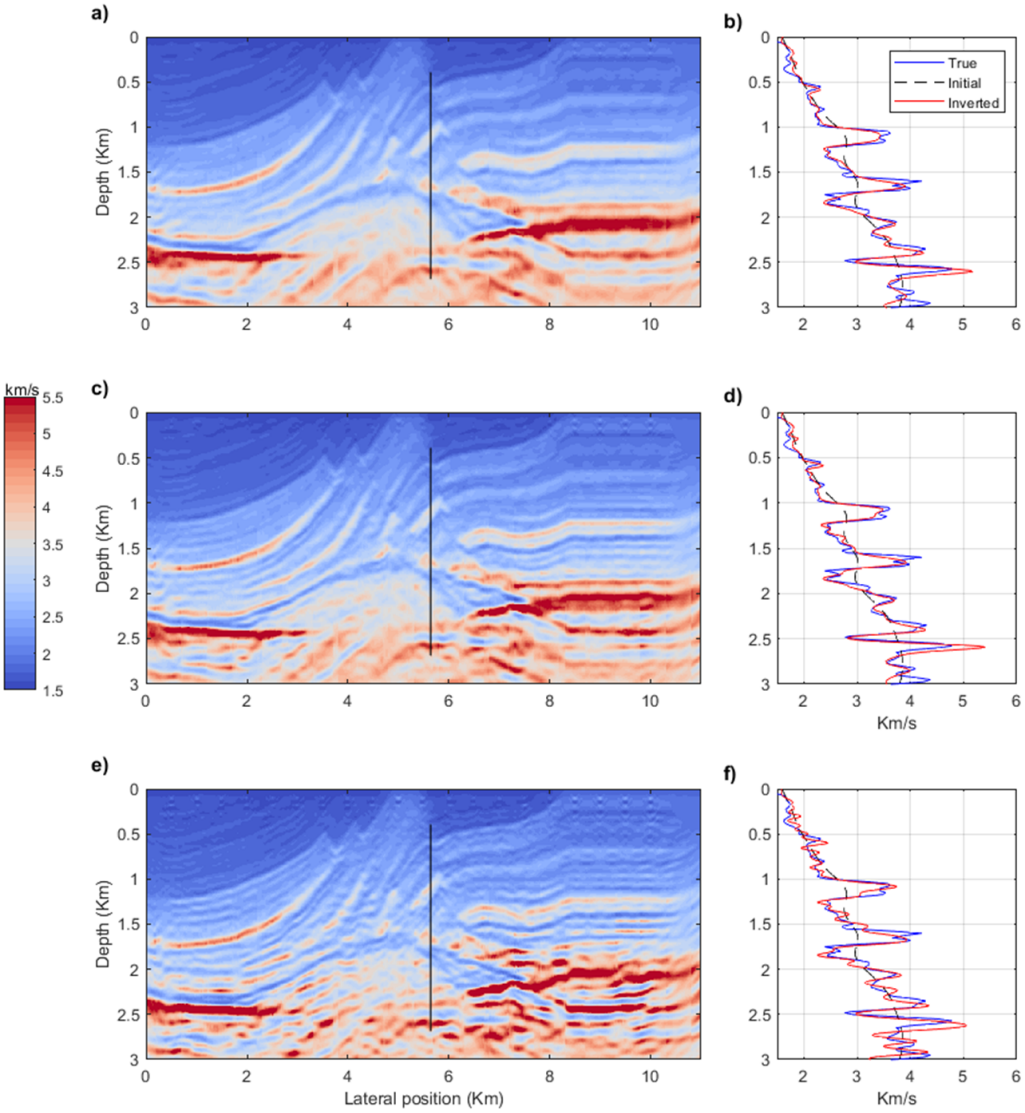

Figure 5.15: Impact of random noise in the velocity log. (a) Inverted model with no noise. (b) Inverted velocity in well location with no noise. (c) Inverted model with moderate noise. (d) Inverted velocity in well location with moderate noise. (e) Inverted model with strong noise. (f) Inverted velocity in well location with strong noise.

other data-validation methods. I evaluated the stabilizing effect of log calibration as a model-validation step under a range of adverse conditions. The tests with three velocity models indicate that increasing geological complexity degrades the effectiveness of the log-validated

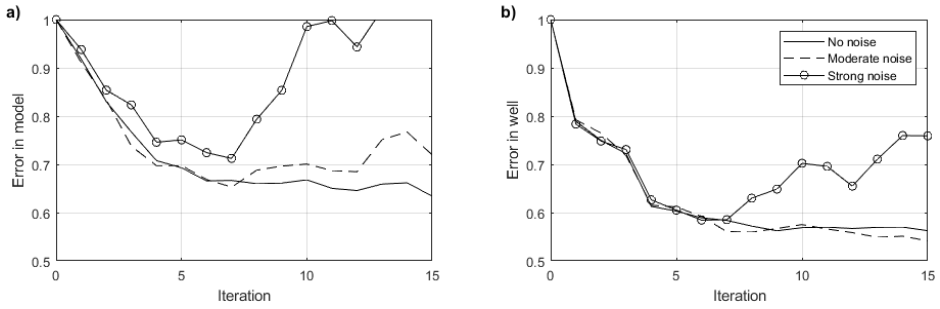

Figure 5.16: Model error comparisons for the cases of a noise-free log, and moderate and strong random noise: (a) throughout the model; (b) at the well location.

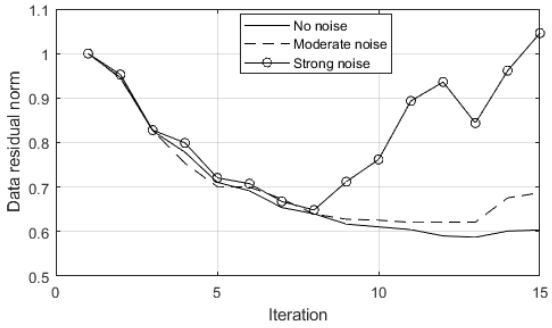

Figure 5.17: Data residual norm comparisons: (i) the log has no noise, (ii) moderate random noise; (iii) strong noise.

waveform inversion, resulting in smoother models when inverting very complex models. In a second test, I observed variations in the matched filter required to produce the exact velocity perturbation away from that produced in the vicinity of the lateral position of the well, further quantifying the issue of lateral variation and structural complexity. However, the final inverted models for three different well locations turned out to be very similar, which suggests that log-validated inversion under this factor has remarkably little sensitivity. I noted that the best result came from a well that through some averaging process represents the velocity across the model; these, of course, are only available when multiple logs are present. I also tried a matched filter computed by simultaneously using three well-logs at different locations; this scenario produced an average result when compared to the inversion obtained with the three wells, separately. In another test, the impact of the log interval

in the inversion was evaluated. Well-log validation has the best performance when the log interval is equal to or greater than 1.5 times the average wavelength determined for the first iteration. In a final test, I added a moderate and strong amount of random noise to the log. I conclude that random noise may limit the calibration capability of log validation, especially when higher frequencies are introduced in the multiscale technique.

Chapter 6

Sensitivity of well-log validated waveform inversion to survey acquisition parameters and random noise

6.1 Introduction

In Chapter 3 and 4, I formulated a log-validated waveform inversion with one-way wave equation migration whose methodology is substantially different from FWI in two main ways: 1) the update direction is obtained through one-way wave operators as a substitution for the RTM gradient, and 2) log validation is applied iteratively in order to generate the velocity perturbation, as a substitution for line search or other data-validation methods. The sensitivity of log-validated waveform inversion to several well-log factors was investigated in Chapter 5. In the current Chapter, I continue testing the performance of the log-validated waveform inversion, this time taking into account the seismic survey parameters. The seismic acquisition parameters are normally designed for imaging the main zone of interest (primary

geological target) by considering aspects such as migration apron, fold, record length, signal-to-noise ratio, etc., (Cordsen et al., 2000). Cost factors play also an important role and the economic benefits constitute a constraint when deciding the final survey parameters. Source-and-receiver intervals and maximum offset are important parameters that determine the scope and quality of the data. The smaller the source-and-receiver intervals and the larger the offset, the better the wavefield sampling, but also the survey is more expensive. These parameters also control the fold, which in turn determines the effectiveness of the stacking process for mitigating the negative effects of random noise. Intuitively, survey parameters are expected to have a strong impact in the waveform inversion, especially because the prediction of the wavefield is a fundamental element in the process. The tests in this Chapter were designed to measure the sensitivity of the waveform inversion to the survey parameters and random noise.

6.2 2D seismic survey parameters

The seismic parameter design marks the start of the seismic exploration process and it can determine the prospectivity of the study area. This section is based on Cordsen et al. (2000), who gives a detailed description of the seismic survey planning.

A 2D seismic survey is determined by three basic parameters: the source interval (SI), the receiver interval (RI) and the maximum offset (MO). These parameters control how the wavefield is sampled, and the stacking fold is a way to quantify it. The stacking fold is the number of midpoints per CMP bin (B), i.e., number of traces that contribute to one stack trace. In a 2D survey, the CMP bin is defined as a distance interval that depends on the receiver interval,

$$B = \frac{RI}{2}. \tag{6.1}$$

The 2D fold is calculated as

$$fold = \frac{\text{NC X RI}}{2\ \text{SI}}, \tag{6.2}$$

where NC is the number of active receiver stations per shot. In a symmetrical spread

$$NC = \frac{2\ \mathrm{MO}}{RI}. \tag{6.3}$$

Thus the fold is

$$fold = \frac{\mathrm{MO}}{\mathrm{SI}}. \tag{6.4}$$

Equation 6.4 says that the fold is in inverse proportion to the source interval, and is directly proportional to the maximum offset. Higher fold improves the offset distribution and contributes to increase the signal-to-noise ratio. The bin size affects the lateral distribution of the traces, but the fold is not able to show this effect because it is constant with respect to different bin sizes. A better sampling quantification is given by the linear trace density, i.e., the number of traces per km,

$$\text{trace density} = \frac{\text{Number of traces}}{km} = \frac{1000 fold}{B}, \tag{6.5}$$

where the factor 1000 converts from m to km when B is given in meters.

I will show how the basic parameters are calculated in a 2D seismic survey taking as an example the anticline model shown in Figure 6.1a.

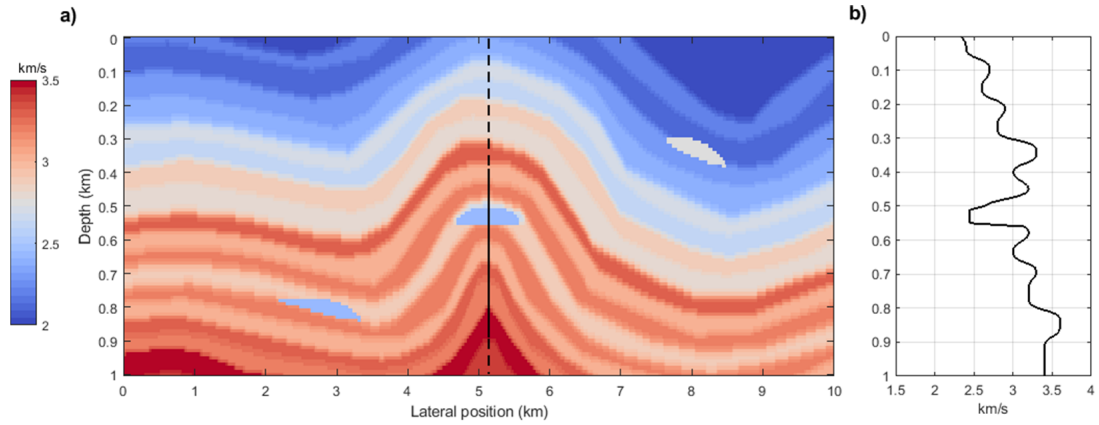

Figure 6.1: (a) Velocity model. (b) Velocity in the middle of the model.

6.2.1 Bin size

The bin size can be obtained in three different ways:

1. By considering the target size. We need at least three CMP traces sampling the target in order to laterally define it. The lateral size of the target in the middle of the model is 720m. Under this criterion the bin is

$$B \leq \frac{\text{target size}}{3} \leq \frac{750}{3} \leq 240m. \tag{6.6}$$

2. By considering the alias frequency. This criterion tries to ensure that the bin size is small enough to recover dipping events. In this case, the bin size depends on the average velocity (V_{ave}), the dominant frequency (f_{dom}) of the seismic data, and the maximum geological dip (θ), which in our example are 2760m/s, 10Hz and 16°, respectively. Under this criterion the bin is

$$B = \frac{V_{ave}}{4f_{dom}\sin\theta} = \frac{2760}{4(10)\sin 16} = 250m. \tag{6.7}$$

3. By considering the lateral resolution. This criterion is related to the ability for resolving two diffractions, which depends on the first Fresnel zone diameter. If two diffractions are closer than this zone, then they will not be resolved. The bin size is

$$B = \frac{V_{int}}{Nf_{dom}}, \tag{6.8}$$

where V_{int} is interval velocity and N is 4 or 2, assuming that the lateral resolution will be between one-quarter and one-half the dominant wavelength. The interval velocity in the geological target located in the middle of the model is 2450m/s, and the dominant frequency is 10Hz; thus $B = 61m$ for $N = 4$ or $B = 122m$ for $N = 2$.

The chosen bin size is $B = 60m$, which is the smallest one given by the three criteria,

and the correspondent receiver interval is 120m.

6.2.2 Maximum offset

The maximum offset is set up by considering the deeper targets, maximum dip and move out assumptions. For imaging purposes, the rule of thumb says that we need at least offsets as large as the deeper target (Cordsen et al., 2000). For AVO and inversion purposes larger offsets may be needed. Assuming that we are interested in knowing the spatial distribution of the high-velocity body at the deeper zone of the model, the maximum offset will be selected as 1200m.

6.2.3 Source interval

Recalling equation 6.4 and 6.5, a small source interval increases the fold and trace density, which contributes to a better offset distribution. This not only helps to improve the signal-to-noise ratio but also diminishes the survey footprint. In a 2D seismic acquisition, the distance between shots plays the role of the minimum offset (X_{min}) in a 3D survey. $Xmin$ or SI should be small enough to adequately sample shallow reflectors. The depth of the shallowest horizon to be mapped (Z_{sh}) works as a reference to select the SI. Assuming that the shallowest horizon of interest is at the depth of 240m, the source interval would be 240m.

Table 6.1 summarizes the parameters designed to acquire 2D seismic data for imaging the anticline model.

I will analyze how the waveform inversion is affected by the source interval, the receiver interval and the maximum offset in the next section.

Table 6.1: Seismic survey parameters designed for the anticline model

Bin (m)	RI (m)	SI (m)	MO (m)	Fold	Traces/km	Channels/shot	Number of shots
60	120	240	1200	5	83	20	41

6.3 Testing waveform inversion

The numerical examples in this section are designed to permit relatively broad conclusions to be made concerning the effect of the seismic survey parameters to the waveform inversion. All follow the procedure described in the workflow shown in Figure 4.6. The anticline model, employed in the numerical examples, is plotted in Figure 6.1a. The initial model, plotted in Figure 6.2a, is generated by applying a Gaussian smoother with a half-width of 200m to the true model. A minimum-phase wavelet with a dominant frequency of 10Hz is used in order to generate the synthetic shot records. A multiscale approach is implemented so that the initial frequency band is 1-6Hz and it is moved up by 1Hz in each iteration. The calibration well is located at the middle of the model 6.1b) and provides a velocity log from 400 to 900m.

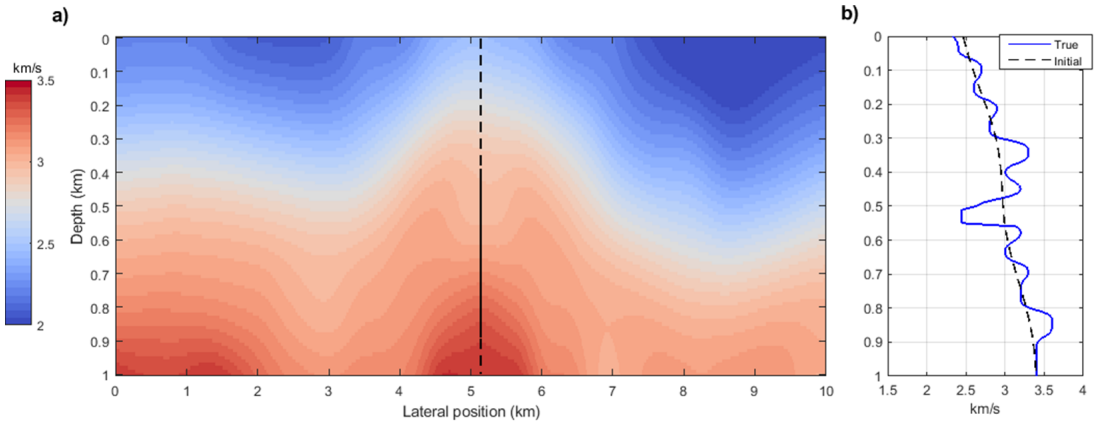

Figure 6.2: (a) Initial velocity model. (b) True and initial velocities in the well location.

The first example corresponds to the seismic parameters calculated by applying the strategies of seismic survey design (Table 6.1). The inverted model after 20 iterations is plotted in Figure 6.3. The shallow zone from 0-300 m is strongly affected by the acquisition footprint. This effect is less evident as we go to the bottom of the model. We also observe that the velocity in the bottom of the well (Figure 6.3b) has been underestimated. The model error, the velocity error in the well location and the data residual norms are plotted in Figure 6.4. Although there is some instability in the well around iteration 6, the errors and the norms

tend to decrease as we iterate.

In the next section, I will vary the source interval, receiver interval and maximum offset to investigate how these parameters influence the inversion result.

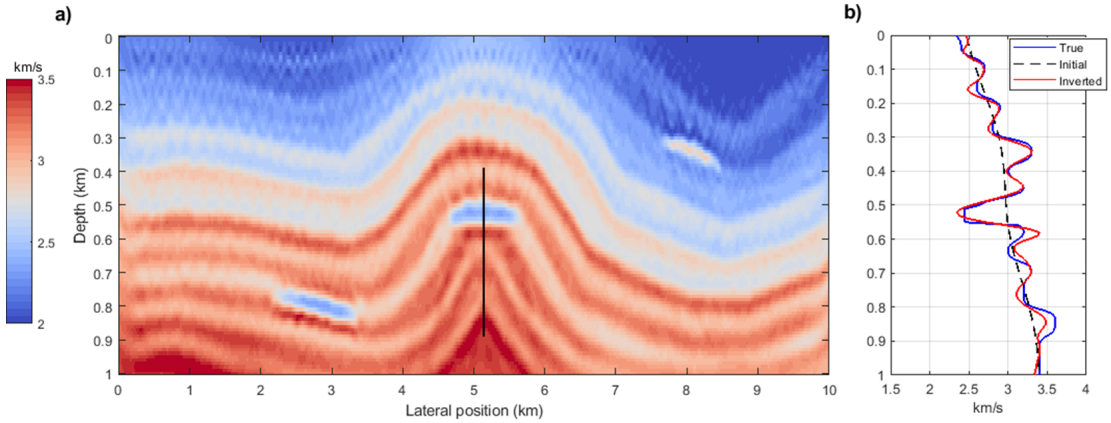

Figure 6.3: (a) Inverted velocity model after 20 iterations. The survey parameters correspond to Table 6.1. (b) True, initial and inverted velocities in the well location.

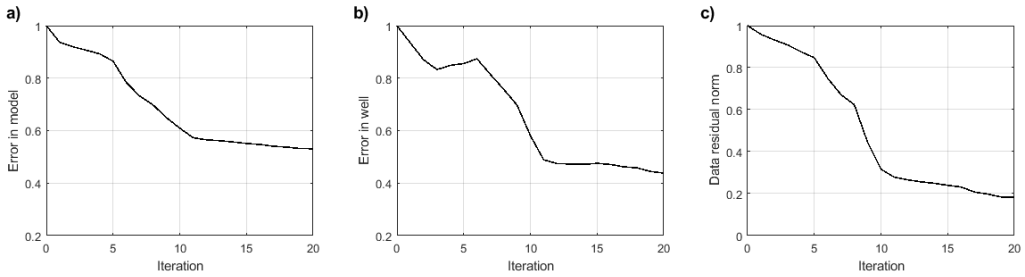

Figure 6.4: (a) Model error, (b) velocity error in the well, and (c) data residual norms for survey parameters shown in Table 6.1.

6.3.1 Sensitivity to receiver interval

In these tests, I investigate the sensitivity of the waveform inversion to the receiver interval. Table 6.2 shows the receiver intervals that are implemented. Test (i) has an extremely large receiver interval of 240m that results in $B = 120m$. Test (ii) implements the receiver interval calculated by the lateral resolution criterion with $N = 4$, which is 120m. Test (iii) has a $RI = 10m$, which is much smaller than the design requirement. Table 6.2 shows that the

fold does not change when RI varies so that the trace density represents better the bin size repercussion to the trace distribution. As the bin size becomes smaller, the trace density increases.

The final model and the inverted velocity in the well after 20 iterations are plotted in Figure 6.5 for (a-b) $RI = 240m$, (c-d) $RI = 120m$, and (e-f) $RI = 10m$. The larger the receiver interval, the stronger the acquisition footprint, especially in the shallow zone. The high-velocity body, located at the right-hand side of the model at a depth of 300m, is strongly affected by an inadequate large receiver interval, appearing discontinuous and blurry. The continuity of the anticline top, signed by an arrow, drastically improves when the RI is reduced. Even the velocity at the bottom of the model is better recovered by $RI = 120$, as it is shown by the black arrows in the inverted velocity in the well. The data residuals after 20 iterations for (a) $RI = 240m$, (b) $RI = 120m$, and (c) $RI = 10m$ are plotted in Figure 6.6. The effect of large receiver intervals is represented by the discontinuous horizons. The model error, the velocity error in the well and the data residual norms, plotted in Figure 6.7(a-c), show that the $RI = 120m$ (calculated with the lateral resolution criterion) has a similar performance than $RI = 10$. But receiver intervals larger than $RI = 120m$, increase the error in the inversion because of the discontinuous character of the horizons in the shallow zone.

Table 6.2: Varying receiver interval

Test	Bin (m)	RI (m)	SI (m)	MO (m)	Fold	Traces/km	Channels/shot	Num. Shots
i	120	240	240	1200	5	42	10	41
ii	60	120	240	1200	5	83	20	41
iii	5	10	240	1200	5	1000	220	41

6.3.2 Sensitivity to source interval

Table 6.3 shows three sets of seismic parameters that are used to evaluate the effect of the source interval in the inversion performance. The receiver interval and the maximum offset were fixed at 10m and 1200m, respectively. Test (i) employs a $SI = 600m$, which results in an extremely low fold of 2 and a density of 400 traces per km. Test (ii) uses a $SI = 240m$

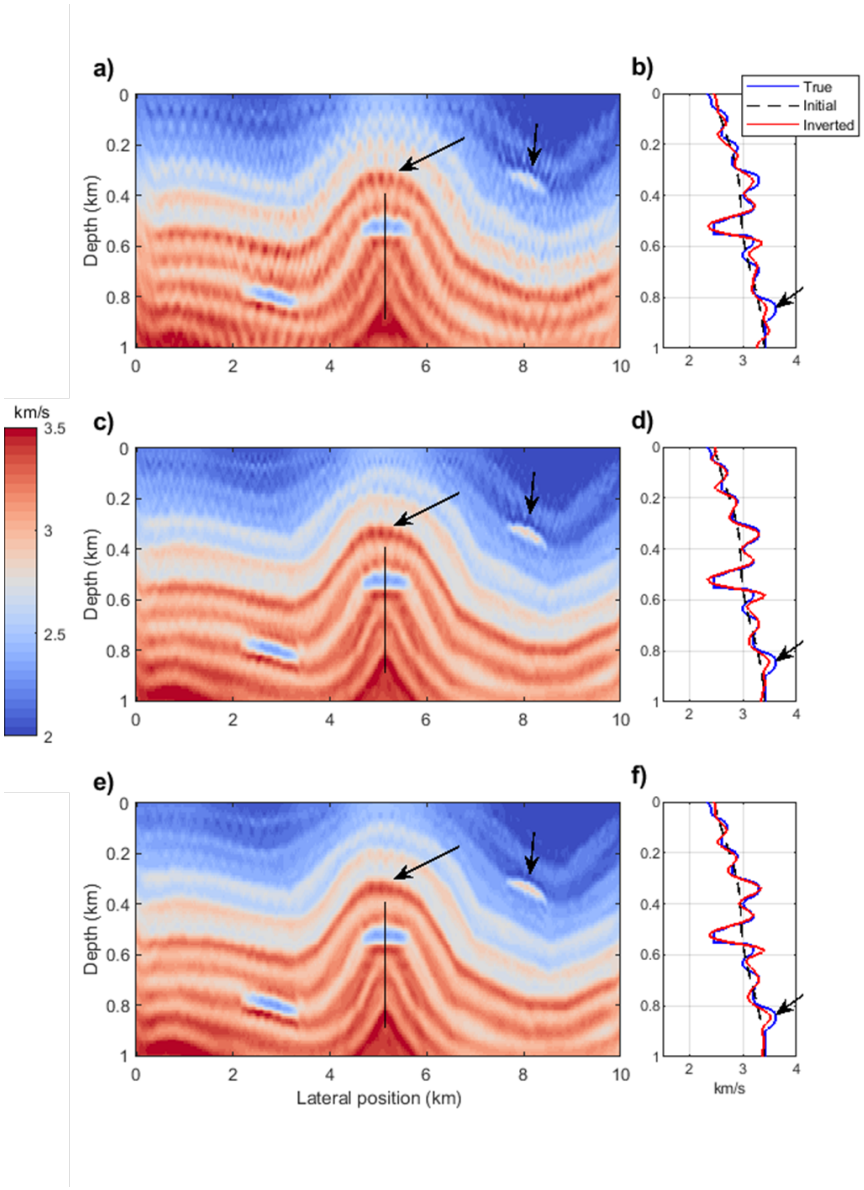

Figure 6.5: Final model and inverted velocity in the calibration well after 20 iterations for (a-b) RI = 240m, (c-d) RI = 120m, and (e-f) RI = 10m.

producing a fold of 5 and 1000 traces per km. A $SI = 120m$ was employed in test (iii), generating a fold of 10 and 2000 traces per km. The number of shots is 16, 41 and 83 for (i), (ii) and (iii), respectively. The final model and the inverted velocity in the well after 20 iterations are plotted in Figure 6.8 for (a-b) $SI = 600m$, (c-d) $SI = 240m$, and (e-f) $SI = 120m$. The model, the velocity error in the well, and the data residual norms are

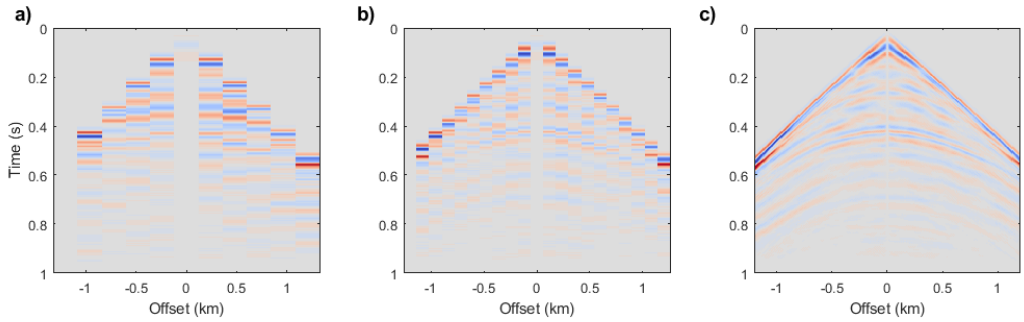

Figure 6.6: Data residual after 20 iterations for (a) RI = 240m, (b) RI = 120m, and (c) RI = 10m.

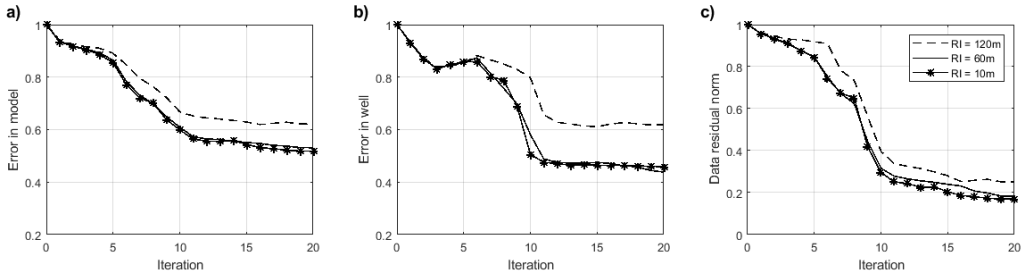

Figure 6.7: (a) Model error, (b) velocity error in the well location and (c) data residual norms for (i) RI = 240m, (ii) RI = 120m, and (iii) RI = 10m.

Table 6.3: Varying source interval

Test	Bin (m)	RI (m)	SI (m)	MO (m)	Fold	Traces/km	Channels/shot	Num. Shots
i	5	10	600	1200	2	400	240	16
ii	5	10	240	1200	5	1000	240	41
iii	5	10	120	1200	10	2000	240	83

plotted in Figure 6.9(a-c). The largest SI compromises the mapping of the shallow horizons, which virtually disappear from 0-250m of depth at the left-hand side of the model. The low-velocity target, located at a depth of 500m in the middle of the model, is also affected by this large SI, having an undulating appearance. Even this SI has an impact at the bottom of the model, as it is shown in the well location, where the velocity is highly underestimated from 800 to 900m. All these negative effects are reflected in the errors, which tend to be higher than the errors produced by smaller source intervals. Even though $SI = 240m$ and $SI = 120m$ have similar errors, the latter produces clearer and more continuous horizons

in the shallow zone. The results suggest that small source intervals benefit the inversion performance by improving the sampling in the shallow zone. The insignificant differences in the errors and norms for $SI = 240m$ and $SI = 120m$, indicate that there is a point where reducing the SI does not have a relevant impact in the inversion performance anymore, that is, $SI < 120$ will have no impact in the final result for this anticline model.

The role of pre-stack mute

The waveform inversion, under IMMI's perspective, incorporates standard processing tools in the FWI workflow (Margrave et al., 2012a). The implementation of a pre-stack mute after migrating the data residual is naturally integrated into the process, aiming to account for migration artifacts. Figure 6.10 shows an example of a migrated data residual for iteration 1 and three mute options: (a) narrow mute, (b) wide mute, and (c) no-mute. In this section, I investigate the effect of applying these pre-stack mutes in the data with parameter (i) and (iii) in Table 6.3, which correspond to a large ($SI = 600m$) and small source interval ($SI = 120m$), respectively.

Figure 6.11 shows, from top to bottom, the inverted model when a narrow mute, wide mute and no-mute are applied. Columns (a) and (b) correspond $SI = 600m$ and $SI = 120m$, respectively. The errors through the model for $SI = 600m$ and $SI = 120m$ are plotted in Figure 6.12(a-b). The results suggest that a narrow mute deteriorates the inverted model especially for the case of large source intervals. When a small source interval is employed, the process is less sensitive to the pre-stack mute.

6.3.3 Sensitivity to maximum offset

In these tests, three different maximum offsets are employed to investigate the sensitivity of the waveform inversion to this parameter. Table 6.4 shows the seismic survey parameters used in each test. The receiver and source intervals were fixed at 10m and 120m, respectively. A maximum offset of 480m was used in test (i), resulting in a $fold = 4$ and a density of 800

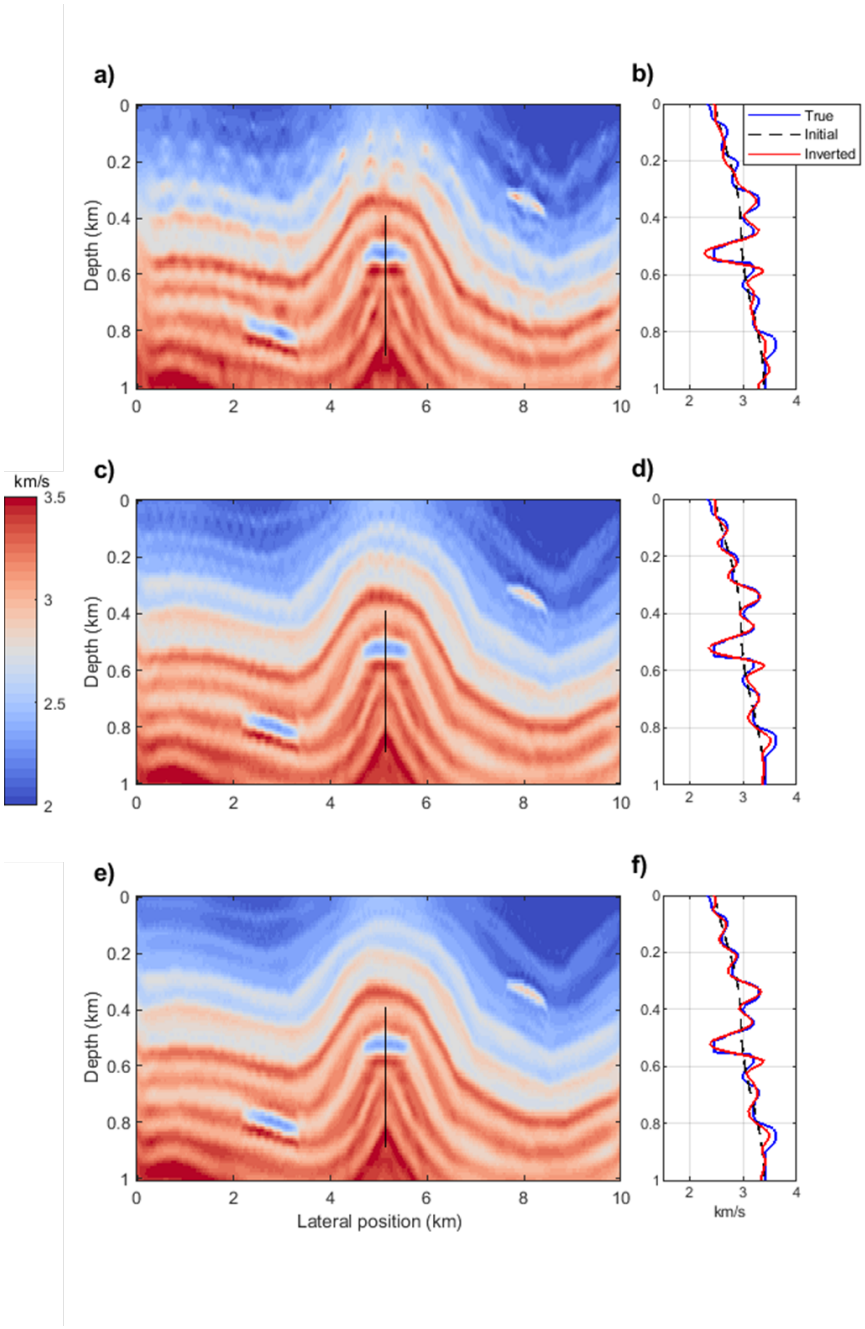

Figure 6.8: Final model and inverted velocity in the calibration well after 20 iterations for (a-b) SI = 480m, (c-d) SI = 240m, and (e-f) SI = 120m.

traces per km. Test (ii) employs a maximum offset of 1200m, which generates a $fold = 10$ and 2000 traces per km. Test (iii) uses a maximum offset of 2400m, producing a $fold = 20$ and 4000 traces per km. The trace density of the parameter set (iii) can be broken down

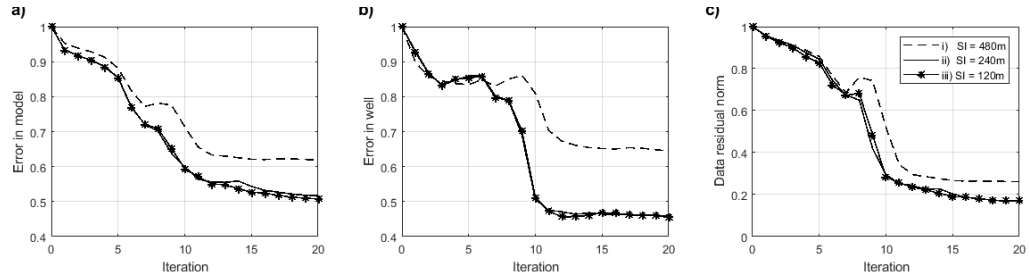

Figure 6.9: (a) Model error, (b) velocity error in the well location and (c) data residual norms for (i) SI = 480m, (ii) SI = 240m, and (iii) SI = 120m.

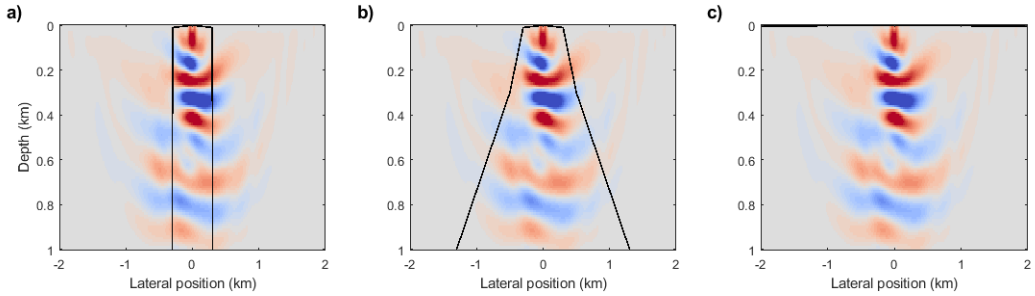

Figure 6.10: (a) Narrow mute. (b) Wide mute. (c) No mute.

as 800 traces with offsets from 0-480m, 1200 traces with offsets from 800-1200m and 2000 traces with offsets from 1200-2400m.

Table 6.4: Varying maximum offset

Test	Bin (m)	RI (m)	SI (m)	MO (m)	Fold	Traces/km	Channels/shot	Num. Shots
i	5	10	120	480	4	800	96	83
ii	5	10	120	1200	10	2000	240	83
iii	5	10	120	2400	20	4000	480	83

The final model and the inverted velocity in the well after 20 iterations are plotted in Figure 6.13 for (a-b) $MO = 480m$, (c-d) $MO = 1200m$, and (e-f) $MO = 2400m$. The model error, the velocity error in the well, and the data residual norms are plotted in Figure 6.14(a-c). Arrows indicate the strong impact that the lack of offsets longer than 480m has in the final inverted model. The velocity at the top of the anticline has been under or overestimated, a blurry character dominates in the steepest events, and strong amplitudes appear below the high-velocity body at the left-hand side of the model. The errors and

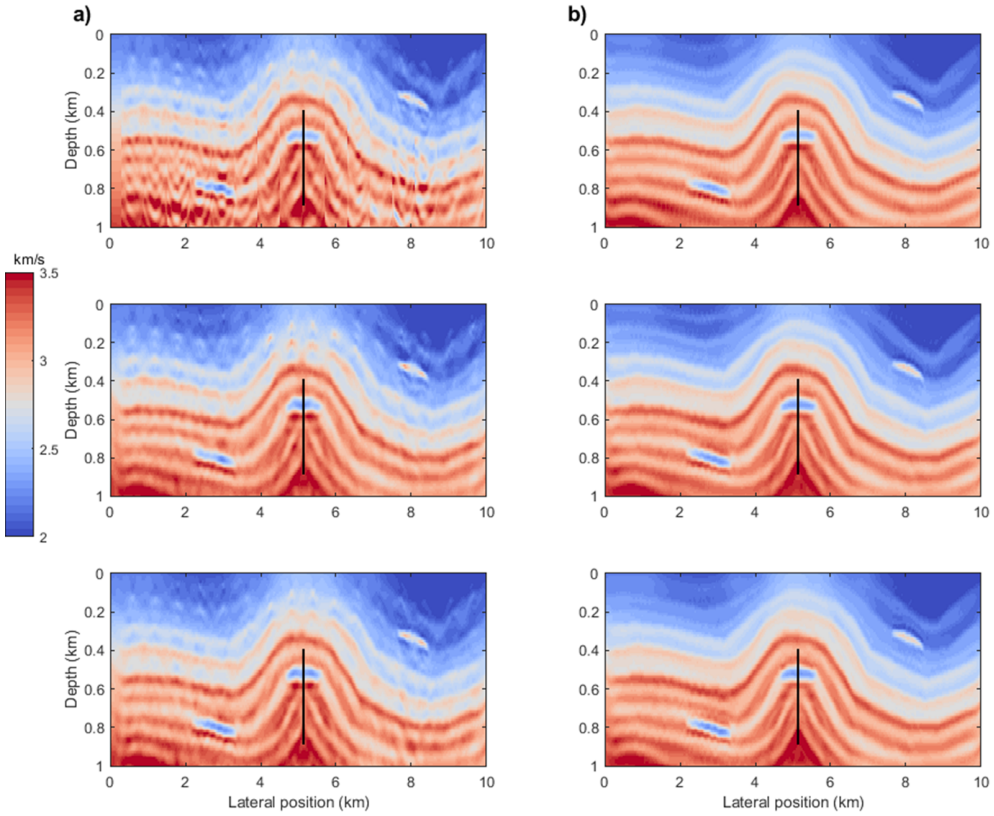

Figure 6.11: Inverted model after 20 iterations for (a) $SI = 600m$ and (b) $SI = 120m$. From top to bottom: narrow mute, wide mute and no-mute.

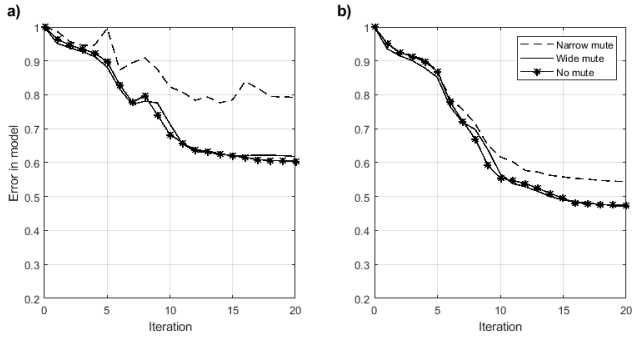

Figure 6.12: Model error for (a) $SI = 600m$ and (b) $SI = 120m$ by applying a narrow mute, wide mute, and without any mute.

norms for the maximum offset of 480m are unstable from iterations 4-7. These problems are overcome when offsets longer than 1200m are employed. The contribution of offsets longer

than 1200m is also reflected at the bottom of the model as it is shown in the inverted velocity in the well from 800-900m, where the velocity is being properly recovered. The model error is similar for maximum offsets of 1200m and 2400m, but the error in the calibration well is smaller when offsets longer than 1200m are incorporated. The data residual norms tend to decrease in each iteration when maximum offsets of 1200m and greater are employed.

It has been documented that long offsets contribute to recovering long wavelengths in FWI, which mitigates the sensitivity to the initial model (Gauthier, 1986; Pratt, 1999; Kazei et al., 2013). An examination of the amplitude spectra of the inverted-model reflectivity for the three maximum-offset scenarios (Figure 6.15) suggests that the waveform inversion with one-way equation migration can, in some degree, incorporate long wavelength information from long offsets. I will evaluate this idea in the next Chapter. The amplitude spectra for $MO = 1200m$ and $MO = 2400m$ are similar, both of them having a jump around 5HZ which is not present in the $MO = 480m$ case. This difference explains some of the problems found in the shallow zone of the inverted model for $MO = 480m$. I conclude that the maximum offset is important to resolve dipping events and provides stability to the inversion by incorporating long wavelengths from long-offset traces.

6.3.4 Sensitivity to random noise

There are different types of noise that may affect the inversion performance. Noise can be classified in two main categories: random and coherent. In the latter case, we may consider noise the events that we are not able to reproduce or manage in our forward modelling, for instance, in the acoustic approach the ground roll is not taken into account and must be attenuated from the field shot records. Multiples may be also considered noise and should be treated before applying the inversion. In this section, I only considered the effect of random noise which I assumed uniformly distributed.

Two sets of parameters, shown in Table 6.5, that produce similar inversion results when no noise is involved, are selected to test the impact of random noise on the inversion result.

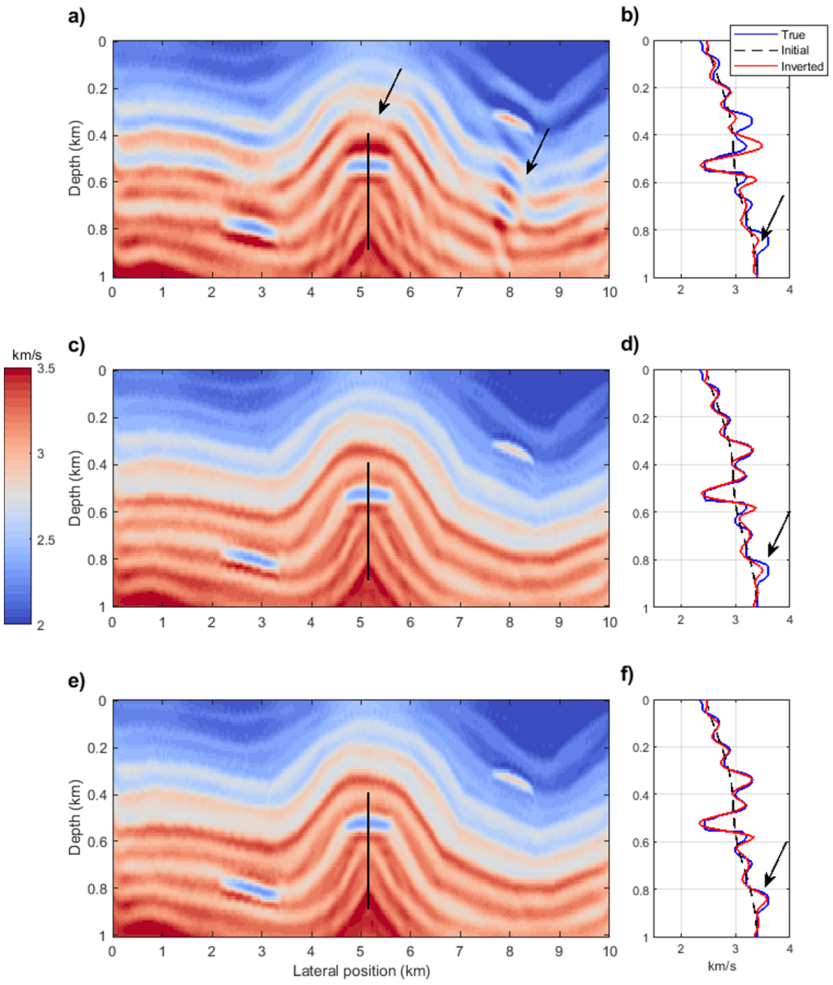

Figure 6.13: Final model and inverted velocity in the calibration well after 20 iterations for (a-b) MO = 480m, (c-d) MO = 1200m, and (e-f) MO = 2400m.

The first set of parameters (i) corresponds to the ones calculated in the survey design in section 6.2.1. They include the minimum required for imaging the anticline model and work in an acceptable manner where no noise is involved. The parameters set (ii) represents a more robust acquisition survey where the receiver and source intervals have been reduced, and the maximum offset has been increased. Survey (i) has double the shots than survey (ii); however, most of the acquisition effort is put in the receivers. The trace density reflects the main difference between these two options. The first parameter set has only 83 traces

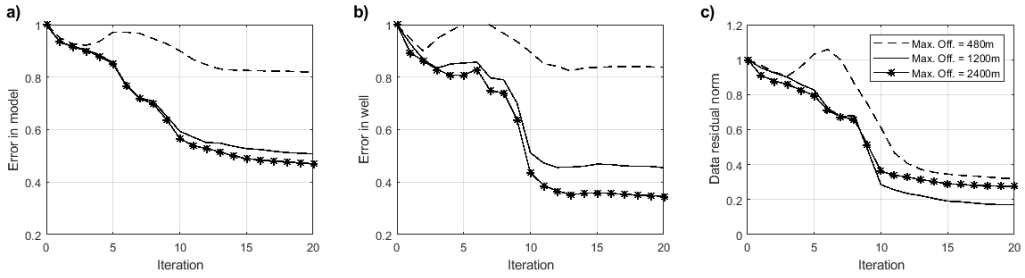

Figure 6.14: (a) Model error, (b) velocity error in the well location and (c) data residual norms for (i) MO = 480m, (ii) MO = 1200m, and (iii) MO = 2400m.

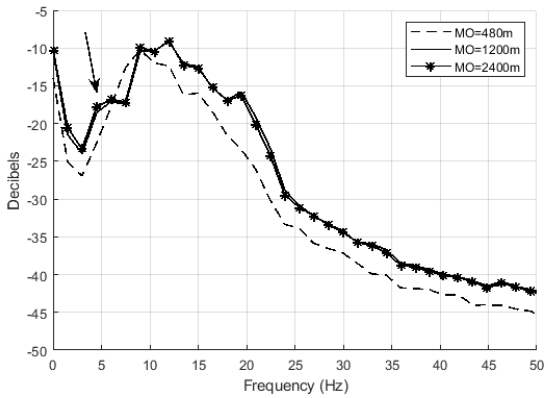

Figure 6.15: Amplitude spectra of the inverted-model reflectivity for $MO = 480m$, $MO = 1200m$ and $MO = 2400m$.

per km, while the second option incorporates 4000 traces per km.

To evaluate the consequences for the inversion of uncertainty within the seismic data, I next reconsider the inversions with random noise added to the seismic shot records. I set up the root mean squared amplitude of the noise (RMS_{noise}) by dividing the root mean squared amplitude in the shots (RMS_{shot}) by the desired signal-to-noise ratio (SN)

$$RMS_{noise} = \frac{RMS_{shot}}{SN}. \tag{6.9}$$

The signal-to-noise ratio was selected as 1. Note that the noise amplitude depends on the spatial and time windows selected to measure RMS_{shot}. The comparison between a shot with and without random noise is shown in Figure 6.16.

The comparison between the inverted model with and without noise for the parameter set (i) is plotted in Figure 6.17a-b. The same is plotted for the parameter set (ii) in Figure 6.18a-b. The model error for the scenarios with and without noise are plotted in Figure 6.19. Although the results are similar when no noise is involved, the presence of random noise strongly deteriorates the result when parameters (i) are employed. On the other hand, the robust survey is able to manage better random noise resulting in an inverted model very similar to the case with no noise. This experiment demonstrates the importance of high trace density when dealing with noise. I conclude that random noise should be taken into account when designing the seismic acquisition parameters and that the waveform inversion with proper parameter setting is able to produce meaningful results with noisy shot records.

Table 6.5: Random noise test

Test	Bin (m)	RI (m)	SI (m)	MO (m)	Fold	Traces/km	Channels/shot	Num. Shots
i	60	120	240	1200	5	83	20	41
ii	5	10	120	2400	20	4000	480	83

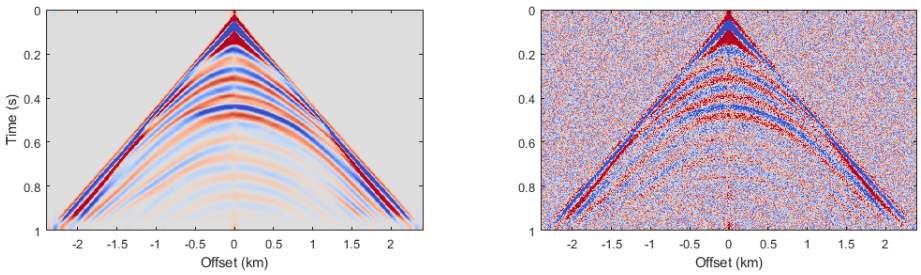

Figure 6.16: (a) Shot without noise. (b) Shot with random noise equivalent to $S/N = 1$.

6.4 Conclusions

The performance of log-validated waveform inversion was evaluated under a range of different survey acquisition parameters. The tests included varying the receiver interval, source interval, and maximum offset. I also included the factor of random noise to investigate the

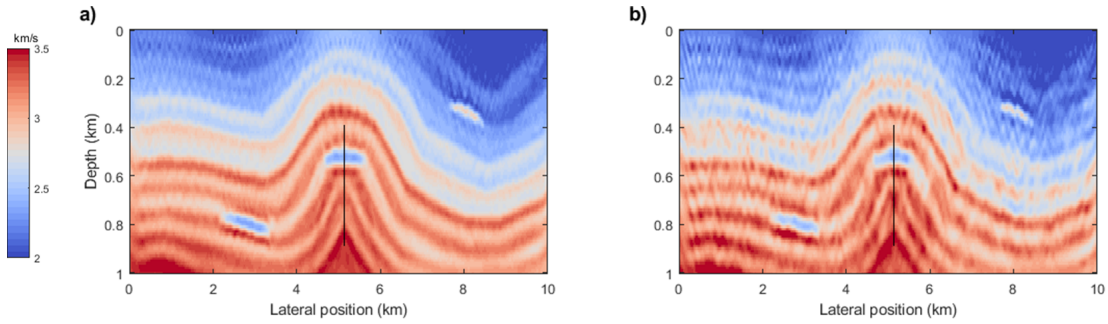

Figure 6.17: Inverted model after 20 iterations for seismic survey parameters in Table 6.5i (a) without and (b) with random noise equivalent to $S/N = 1$.

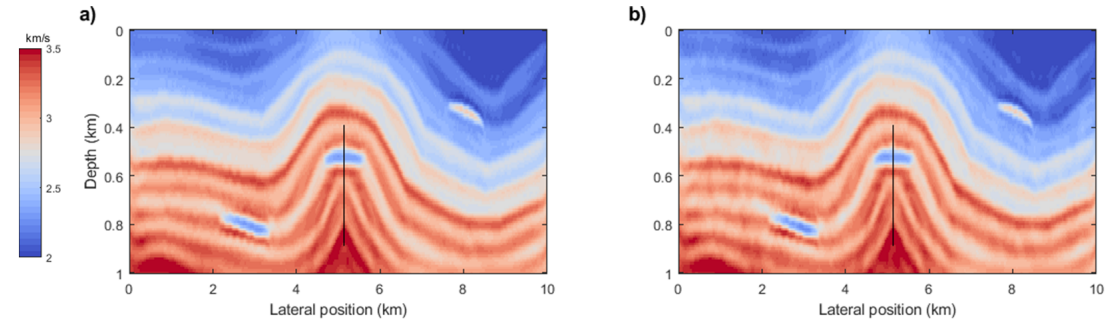

Figure 6.18: Inverted model after 20 iterations for seismic survey parameters in Table 6.5ii (a) without and (b) with random noise equivalent to $S/N = 1$.

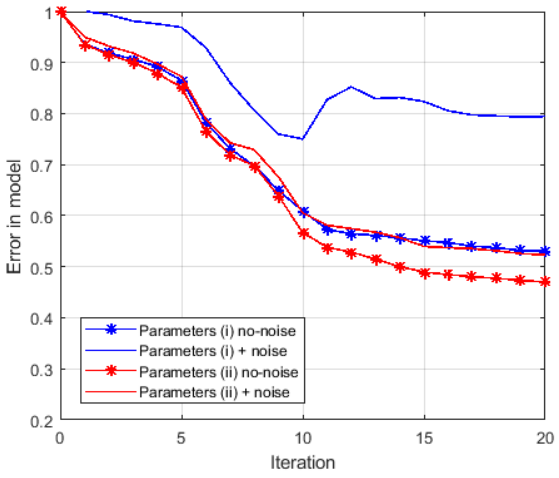

Figure 6.19: Model error for seismic survey parameters in Table 6.5i-ii with and without random noise equivalent to $S/N = 1$.

effect of uncertainty in the seismic data in the inversion result. The receiver interval, which controls the bin size and impacts the trace distribution, showed to be important to provide continuity to the horizons. If this parameter is properly selected following the design recommendations, the inversion is relatively insensitive. On the other hand, the source interval has the potential to damage the inversion result especially in the shallow zone of the model, because it controls how the horizons close to the surface are mapped. The inversion is very sensitive to a large source interval because it is exposed to a strong acquisition footprint. Furthermore, the mute before stacking the migrated data residual has little influence for small source intervals, but it has to be properly selected when using large source intervals. The maximum offset not only contributes to imaging the steepest horizons but also provides stability of the inversion in shallow events by incorporating long wavelengths from long-offset traces. In a final test, I added random noise equivalent to a signal-to-noise ratio equals to 1. The results with two survey parameter sets, one with poor trace density and another with relatively high trace density, allow concluding that this factor is relevant when designing the survey and that the waveform inversion with high trace density is able to produce meaningful results when applied in noisy shot records.

Chapter 7

Sensitivity of waveform inversion to the initial model

7.1 Introduction

FWI is formulated as a data-fitting least-squares minimization problem that iteratively updates an initial velocity model with the scaled gradient of the misfit until a satisfactory match between the real and synthetic data is obtained. The lack of convergence to the subsurface model when the seismic data does not have enough low frequencies or when a sufficiently accurate initial model is not provided is a common problem in this local optimization approach (Virieux and Operto, 2009). Local minima impede iterative techniques from finding the global minimum unless the initial model for the velocity field is already in the neighborhood of the global solution. Multiscale approaches can help to attain a reasonable degree of convergence to the neighborhood of the global minimum by the selection of a suitable sequence of frequencies in the inversion (Bunks et al., 1995; Pratt, 1999). Sufficient long offsets contribute to reconstructing the long wavelength components (Kazei et al., 2013). However, the multiscale approach and long offsets may not be enough to avoid being trapped in a local minimum when the initial model is deficient. Building accurate starting models (Datta and

Sen, 2016; Prieux et al., 2013; Chauris et al., 2008) and/or recording low frequencies (Plessix et al., 2010; Soubaras and Whiting, 2011) are ongoing and important research topics. In this Chapter, I investigate the sensitivity of log-validated waveform inversion to the initial model and compare its performance to the conventional FWI.

7.2 Sensitivity to the initial model

Two different initial models, plotted in Figure 7.1b-c, are employed to investigate the impact of this input in the inversion. One model, which I will refer to as GS200, is generated by applying a Gaussian smoother with a half-width of 200m to the true model plotted in Figure 7.1a. A half-width of 500m is used to generate a smoother model, which it is called GS500. Figure 7.2 shows the velocity at a well located in the middle of the model for the true and the initial models GS200 and GS500. Figure 7.3 plots the amplitude spectra of the true and the initial models, so we can observe their frequency contribution. Model GS500 supplies up to 2Hz of information, while model GS200 contributes up to 3Hz. We will see that this small change in the spectrum has a significant impact on the inversion especially for the case of well-log validated waveform inversion.

I will compare the sensitivity of two inversion workflows to the initial velocity model:

1. Conventional FWI. The update direction is produced by RTM migration of the data residuals, and data validation is applied to produce the velocity perturbation. The FWI workflow is shown in Figure 2.2. In these tests, the data validation process is carried out by applying Tarantola-and-Pica's approach (section 2.3.1) with 5 shots distributed along the surface.

2. Well-log validated waveform inversion. The update direction is obtained via PSPI migration and impedance inversion. The velocity perturbation is produced by applying well-log validation. The workflow is shown in Figure 4.6. The calibration well is located at the middle of the model and provides a velocity log from 400 to 900m.

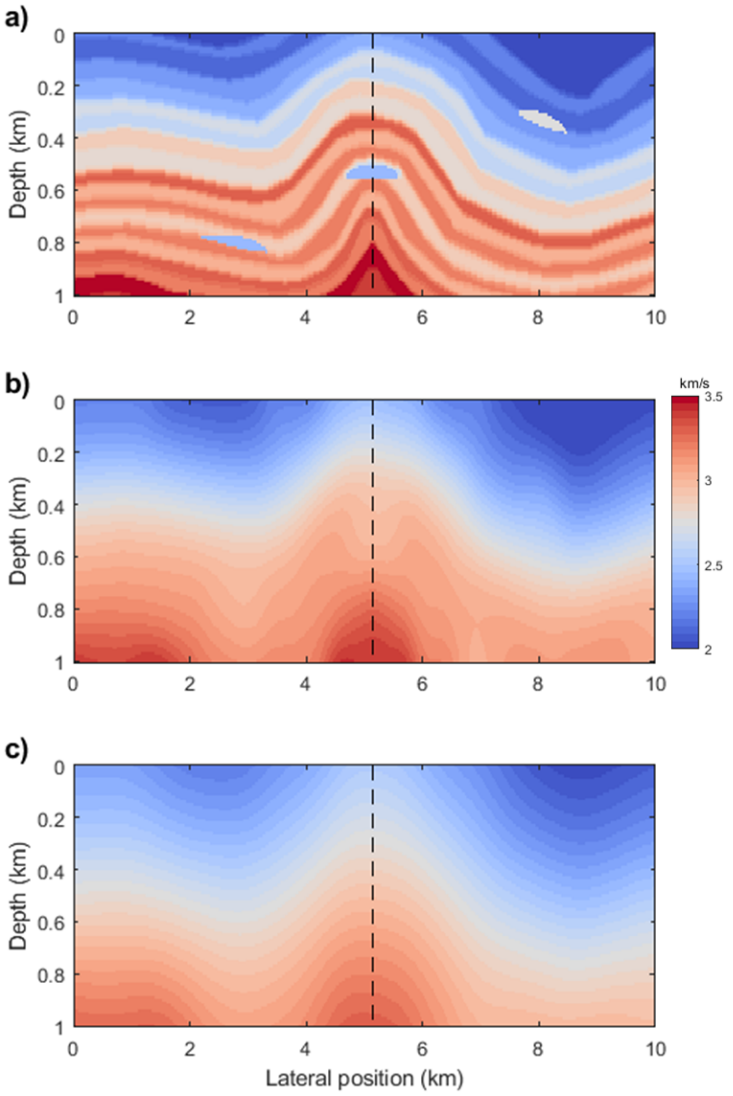

Figure 7.1: (a) True velocity model. (b) Initial model GS200 generated by applying a Gaussian smoother with a half-width of 200m. (c) Initial model GS500 generated by applying a Gaussian smoother with a half-width of 500m.

The observed shot records are generated by propagating a minimum-phase wavelet with a dominant frequency of 10Hz through the true model. The source and receiver intervals are 120m and 10m, respectively. The total number of shots is 83. All receiver stations are kept alive for each shot. The maximum offset is 2400m for a recorded time of 1 second.

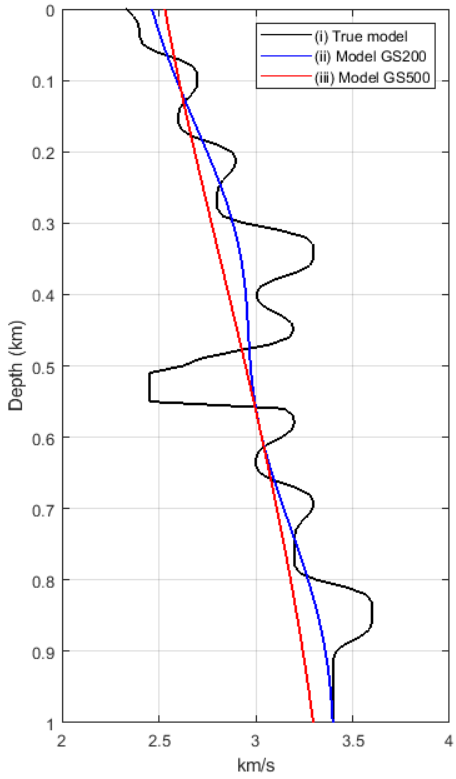

Figure 7.2: Velocities in a well located at the middle of the model for (i) the true model, (ii) initial model GS200, and (iii) initial model GS500.

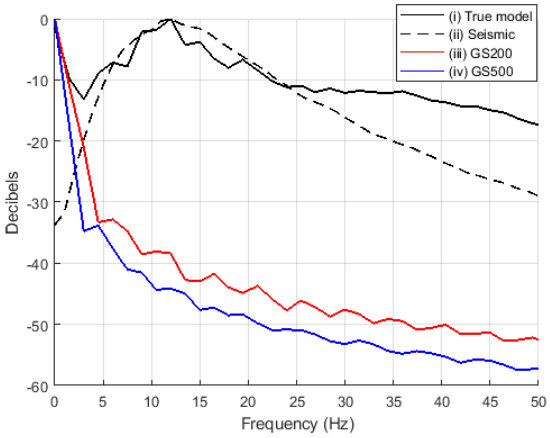

Figure 7.3: Amplitude spectra of the reflectivity for (i) the true model, (ii) seismic data, (iii) model GS200, and (iv) model GS500.

A multiscale approach is implemented so that the initial frequency band is 1-6Hz and it is moved up by 1Hz in each iteration. A 2D medium governed by the constant density acoustic wave equation is assumed to hold. The simulations are carried out with a fourth-order finite difference scalar acoustic algorithm.

The inverted model and the error distribution across the model after 20 iterations are plotted in Figure 7.4 for (a-b) FWI workflow and initial model GS200, (c-d) FWI workflow and initial model GS500, (e-f) log-validated waveform inversion workflow and initial model GS200, and (g-h) log-validated waveform inversion workflow and initial model GS500. Figure 7.5 shows the model error, the velocity error in the calibration well and the data residual norms with iteration for the four scenarios. When the starting model is GS200, both inversion methods achieve similar results and are able to recover the true model. There is a slightly higher error distributed across the model for the case of well-log validated waveform inversion, which does not significantly affect the final result. On the other hand, when the initial model is GS500, both inversion methods showed to be sensitive to the initial model but in different degrees. Conventional FWI seems to have no problem to recover long-wavelength information in the shallow zone. Errors across the model, from 0 to 400m of depth, are similarly low as in the case when the model GS200 was used; however, the inversion result degrades as we go to deeper zones. Well-log validated waveform inversion with PSPI update direction is more sensitive to the lack of long wavelengths in the initial model. The high error evenly distributed across the model indicates that this inversion method has limitations to recover low-frequency information even in the shallow zone. The amplitude spectra of the inverted-model reflectivity after 20 iterations, when the initial model is GS200, is shown in Figure 7.6a. The amplitude spectrum of the true model is also plotted as a reference. Both inversion methods produce models with similar frequency content from 0 to 18Hz, which are able to efficiently recover the low-frequency information of the true model. The amplitude spectrum, when the initial model is GS500, is plotted in Figure 7.6b. In this case, well-log validated waveform inversion has problems to retrieve frequencies from 0 to 4Hz, which is

not happening when conventional FWI is applied.

The update directions in the first iteration when we are employing a frequency band from 1 to 6Hz are shown in Figure 7.7 for (a) the conventional FWI and (b) log-validated waveform inversion. The former is providing significantly more information in the shallow zone, which makes the difference in the inversion result.

7.3 Where does the long-wavelength information come from?

The next test is set up with the purpose of understanding which seismic events contribute to the long-wavelength information in the inversion. I assumed that the true subsurface model is GS200 and the starting model is GS500. The same minimum-phase wavelet (10Hz dominant frequency), used in the previous examples, was employed to generate the observed shot record plotted in Figure 7.8a. This shot does not have significant reflection energy. The dominant event is constituted by the first arrivals which include the direct, head and diving waves. An example of the modelled shot record that corresponds to the initial model is plotted in Figure 7.8b. In the data residual, shown in Figure 7.8c, the direct wave has been subtracted remaining the head and diving waves. These events will contribute to constructing the update direction for this early stage in the process. Conventional FWI was implemented to obtain the velocity perturbations plotted in Figure 7.9. We observe that most of the energy is concentrated in the shallow zone. The inversion result and the error distribution through the model after 5 iterations are plotted in Figure 7.10a-b. The inverted velocity in the well location is shown in Figure 7.11. The results confirm that head and diving waves represent a source of low-frequency information for FWI as it has been documented in Kazei et al. (2013).

There is still a question about the limitation of FWI to properly recover the velocity in the deeper zone of the model. The answer is given by the way the seismic waves travel through

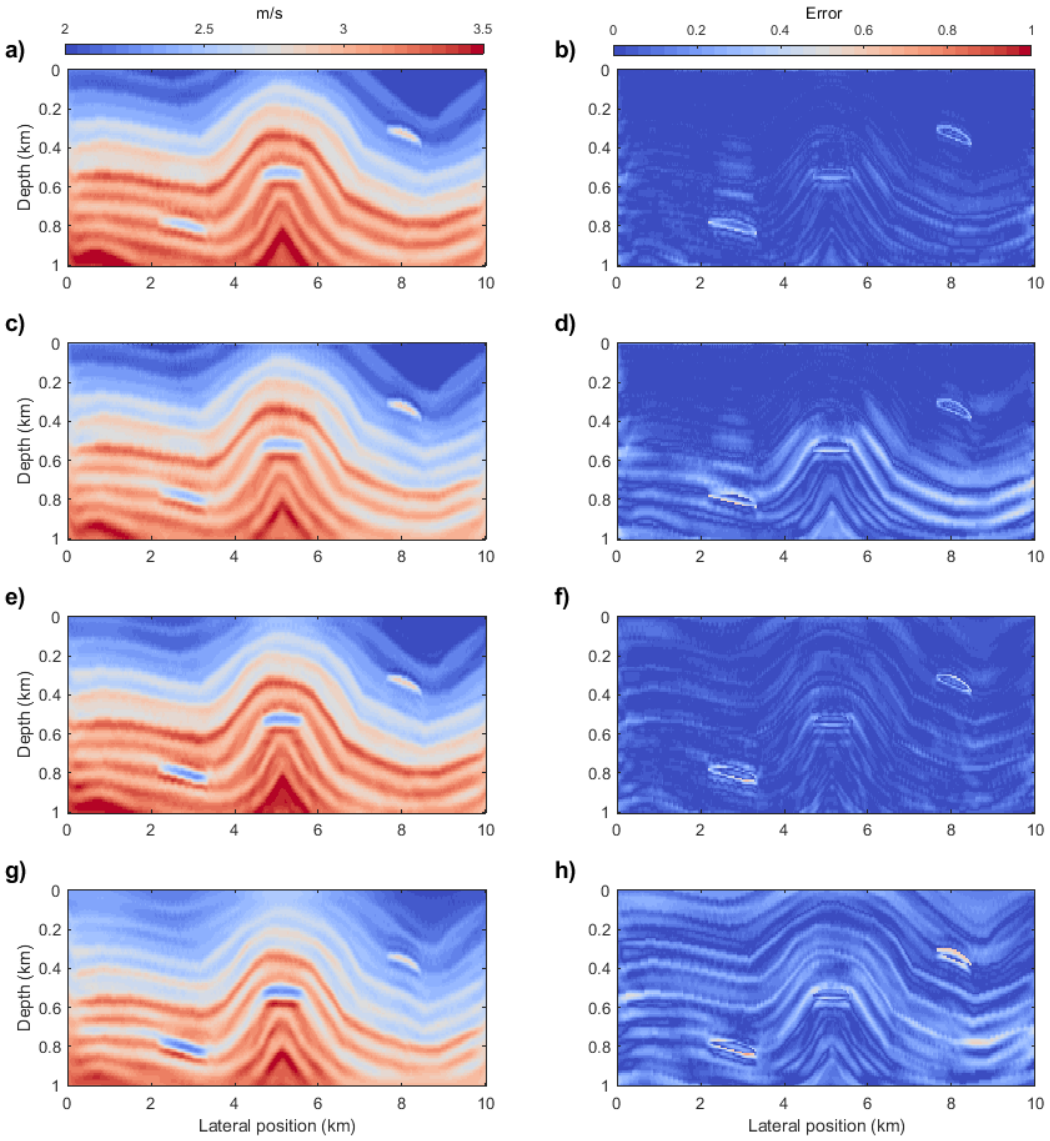

Figure 7.4: Inverted model and distribution of the error across the model for (a-b) FWI workflow and initial model GS200, (c-d) FWI workflow and initial model GS500, (e-f) log-validated waveform inversion workflow and initial model GS200, and (g-h) log-validated waveform inversion workflow and initial model GS500.

the medium. Figure 7.12 shows the ray tracing through the true model for three different shots. We observed that the diving waves penetrate up to 600m of depth. These waves contribute to reconstructing the low-frequency components during the inversion. Therefore,

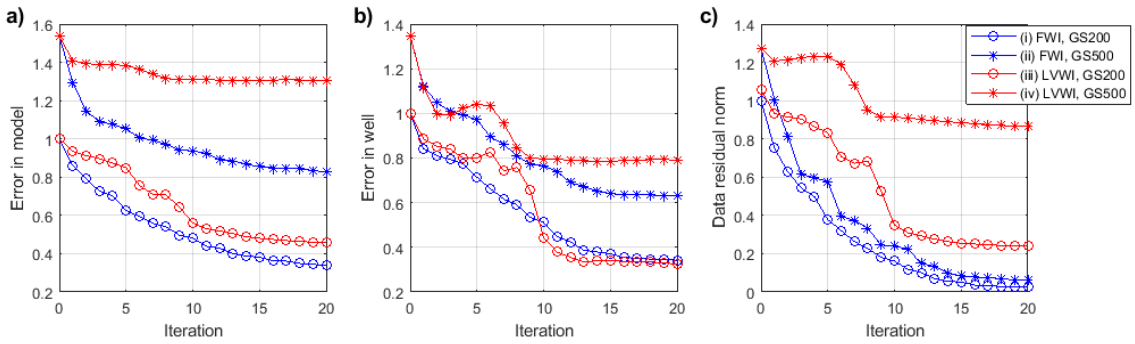

Figure 7.5: (a) Model error, (b) velocity error in the calibration well, and (c) data residual norms for (i) FWI workflow and initial model GS200, (ii) FWI workflow and initial model GS500, (iii) log-validated waveform inversion workflow and initial model GS200, and (iv) log-validated waveform inversion workflow and initial model GS500.

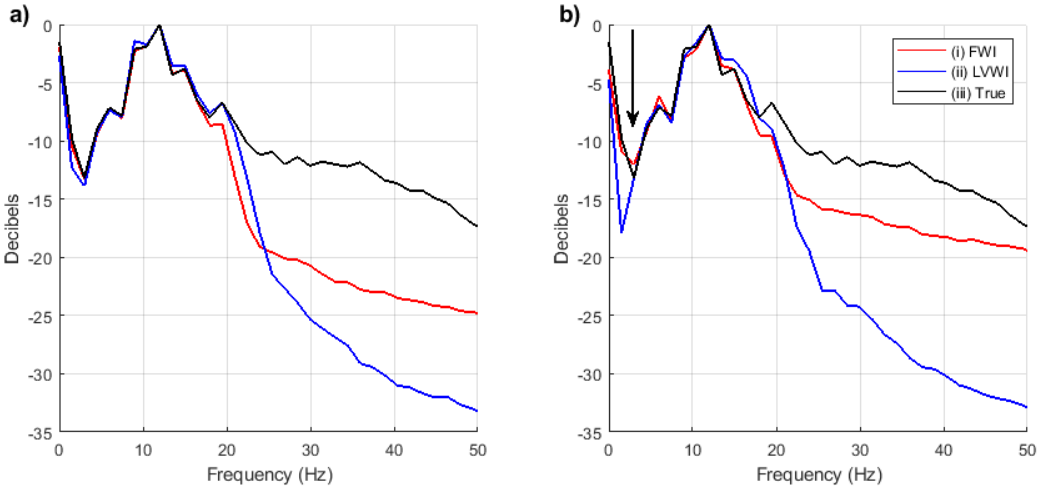

Figure 7.6: Amplitude spectrum of the inverted-model reflectivity when the initial model is (a) GS200 and (b) GS500 for (i) FWI workflow and (ii) log-validated waveform inversion workflow (LVWI). The black curve is the amplitude spectrum of the true model (iii).

the recovery of the long-wavelength information is subject to how deep the diving waves are able to travel.

RTM and PSPI update directions have pros and cons. The former has the capacity to retrieve long wavelengths from the first arrivals but is computationally expensive. The latter has a smaller computational burden but is more sensitive to the initial model. A combination of these two methods may exploit the advantages that they offer in the scenario of an

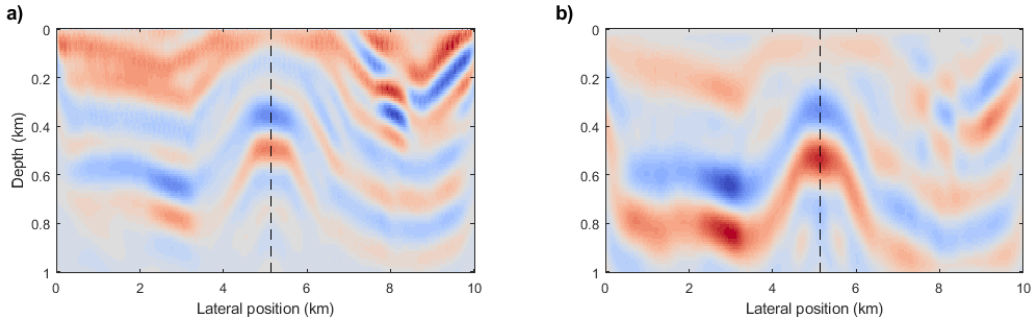

Figure 7.7: Update direction in the first iteration for (a) the conventional FWI and (b) log-validated waveform inversion using GS500 as the initial model.

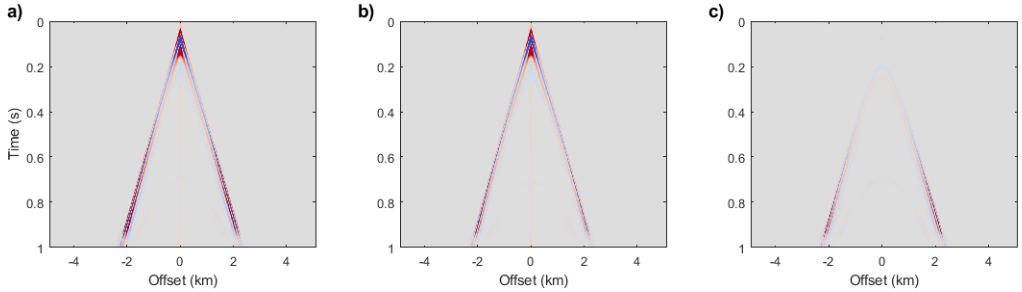

Figure 7.8: (a) Observed shot record through model GS200. (b) Modelled shot record through initial model GS500. (c) Data residual = (a) - (b).

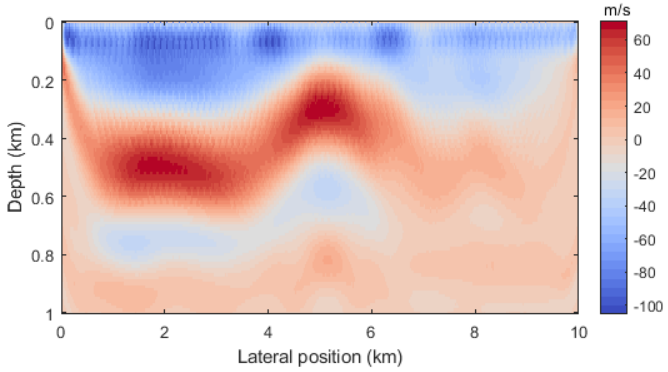

Figure 7.9: Velocity perturbation in the first iteration obtained by applying the conventional FWI workflow and by using model GS200 as true model and model GS500 as initial model.

inaccurate starting model. We could use the conventional FWI in the first iterations, when low frequencies are employed, in order to recover the long wavelengths, and then, we could switch to well-log validated waveform inversion when higher frequencies are incorporated.

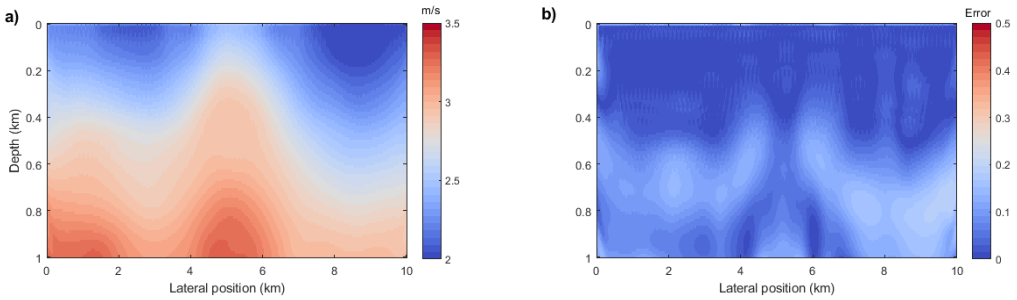

Figure 7.10: (a) Inverted model and (b) distribution of the error across the model after 5 iterations obtained by applying the conventional FWI workflow and by using model GS200 as true model and model GS500 as initial model.

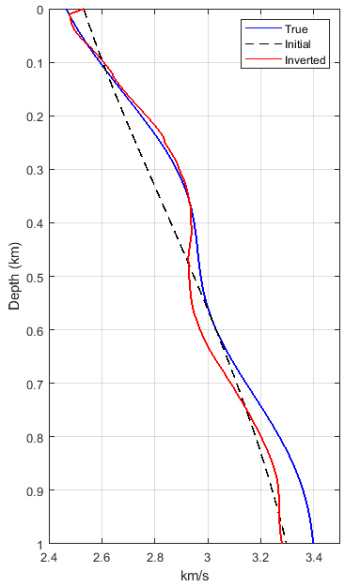

Figure 7.11: True, initial and inverted velocities at the location of the well obtained by applying the conventional FWI workflow and by using model GS200 as the true model and model GS500 as the initial model.

7.4 Conclusions

The initial model, one of the input variables in the waveform inversion process, has a significant impact on this local optimization problem. Its accuracy may determine the success or failure of the result. A good starting model is able to complement the lack of low frequencies in the seismic data, assisting to avoid cycle skipping and being trapped in a local minimum. I

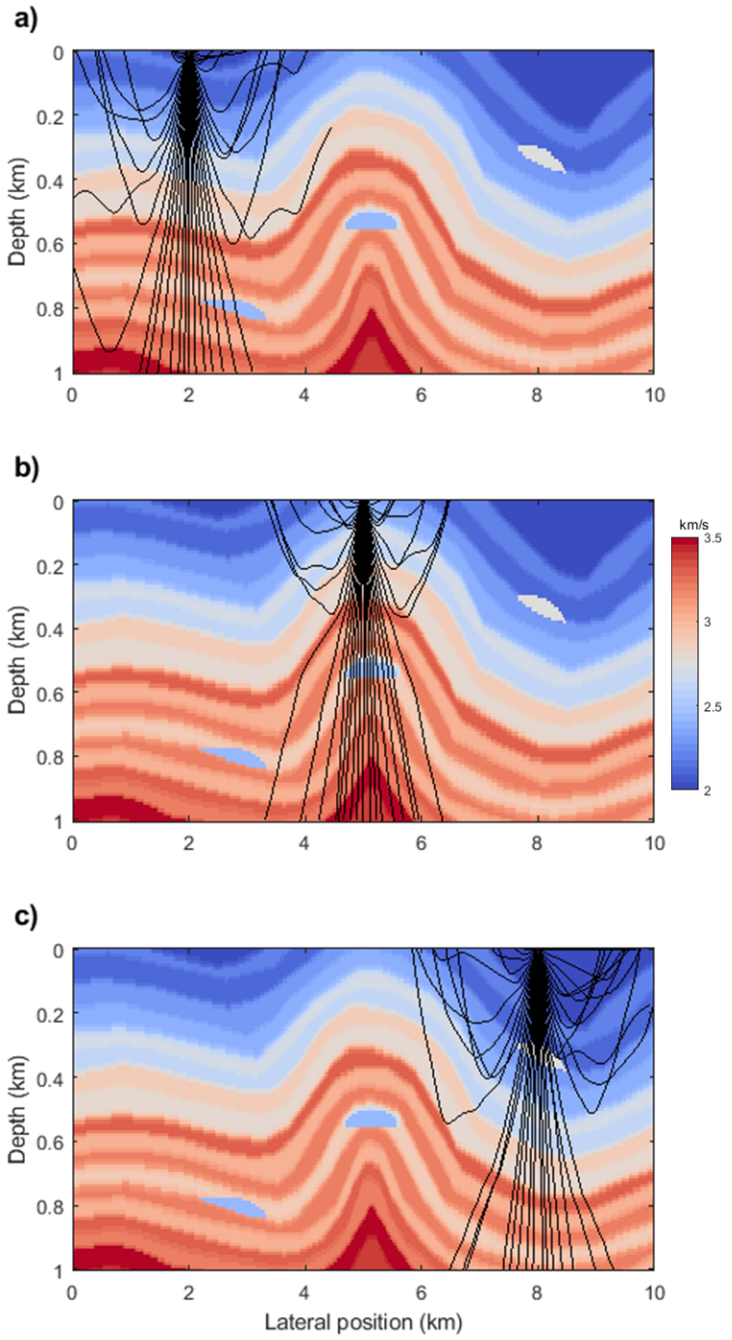

Figure 7.12: Ray tracing trough the anticline model for three different shots located at the lateral position of (a) 2km, (b) 5km and (c) 8km.

evaluated the sensitivity of two inversion methods to the initial model: the conventional FWI and the log-validated waveform inversion. The former produces the velocity perturbation via reverse time migration of the data residuals and data validation. The latter uses PSPI migration and impedance inversion to generate the update direction, and well-log validation to produce the velocity perturbation. A synthetic test showed that both methods converge into the true model when a sufficiently accurate starting model is employed. However, the use of a inaccurate initial model confirmed that the two methods are sensitive to a deficient initial model but in a different degree. The results suggest that the ability of RTM in managing diving waves represents an important advantage over PSPI when the initial model is deficient. RTM can better incorporate long wavelengths from the diving waves in the first stages of the inversion, where we are employing low frequencies under a multiscale approach. A synthetic example demonstrated that the source of the long wavelengths is the head and diving waves. Therefore, the recovery of low frequencies is limited to the depth penetration of these seismic waves.

Chapter 8

Well-log validated waveform inversion of reflection seismic data with wavelet phase and amplitude updating

8.1 Introduction

Full waveform inversion (Tarantola, 1984; Virieux and Operto, 2009) is now in regular, production-level use in industry and academia, with its impact in imaging of offshore reservoirs attracting particular notice (Minkoff and Symes, 1997; Shipp and Singh, 2002; Lee and Shin, 2015; Ray et al., 2016; Huang and Schuster, 2018). Its application onshore has undergone somewhat less of an explosion, through a range of compelling examples have been reported (Ravaut et al., 2004; Operto et al., 2004; Bleibinhaus et al., 2007; Brenders and Pratt, 2007; Gao et al., 2007; Jaiswal et al., 2008; Vigh et al., 2011; Malinowski et al., 2011; Plessix et al., 2012; Yu and Hanafy, 2014). There are several technical reasons for this slower uptake, important amongst which are (1) that land data is complex and poorly explained with simple (e.g., scalar acoustic) wave models; (2) that acquisition geometries are less regular; (3) that complex near-surface environments and source non-uniformity lead

to strong variability of the effective wavelet, which trades off with velocity errors; and (4) that long-offset data, important to the long-wavelength components of model updates, tend to be less commonly available. Economics also has an effect: in many onshore reservoir monitoring and exploration scenarios, the cost of a computationally demanding calculation, like FWI, is too large a fraction of the overall geophysics budget to be borne. The purpose of the research described in this Chapter is to formulate and examine waveform inversion procedures that address these issues, by taking advantage of auxiliary data that are often available in the same onshore environments.

Although they are less common than in marine settings, case examples of FWI applied to onshore data have been published. Common features of these reports are the importance of data pre-processing to accommodate amplitude variations not accurately modelled with simple wave physics, the benefits of the multi-scale approach to avoid cycle-skipping, and the requirement for some strategy concerning the wavelet. Ravaut et al. (2004) and Operto et al. (2004) applied traveltime and visco-acoustic waveform inversions to estimate the P-wave velocity from seismic data acquired in complex geological settings. The source wavelet in these cases was estimated following Pratt (1999). Other examples of combining traveltime and acoustic physics in land waveform inversion include those of Gao et al. (2007), who delineated a shallow paleochannel related to groundwater contamination, and Jaiswal et al. (2008), in a complex thrustbelt application. Brenders and Pratt (2007) demonstrated, in the context of a blind test, the efficacy of applying acoustic frequency domain waveform inversion to land data generated in a realistic, viscoelastic, crustal geology model. Bleibinhaus et al. (2007) applied frequency-domain acoustic-waveform inversion to the recovery of a velocity model above the San Andreas Fault, despite strong topography and near-surface geological variations. Vigh et al. (2011) applied time domain acoustic FWI to determine velocity models in both real marine and onshore settings, finding that these velocity models were able to provide uplift to the final images. Malinowski et al. (2011) also reported a land application of a visco-acoustic frequency domain FWI for velocity model recovery, as did Yu

and Hanafy (2014) in the inversion of early arrivals, including diving waves, for near-surface characterization of water storage. Plessix et al. (2010) and Plessix et al. (2012) focused on the importance of acquisition and pre-processing in land data before applying full-waveform inversion.

Margrave et al. (2010) set out a waveform inversion procedure called iterative modelling, migration, and imaging (IMMI), which emphasized precritical reflection data, and which made an effort to assign to each element of the standard FWI workflow an element of standard seismic processing. For instance, the gradient calculation was argued to be approximately replaceable with any convenient depth migration scheme, and the pseudo-Hessian (Shin et al., 2001b) was replaced with a deconvolution imaging condition, etc (see Chapter3). In substituting standard methodologies within the FWI loop, the incorporation of well-log information (a common step in impedance inversion) played a particularly important role (Chapter 4). A key element of IMMI was that rather than determining a scalar step-length with a line search (i.e., a data-validation approach), the scalar step-length was determined by minimizing the misfit with P-wave velocity log information. Margrave et al. (2010) examined the idea with synthetic examples, where the gradient was approximated using phase-shift plus interpolation or PSPI (Gazdag and Sguazzero, 1984). A major strength of using PSPI is the natural accommodation of frequency selection strategies in a multiscale approach (e.g., Pratt, 1999). This is because, unlike RTM, PSPI migrates each frequency independently and the cost is directly proportional to how many frequencies we migrate. Pan et al. (2014b) merged the IMMI approach with a phase-encoding technique.

Limiting the completeness with which waveform information is used, through the substitution of one-way wave operators, is a relatively drastic step, disqualifying these procedures from classification as true FWI algorithms. In fact, because of this move away from waveform inversion, quantities that play the role of FWI gradients are not gradients in the technical sense, so I will refer to them as *update directions*. Nonetheless, the combination of the computational savings brought about by this substitution, the stability conferred by the well-log

calibration, which requires no forward modelling steps, and the immediate use of near offset reflection energy is a strong motivation. It appears, as I will show in this Chapter, that the modelling error associated with a mono-parameter acoustic waveform inversion of land data, is sufficiently mitigated by stacking to produce interpretable models. Expanding to a pre-stack PSPI formulation of multi-parameter log-validated waveform inversion, and making use of the AVO information within the reflection data (Innanen, 2014), is a natural next step. However, in this Chapter, I focus on the leading order practical issues of (1) optimal processing, including transforming from reflectivity to impedance or velocity perturbations, time versus depth processing and (2) adjusting for wavelet error.

Wavelet error appears to be particularly important for the practical application of the well-log validated waveform inversion. Several approaches for coping with an unknown or difficult-to-estimate wavelet have been proposed. Lee and Kim (2003) set up an algorithm in which the source spectrum is eliminated through the construction of a normalized wavefield in the Fourier domain, resulting in a source-independent FWI. Liu et al. (2016) presented an approach in which observed shots were convolved with a reference trace from the modelled wavefield, and the modelled wavefield was convolved with a reference trace from the observed wavefield, to create meaningful residuals in the absence of a wavelet estimate. Both of these methods were reported as being affected by local minima and other convergence issues. These discussions are especially relevant to our current approach because they address wavelet errors with adjustments of the amplitudes and phases of the modelled seismograms to the observed seismograms. However, in these studies no updating of the wavelet was included. Another approach consists in treating wavelet parameters as a second set of unknowns alongside the medium property model, to be simultaneously determined (Pratt, 1999; Zhou et al., 1997; Wang et al., 2009). Our approach follows these latter formulations most closely.

The workflow for log-validated waveform inversion is the base on which the new workflow is founded. It includes an objective-function based decision to update the amplitude and

phase spectra of the modelling wavelet (criteria are given in detail in the next section). Synthetically, the approach is stable and in the presence of relatively strong wavelet errors, we recover models very similar to those recovered with a wavelet which is exactly known.

8.2 Workflow 1: Log-validated waveform inversion with one-way equation migration

In this section I recall the workflow for well-log validated waveform inversion set up in Chapter 4 (Figure 8.1). In contrast to many waveform methods, the data validation comes primarily from fitting of modelled and measured pre-critical reflections. The basic assumption is that the instabilities and local minima which attend such an inversion are avoided because of the presence of well-log data. To begin, I set out in a simple operator form the key calculations by which in standard seismic inversion (for details, see, e.g., Margrave et al., 2010, 2012a) velocity updates are extracted from residuals in the approach. We have, firstly,

$$\Delta \mathbf{v}_k = \lambda * \mathrm{Imp}\left(\Delta \mathbf{R}\right), \tag{8.1}$$

where constant density medium has been assumed, $\Delta \mathbf{v}_k$ is the velocity perturbation vector for iteration k, λ is a matched filter obtained with well-log control that calibrates the update or in the simplest case λ degenerates to a scalar, $*$ stands for convolution, and $\mathrm{Imp}(\cdot)$ is an impedance inversion operator acting on the reflectivity residual vector $\Delta \mathbf{R}$ that produces the raw update direction $\mathbf{\Phi}_k$:

$$\mathbf{\Phi}_k = \mathrm{Imp}\left(\Delta \mathbf{R}\right), \tag{8.2}$$

The reflectivity residual is obtained via:

$$\Delta \mathbf{R} = \mathrm{Stk}\big[\mathrm{Mig}\left(\Delta \mathbf{p}\right)\big], \tag{8.3}$$

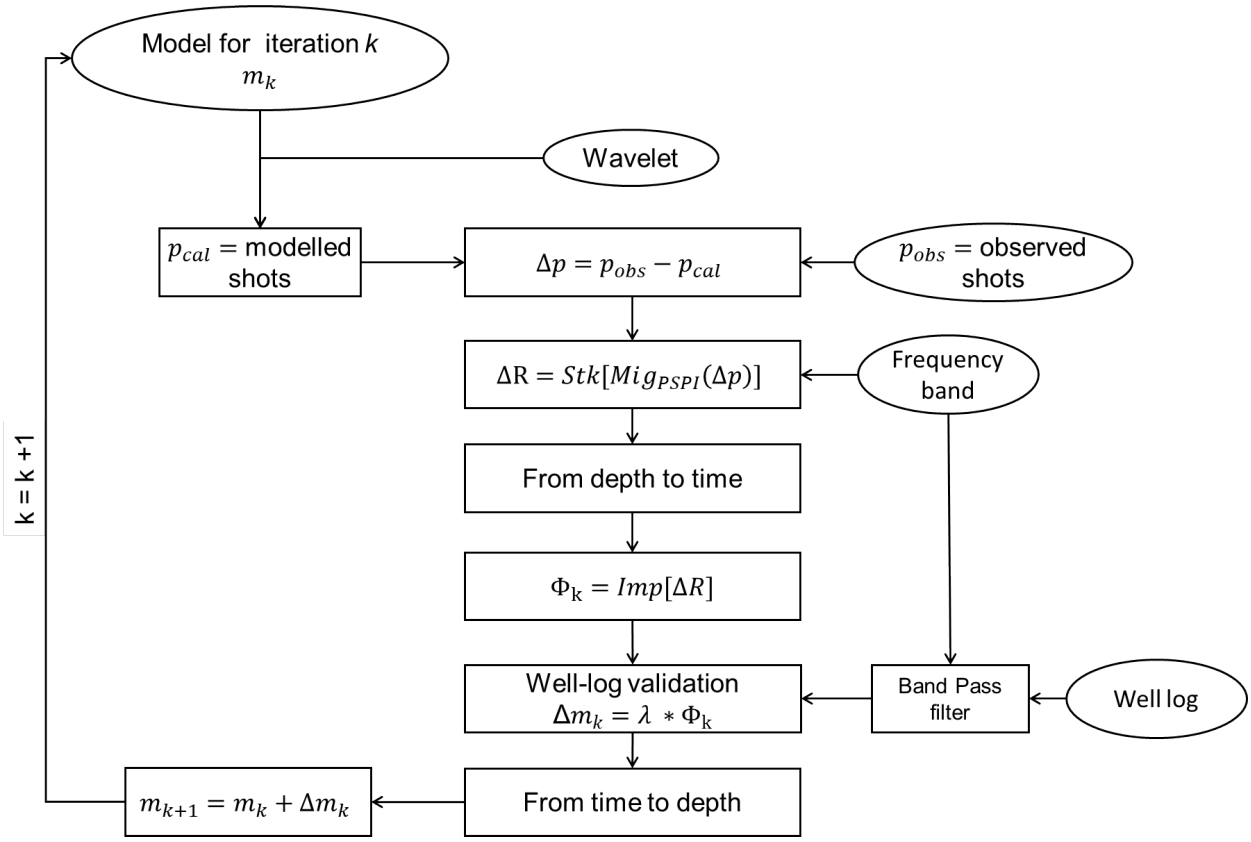

Figure 8.1: Workflow for well-log validated waveform inversion with update direction computed through PSPI depth migration.

where Mig$(\cdot)$ is the migration operator, Stk$[\cdot]$ is the operator that stacks the migrated data residuals, $(\Delta\mathbf{p})$ is the difference between observed shot record data $\mathbf{p}_{obs}$ and modelled shot record data $\mathbf{p}_{cal}$. The residual vector can be expressed in either time or depth coordinates, as needed, with the latter produced using the velocity model in the current iteration. Generally, the migration operator produces output in depth, whereas the impedance inversion of the reflectivity can occur in either depth or time (Chopra, 2016). However, our experience was that the impedance inversion was more stable and produced better results when applied in the frequency domain, especially in the presence of noise.

The numerical behavior of workflow 1 was examined with a synthetic example involving a moderate degree of lateral variability. In all algorithms, both explicitly in the simulation and implicitly within the migration step, a 2D medium governed by the constant density

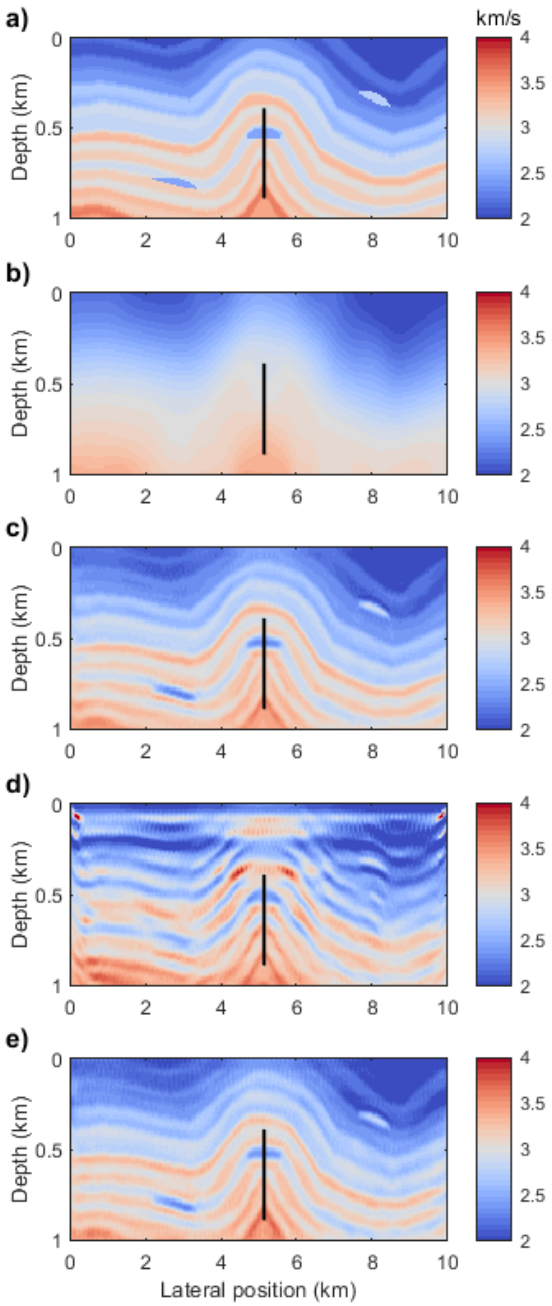

Figure 8.2: (a) Synthetic velocity model with weak lateral variations. (b) Initial velocity model. (c) Result from log-validated waveform-inversion workflow 1 (see Figure 8.1) with accurate input wavelet (i.e., solid black curve in Figure 8.3). (d) Result from log-validated waveform-inversion workflow 1 with wrong estimated wavelet (i.e., dashed curve in Figure 8.3). (e) Inverted velocity model using the wrong estimated wavelet and applying the phase and amplitude updating workflow (Figure 8.6).

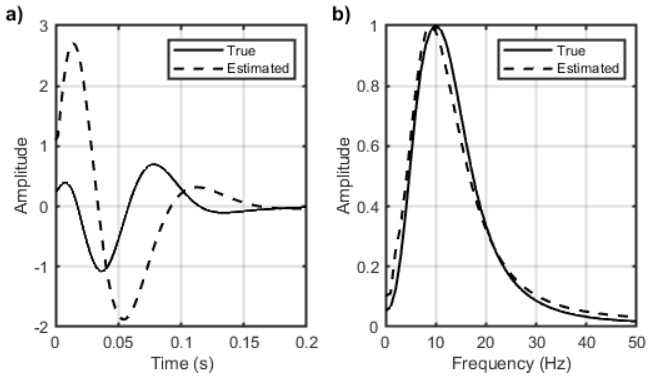

Figure 8.3: (a) Actual and estimated (minimum phase) wavelet. The latter was obtained by fitting the amplitude spectrum of the observed seismic data and assuming a minimum phase wavelet. (b) Amplitude spectra for actual and estimated wavelets.

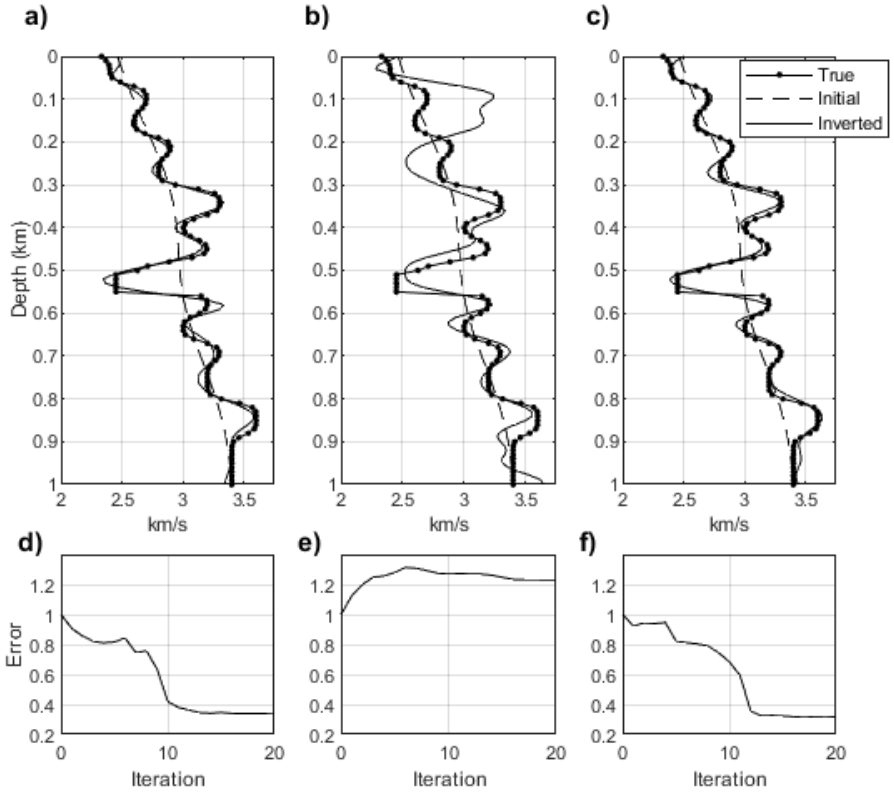

Figure 8.4: Inversion profiles at the calibration well location. (a) Log-validated waveform inversion workflow 1 (Figure 8.1), carried out with exact prior knowledge of the source wavelet; (b) workflow 1 using the estimated minimum phase wavelet (Figure 8.3); (c) Workflow 2 involving phase and amplitude correction and wavelet updating (Figure 8.6). (d) Normalized velocity error versus iteration for case (a). (e) Velocity error versus iteration for case (b). (f) Velocity error versus iteration for case (c).

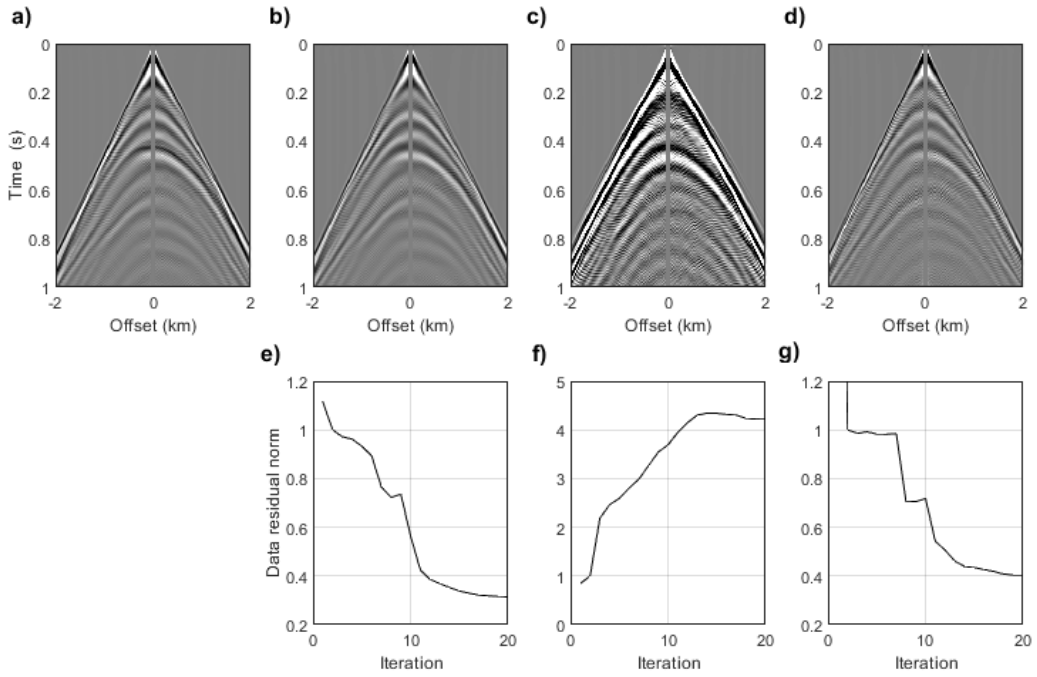

Figure 8.5: Synthetic observed and modelled data record examples after 20 iterations. (a) Observed shot record. (b) Modelled shot record produced by applying log-validated waveform inversion via workflow 1 (Figure 8.1) and by employing actual wavelet. (c) Modelled shot record produced by using the estimated wrong wavelet (Figure 8.3) with workflow 1, with no wavelet correction. (d) Modelled shot record obtained by using the estimated wrong wavelet and applying workflow 2, with phase and amplitude updating (Figure 8.6). (e) Data residual norm for case (b). (f) Data residual norm for case (c). (g) Data residual norm for case (d).

acoustic wave equation is assumed to hold. All simulations were carried out with a fourth-order finite difference scalar acoustic algorithm. The process is summarized next: The inputs are the initial velocity model, an estimated wavelet (which is not updated in workflow 1), the recorded data, and a P-wave velocity well log. First, synthetic shot records are generated by propagating the source wavelet through the initial velocity model, and data residuals are formed. Second, the residual gathers are depth-migrated and stacked, producing the reflectivity residual. PSPI is very convenient for a multiscale approach because it allows selecting the frequency band that we want to migrate. Third, the reflectivity residual is transformed into a raw update direction by changing coordinates from depth to time and applying the frequency domain impedance inversion algorithm. The assumption of constant density leads to an update in velocity units. Fourth, the well-log information is used to estimate an amplitude scalar and a phase rotation which optimally, in the least-squares sense, transforms the update direction at the well into a velocity perturbation. The well-calibration can be applied in either the time or depth domains. Since we are already in the time domain after the impedance inversion, we convert the velocity log from depth to time (using the velocity model), apply a band-pass filter which makes the raw update and the log comparable, and proceed to the estimation of the matched filter λ. The resulting matched filter is applied to the raw update throughout the model in order to obtain the final velocity update for that iteration. Fifth, the velocity update is stretched to depth and added to the current model. This new model is then used in the next iteration.

The model, illustrated in Figure 8.2a, was chosen to be a shallow anticline containing a low-velocity reservoir surrounded by relatively high-velocity rock. Two features were added to test the ability of the workflow to resolve stratigraphic features: a low-velocity trap was placed at 800m depth on the left-hand side of the model, and a high-velocity body was positioned at 300m depth near the right-hand edge of the model. Synthetic shot records were generated from 83 surface sources, positioned at 120m intervals and recorded by receivers across the surface at intervals of 10m. The initial model was generated by applying a

Gaussian smoother with a half-width of 200m to the true model (Figure 8.2b). A calibration well, labelled C, was positioned at roughly the center of the model. The well log was assumed to provide exact velocity information over a depth interval of 400-900m. The source was a minimum-phase wavelet, with a dominant frequency of 10Hz, rotated by a constant phase of 90° (Figure 8.3a-b, solid black curve).

The inversion was carried out using a multi-scale approach. The starting migration frequency band was 1-6Hz; this was increased by 1Hz at each iteration. The inverted velocity model produced by workflow 1 after 20 iterations is plotted in Figure 8.2c. The inversion result at the calibration well and its corresponding error are plotted in Figures 8.4a and 8.4d. Observed shot records, and modelled shot records after 20 iterations, are plotted in Figures 8.5a and 8.5b. The 2-norm of the data residuals is plotted as a function of iteration numbers in Figure 8.5e. In spite of the absence of a line search, we observe stable convergence both at the calibration well and throughout the model (via the norm of the data residuals). I conclude that in a simple synthetic environment, the presence of well-log information stabilizes waveform updates based on band-limited, relatively near offset reflection energy.

However, by introducing some uncertainty concerning the wavelet, even in a relatively simple synthetic environment such as this, the stability is quickly lost. We observed this by re-running workflow 1, keeping all things equal, except removing the wavelet as a known quantity. Instead, I applied a wavelet estimation approach to the data, fitting the amplitude spectrum determined directly from the synthetic data, and assuming that the associated wavelet is minimum phase. This estimated wavelet is plotted as a dashed line in Figure 8.3. The log-validated inversion workflow was re-applied; the result after 20 iterations is plotted in Figure 8.2d. A strong source footprint now dominates in the shallow zone. The inverted velocities tend to be significantly over- and under-estimated across the full breadth and depth of the model. The low-velocity reservoir at the left of the model is not identifiable; the other isolated bodies are just barely distinguishable from the surrounding medium. The inverted velocity at the calibration well and its corresponding error are plotted in Figure 8.4b and

8.4e, respectively. A modelled shot record after 20 iterations and the corresponding data residual norms are displayed in Figure 8.5c and 8.5f, respectively. The relatively stable decrease in model error has been replaced with error growth. I conclude that, even with the stabilizing presence of well-log validation, large and disruptive velocity model variations are introduced to account for wavelet mismatch in the residuals.

8.3 Workflow 2: wavelet phase and amplitude updating

Wavelet estimates used in typical seismic inversions are rarely accurate approximations of the actual seismic source. In waveform inversion methods, deviations between actual and estimated wavelets tend to leak uncontrollably into the velocity updating, causing tradeoff phenomena and impeding convergence. As we have now seen, a waveform method stabilized by model validation with well-log control is not particularly robust to such wavelet errors. In order to address this problem, I set up a wavelet updating methodology, which fits into a second workflow involving the separate migration and stacking of the observed and modelled shot records. The fact that we are updating with raw update directions computed with PSPI depth migration operators, as opposed to RTM operators, which decreases the computational cost significantly, makes this step feasible.

Workflow 2, set out in Figure 8.6, is based on a re-expression of the reflectivity residual used in workflow 1, i.e., equation 8.3. We write

$$\begin{aligned}\Delta\mathbf{R}^{(z)} &= \mathrm{Stk}\big[\mathrm{Mig}\left(\Delta\mathbf{p}\right)\big] \\ &= \mathrm{Stk}\big[\mathrm{Mig}\left(\mathbf{p}_{obs}\right)\big] - \mathrm{Stk}\big[\mathrm{Mig}\left(\mathbf{p}_{cal}\right)\big] \\ &= \mathbf{R}^{(z)}_{obs} - \mathbf{R}^{(z)}_{cal},\end{aligned} \tag{8.4}$$

where I have added the label $\cdot^{(z)}$ to make explicit the fact that the reflectivity is in the depth

domain, and where $\mathbf{R}_{obs}^{(z)}$ and $\mathbf{R}_{cal}^{(z)}$ are vectors of reflectivity data produced by migrating and stacking the observed and modelled shots, respectively. The motivation for separating the migration of the observed and modelled data is that it allows us to extract information about the wavelet by comparing these two datasets. However, the comparison must occur in the time domain for this information to be useful, so, a conversion from depth to time $\mathbf{R}_{(\cdot)}^{(z)} \rightarrow \mathbf{R}_{(\cdot)}^{(t)}$ is carried out using the current velocity model. These time reflectivity datasets can then be used to construct a cost function

$$\epsilon_R = \sum_t ||\mathbf{R}_{obs}^{(t)} - \mathbf{R}_{cal}^{(t)}(\phi, A)||_2^2, \tag{8.5}$$

which is analyzed to determine the suitability of the amplitude A and phase ϕ of the current wavelet estimate. This scheme is a vastly simplified form of wavelet estimation as used for well-tying, which assumes the initial wavelet to be stationary and correct except for a rescaling and a constant phase rotation. Empirically, i.e., through synthetic testing, one of two distinct cases appears to reliably occur with respect to ϵ_R:

1. It may have a well-defined minimum and be straightforward to minimize, in order to determine amplitude A and phase ϕ matching the stacked data, or

2. It may be poorly behaved, with either a weak or non-existent minimum, with optimal A and ϕ defaulting to values on one of the boundaries in their allowable ranges.

Through numerical testing, we observe that case (2) occurs when no significant improvement in the amplitude and phase of the current wavelet can be found within the current frequency band. In light of this, I include logic in the workflow such that, if case (2) occurs, no wavelet updating is carried out ($A = 1$ and $\phi = 0$), and the frequency band is extended. This logic appears in box A (Figure 8.6). In the new workflow, whenever case (1) occurs, the synthetic time reflectivity is updated and, according to the logic in the vicinity of box B in Figure 8.6, if the scalar factor and phase rotation minimize the data residuals, the wavelet is updated

and the frequency band is maintained for the next iteration. If condition B is not met, the wavelet is not changed and the frequency band is extended for the next iteration.

After evaluating the scalar and phase rotation within box A (Figure 8.6), we end up with a synthetic reflectivity that is combined with the observed time reflectivity to create the wavelet-updated residuals

$$\delta\mathbf{R}^{(t)} = \mathbf{R}^{(t)}_{obs} - \mathbf{R}^{(t)}_{cal}. \tag{8.6}$$

This is input into the construction of the raw update direction, as before, through an impedance inversion:

$$\mathbf{\Phi}^{(t)} = \mathrm{Imp}\left(\Delta\mathbf{R}^{(t)}\right). \tag{8.7}$$

The quantity $\mathbf{\Phi}^{(t)}$ is then calibrated with well-log information, mapped onto the depth coordinate axis, and used to produce the velocity perturbation.

Workflow 2 was tested by applying it to the same data set used to examine workflow 1, within which the actual wavelet was unknown and the initial wavelet was estimated from the seismic data. The inverted velocity model after 20 iterations is plotted in Figure 8.2e. The inversion at the calibration well and its corresponding error are plotted in Figure 8.4c and 8.4f, respectively. The modelled shot after 20 iterations and the data residual norms are displayed in Figure 8.5d and 8.5g, respectively. We observe a return to the stability and resolution of the workflow 1 inversion results recovered when the wavelet was known a priori. We also note that the error at the calibration well tends to decrease as the wavelet undergoes corrections. The decay of the norm of the data residuals is also seen to be once again similar to that of workflow 1 with a known wavelet.

In Figure 8.7 the evolution of the wavelet during the well-log validated waveform inversion iterations is plotted. We see punctuated updating: the wavelet only changes at iterations 1, 8, and 11 when the phase and amplitude updates minimize the data residuals. Even though the wavelet is being only updated in some iterations, the modelled reflectivity is continuously subjected to updates. This is shown in Figure 8.8, where the phase and amplitude updates

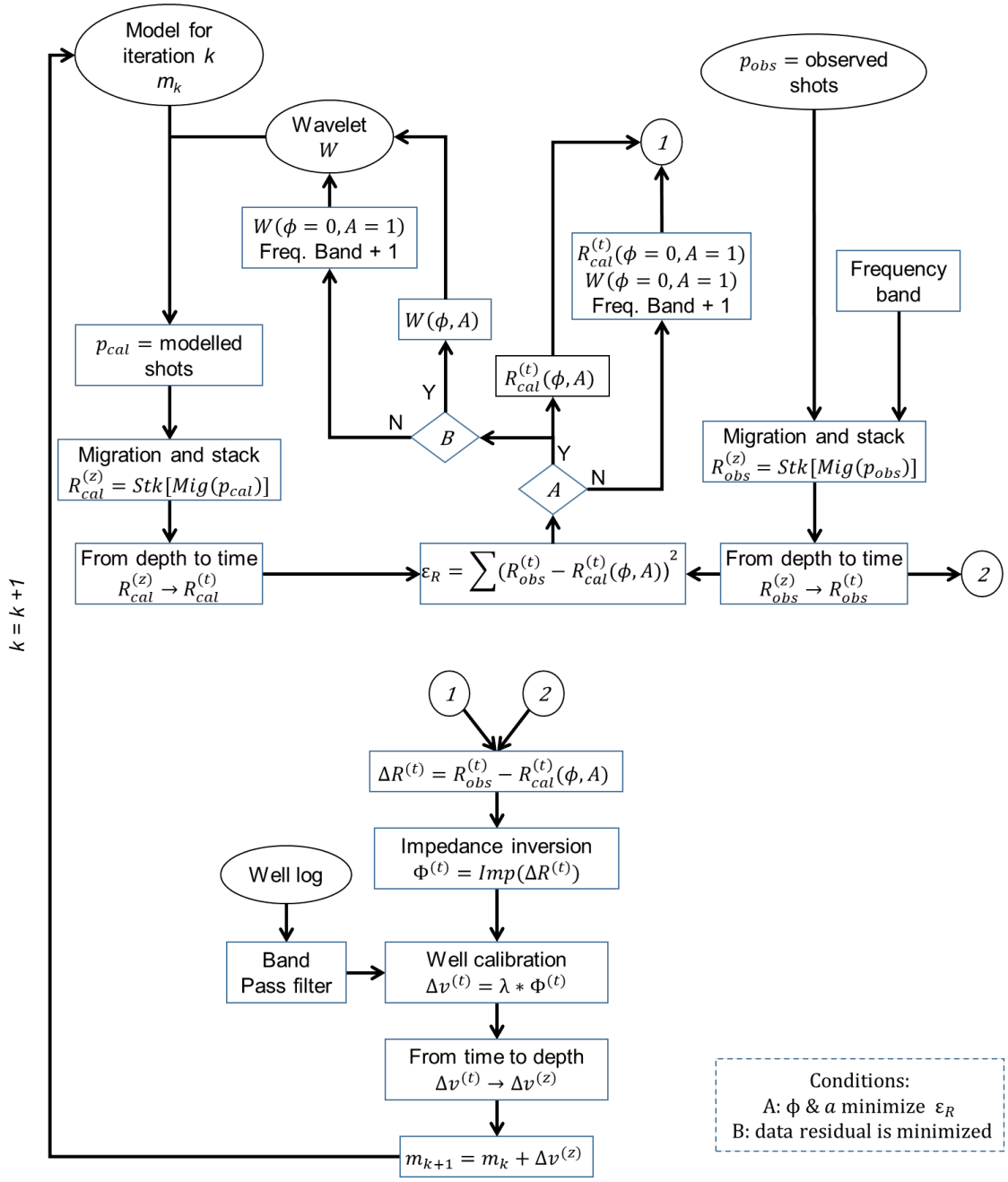

Figure 8.6: Workflow 2 for log-validated waveform inversion with update direction computed through PSPI depth migration, and with wavelet amplitude and phase updating.

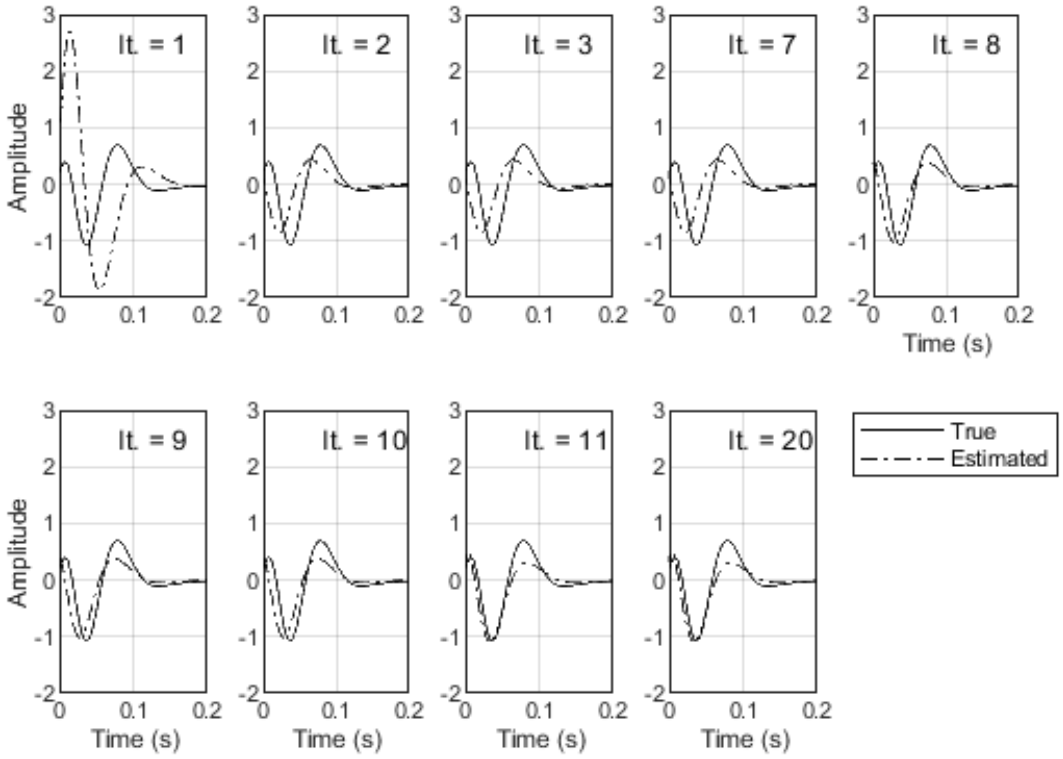

Figure 8.7: Wavelet phase and amplitude updating with iterations.

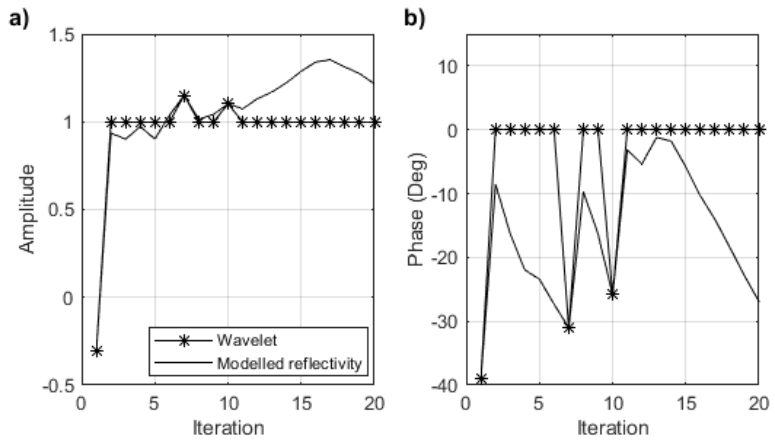

Figure 8.8: (a) Amplitude updates applied to the wavelet and modelled reflectivity. (b) Phase rotation updates applied to the wavelet and the modelled reflectivity.

for the modelled reflectivity and the wavelet are plotted.

8.4 Validation on the Hussar land dataset

In 2011 a 2D land data set was acquired near Hussar, Alberta to support waveform inversion research (Margrave et al., 2011a). The data were acquired with maximally broadband sources, including low-frequency and low-dwell (spend extra time in the low -frequency range (Margrave et al., 2012b)) Vibroseis sources and dynamite, which illuminated single and multi-component sensors with maximally broadband responses, including 10Hz and 4.5Hz geophones, and also accelerometers. The data have been processed and analyzed to determine their useable bandwidth (Isaac and Margrave, 2011), and have been used to support parameter resolution analyses of elastic full waveform inversion (Pan et al., 2018). The dataset, with its 3 well logs, which can be used partially to support the inversion and partially as ground truth, is ideal for testing the log-validated workflows.

The Hussar dataset consists of 257 source stations at approximately 20m intervals, and 448 receiver stations at 10m intervals, for a total array length of 4.47km. Although originally acquired with a variety of sources and receivers, in this study I used only the vertical

components of the accelerometer data, and roughly one-third of the 2kg dynamite sources, which were evenly separated at 60m and buried at a depth of 15m. P-wave velocity logs were available from three nearby wells. All receivers recorded each source point, leading to source gathers each containing 448 traces. In Figure 8.9 the 2D seismic line is illustrated, along with the positions of the 3 wells, 14-27, 01-34 and 14-35.

The initial processing of the Hussar data set (Isaac and Margrave, 2011) included radial filtering (Henley, 1999) to attenuate high-amplitude and low-frequency source generated noise, and Gabor deconvolution (Margrave et al., 2011c) to correct for non-stationary wavelet effects. The data were processed to a final datum of 985m. An example shot record is plotted in Figure 8.10a.

As additional data conditioning in preparation for the waveform inversion described in this Chapter, I also applied:

1. A low-pass filter with a cutoff of 65Hz;
2. An FK filtering process to suppress some remaining linear source noise,
3. A mute of the direct arrival in both the field data and the synthetic shot records.
4. An approximate amplitude correction (from three dimensions to two dimensions) that consists in employing a $\sqrt{t}$ filter as in Pratt (1999).

The same shot record after conditioning for waveform inversion is plotted in Figure 8.10b.

Well 14-35 was the main calibration well, i.e., it was used both to generate the initial model, plotted in Figure 8.11a, and to calibrate the raw update direction in the inversion process. Wells 01-34 and 14-27 were then free to act as blind wells for error analysis. In Figure 8.12a the starting wavelet, estimated by fitting the amplitude spectrum of the seismic data and assuming a minimum phase response, is plotted. The dominant frequency is roughly 20Hz (Figure 8.12b). Notice that well 01-34 is offset from the seismic line by roughly 450m. Through some trial and error, I found that the best match with the inverted velocity and

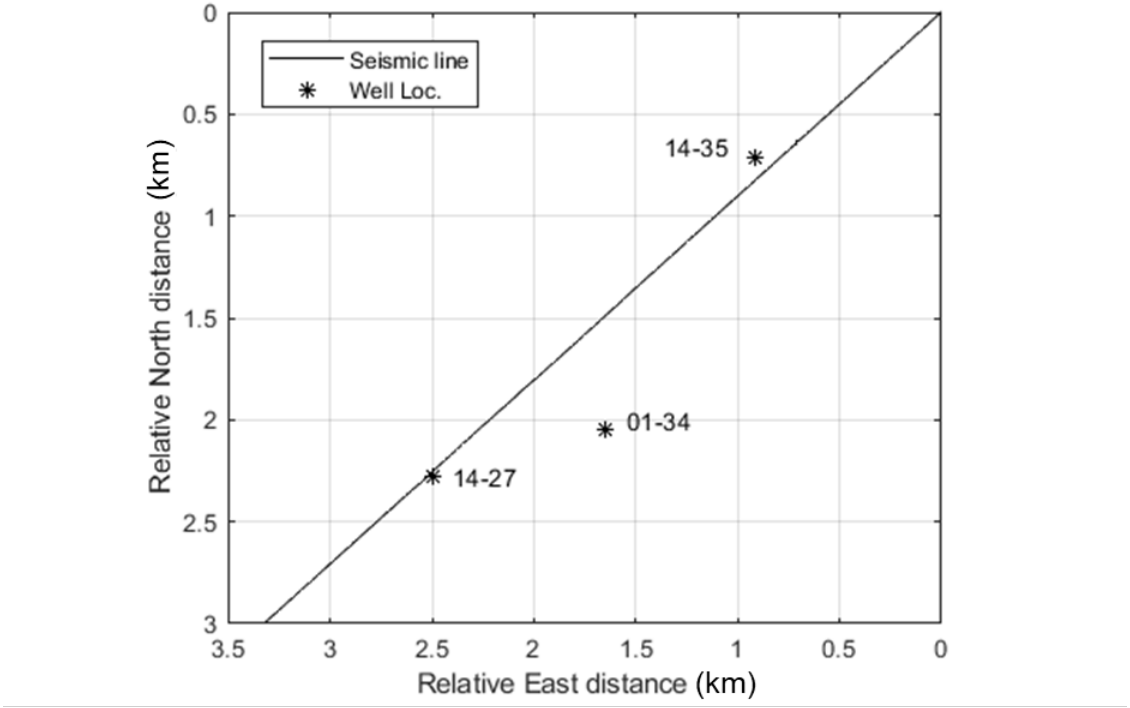

Figure 8.9: Map view of Hussar survey area, 2D seismic line, and wells 14-27, 01-34 and 14-35.

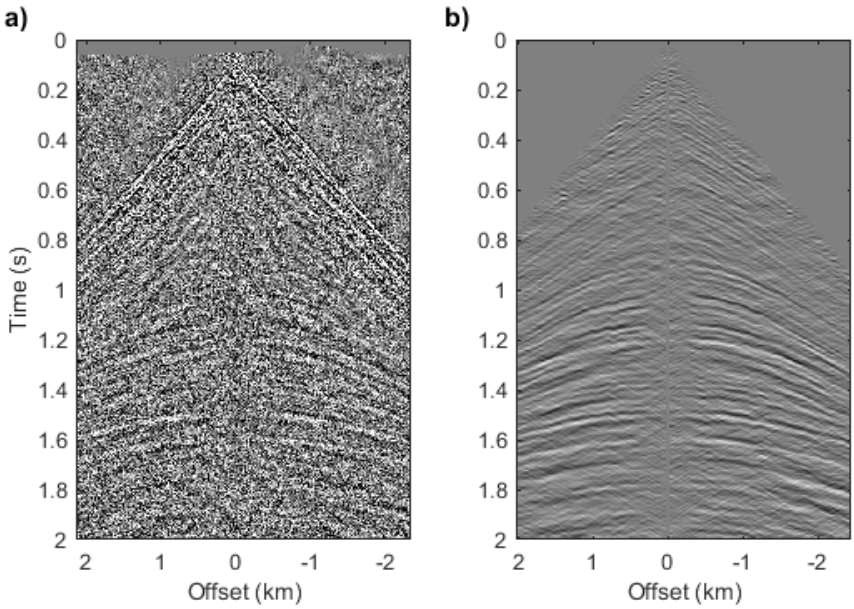

Figure 8.10: Hussar reflection seismic data example shot record, (a) before and (b) after processing and conditioning for waveform inversion testing.

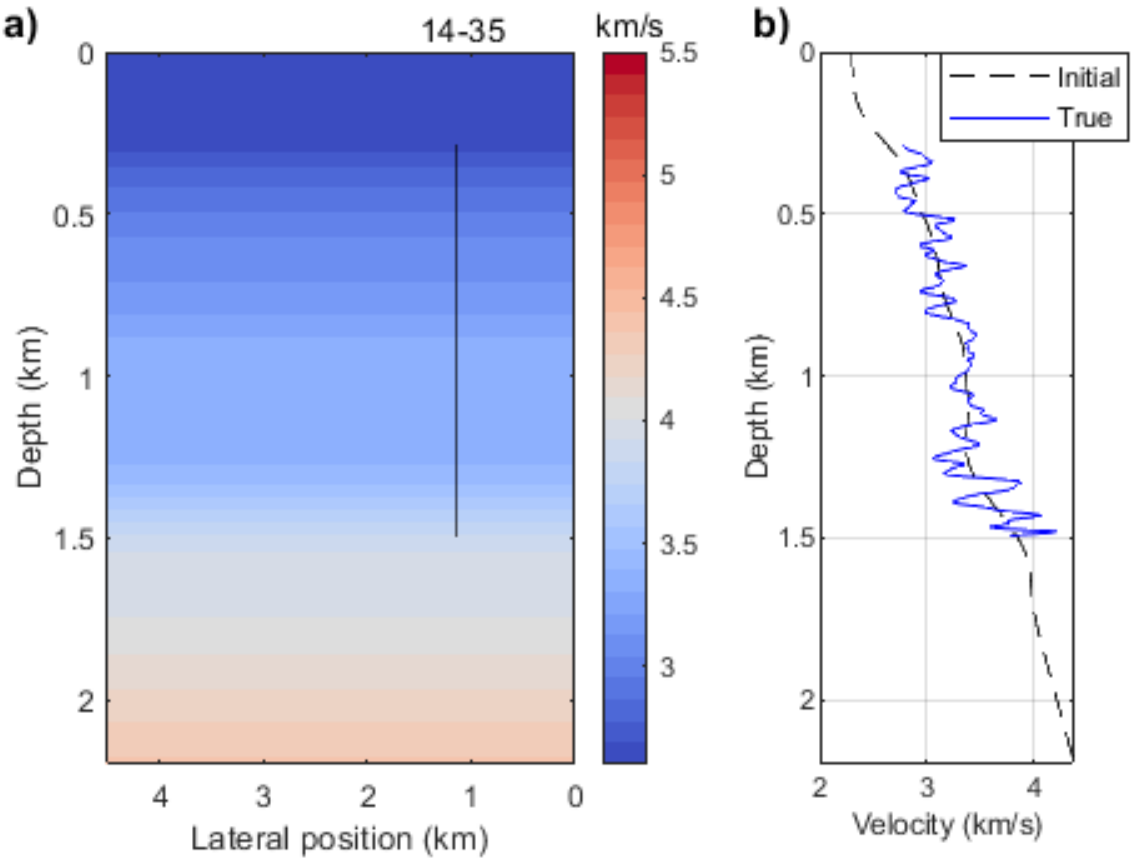

Figure 8.11: (a) Starting model for inversion of the Hussar data, with calibration well-log overlain (solid black line); (b) the initial velocity model profile (dashed line), which is a smoothed version of the velocity profile at well 14-35 (blue).

this well was obtained if the log was shifted upwards by 50m. This is consistent with the positioning of the well assuming that the layers dip at about 6°.

The inversion, like the synthetics of the previous section, was carried out using a multi-scale approach. The starting frequency band was 4-8Hz; it was moved up by 1Hz per iteration, subject to the wavelet correction logic discussed in the previous section (labelled condition B in the workflow in Figure 8.6).

In Figure 8.13 the output Hussar velocity model, determined using workflow 2, is plotted. Within the zone that generated significant seismic reflection events, at roughly 0.8s (approximately 1000m depth and below), the inverted velocity agrees well with the velocities in the blind and calibration wells (Figure 8.14). In the shallower zones where reflection

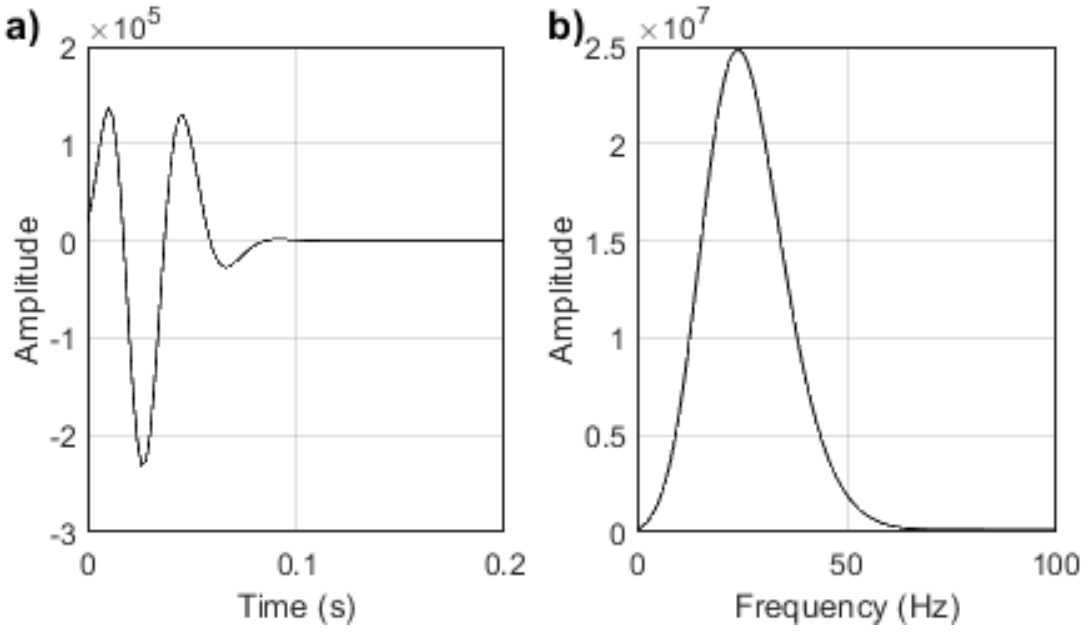

Figure 8.12: (a) Wavelet estimated from Hussar seismic data. (b) Amplitude spectrum.

energy is weaker, little in the way of useful structure is extracted. In Figure 8.15 example observed and modelled shot records, the latter after 60 iterations, are plotted alongside the data residual norm. We observe that, in contrast to the synthetics, the wavelet tends to continuously change as we iterate, as shown in Figure 8.16, indicating unsurprisingly that the data residual reduction was less regular in the field case than in the synthetics. That said, workflow 2 converged convincingly by iteration 40, and the final model contained well-resolved structural information results wherever reflection energy occurred in the data. The frequency band used in each iteration is plotted in Figure 8.17.

8.5 Discussion

The well-log validated waveform inversion workflows I present are stable, well-posed, and straight forward-to-apply given surface seismic data with significant reflection energy and low to moderate offsets. Its main positive features are that it directly addresses the primary issues facing reflection inversion: non-linearity and local minima are mitigated with well-

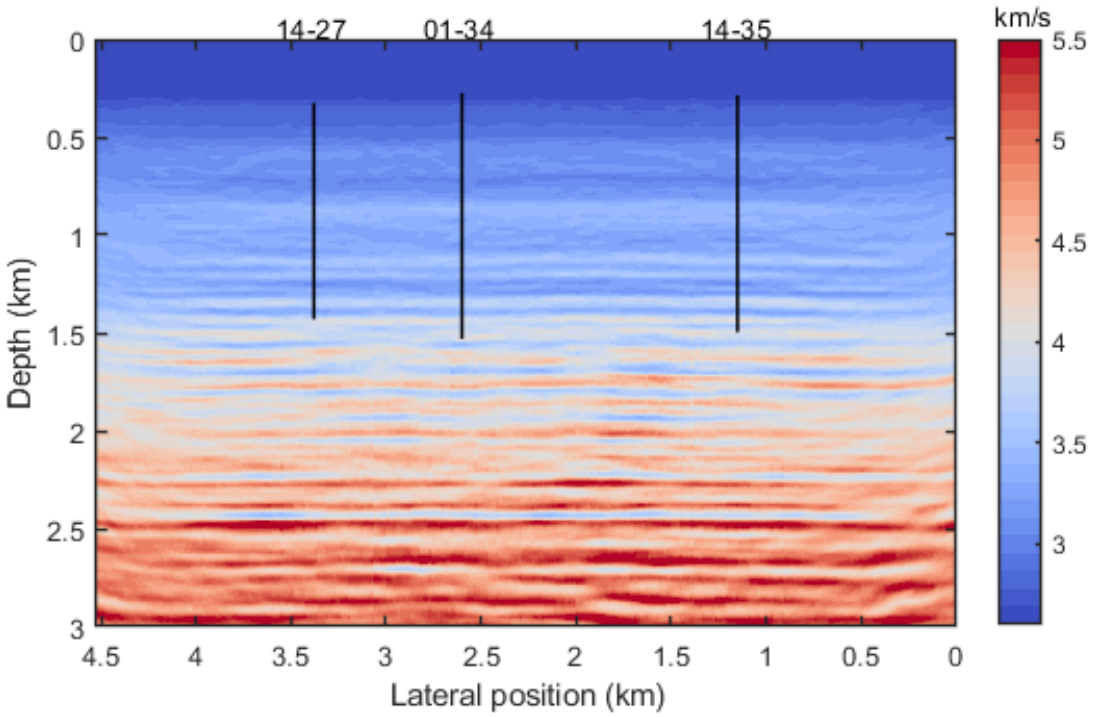

Figure 8.13: Inverted velocity model generated using log-validated waveform inversion workflow 2 with wavelet updating. Calibration well 14-35, and blind validation wells 01-34 and 14-27 are overlain (solid black).

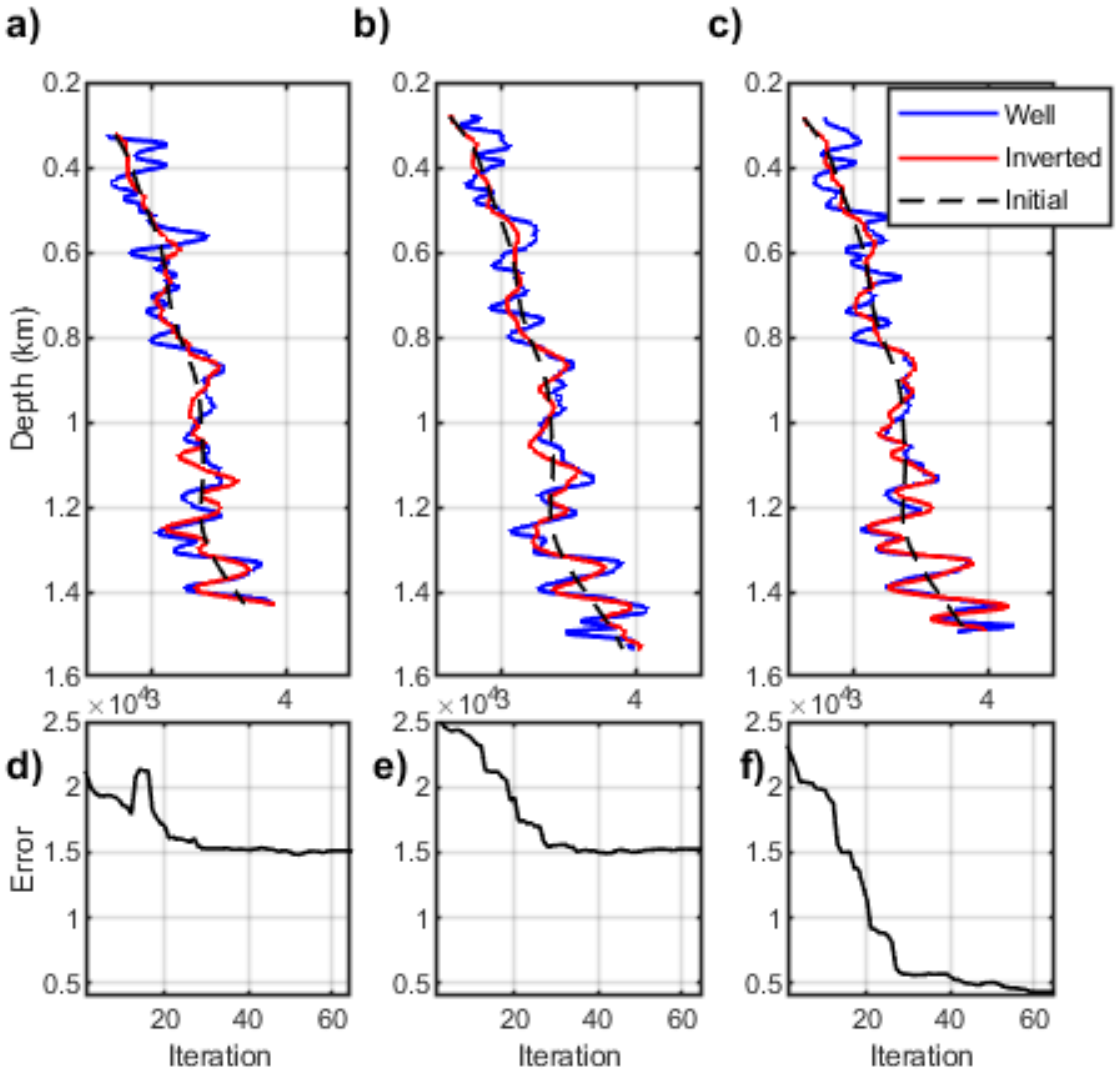

Figure 8.14: Inverted velocities and model errors at well locations. (a) Well 14-27; (b) well 01-34; (c) calibration well 14-35. Model error norm versus iteration number for (d) well 14-27; (e) well 01-34; (f) calibration well 14-35.

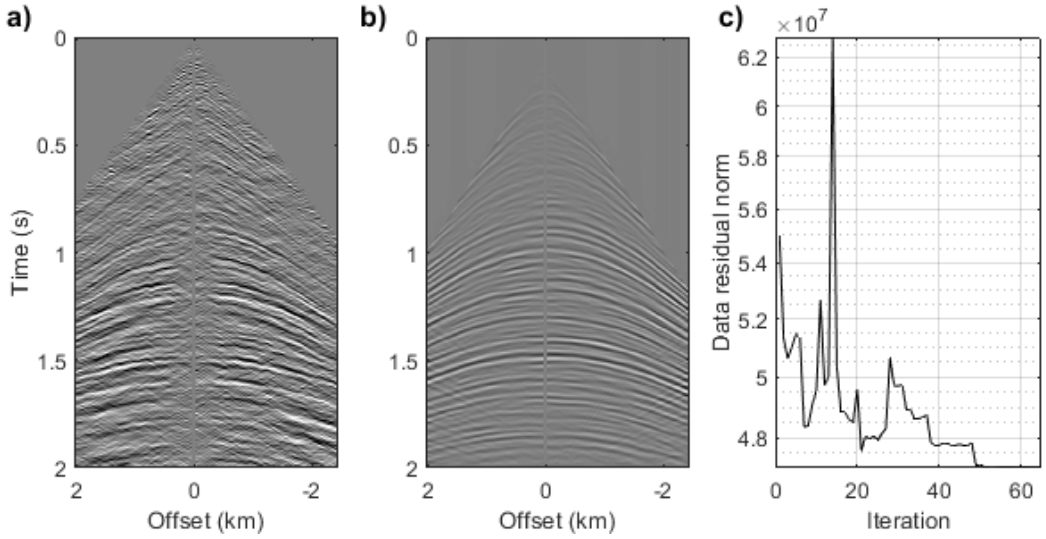

Figure 8.15: Modelled versus observed data during inversion. (a) Example of observed Hussar shot record; (b) modelled Hussar shot after 65 iterations; (c) Data residual norm versus iteration number. Well-log validation step permits data residuals to experience punctuated growth, but an overall stable decay is noted.

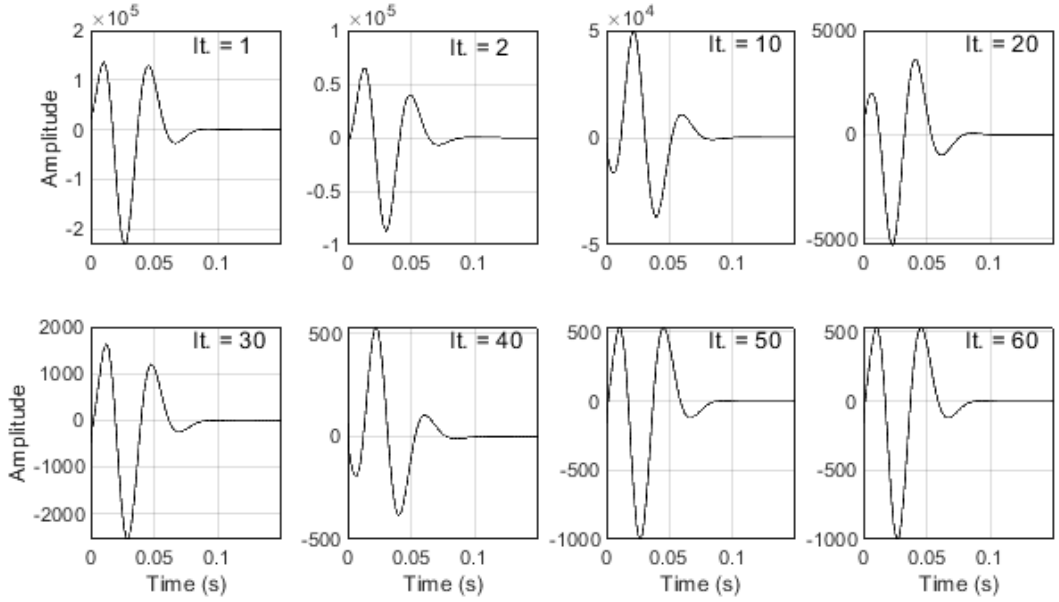

Figure 8.16: Evolution with iteration number of the estimated wavelet for the Hussar data.

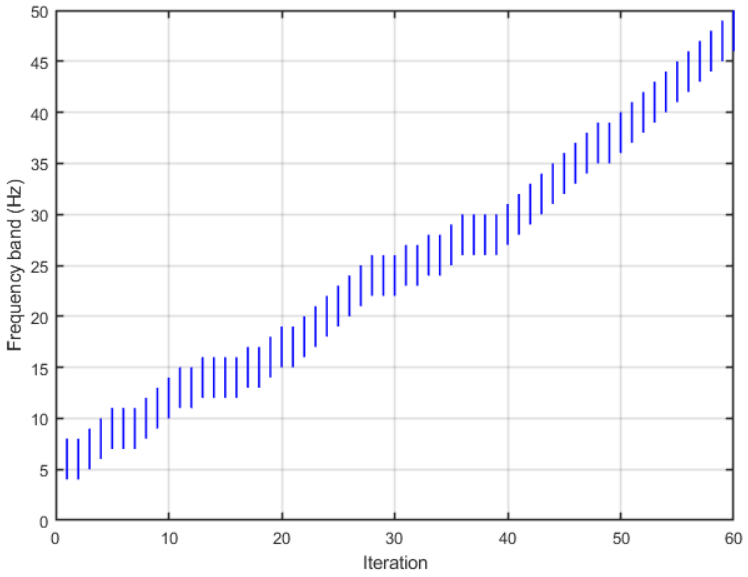

Figure 8.17: Frequency bands used in each iteration.

log validation, noise is mitigated with stacking, and wavelet cross-talk is mitigated with a phase and amplitude updating. The approach can be applied to field data with relatively low degrees of data preprocessing and conditioning, resulting in models that correlate well with blind well data in regions illuminated by seismic reflection energy. However, there are qualitative differences in the wavelet updating observed between the synthetic and field examples. In the synthetic case, the wavelet remained constant over significant iteration intervals, updating in a punctuated manner that it, in fact, helped to guide the timing of inclusion of new frequencies. In the field case, the conditions leading to a wavelet update tended to be met at almost every iteration. This is suggestive that under field conditions there exist interactions between the wavelet and the velocity errors beyond those which our approach accommodates. I conjecture that a lack of constancy in the phase of the field wavelet, which held in the synthetic example, is partially responsible for this. The next order of complication in wavelet updating will be to search for a frequency dependent phase. In workflow 2, any non-constant phase variability in the true wavelet would be construed as a reflectivity error. The non-stationarity of the wavelet is another factor that may affect

the wavelet updating. It is possible that changing the parameterization of the wavelet may better isolate source and velocity errors. This is a subject of ongoing research. In the meantime, the workflow we set out led to a continuously updating reflectivity, a relatively rapid convergence, and the recovery of structures which correlated with blind well data. For this reason, I consider that such an approach represents a useful way forward.

8.6 Conclusions

Building on the iterative modelling, migration and inversion concept of Margrave, I have formulated an approach to reflection seismic data inversion that involves the substitution of robust processing methodologies for several of the standard ingredients of FWI. A raw update direction is obtained by applying a one-way wave-equation migration (PSPI) to near and moderate offset reflection data, and an iterative updating is based on this quantity, built from a well-log calibration process (as opposed to a line search or other data-validation process) to produce the velocity perturbation. I found that, although it is generally stable, when exposed to errors in the initial wavelet estimation, synthetic and practical application of the formulation were badly exposed to wavelet/model cross-talk. To address this, I set up a log-validated waveform inversion workflow containing an extra internal loop, within which the phase and amplitude of the synthetic wavelet were given the opportunity to update prior to the velocity. In the workflow, the suitability of the current wavelet is judged by separately migrating and stacking the observed and modelled shot records, rather than processing their difference, to produce two reflectivity datasets. The observed and modelled reflectivities are expressed in time coordinates, where they are compared through a cost function that depends on the wavelet phase and amplitude. Instabilities easily produced in synthetic examples with wavelet errors are observed to vanish under this workflow. The workflow can be stably applied to field data, which I demonstrate with the CREWES Hussar 2D land data set. The stable, rapid convergence of both the recovered reflectivities and velocity models,

as well as the meaningful geological structures we obtain, are positive signs that the log-validated approach works. The detailed behavior of the wavelet updating in field application is different from that which we observed in the synthetics; I speculate that variants of the wavelet parameterization may be useful.

Chapter 9

Summary and conclusions

The well-log validated waveform inversion presented in this thesis has been demonstrated to provide reliable P-wave velocity models from reflection seismic shot records. LVWI is built on iterative modelling, migration and inversion, concept of Margrave. IMMI follows the basic full-waveform inversion workflow and aims to identify internal operations in FWI that can be replaced by standard processing techniques. In order to put LVWI into context, first I described the FWI framework and set up a four-step basic procedure: 1) modelling of synthetic shots and generation of data residuals, 2) reverse time migration of the data residuals to produce the gradient, 3) scaling the gradient to derive the model perturbation, and 4) updating the model. A synthetic example was used in order to demonstrate the validity of the procedure. The simulations were carried out with a fourth-order finite difference scalar acoustic algorithm and a 2D medium governed by the constant density acoustic wave equation was assumed to hold. In the migration step, a deconvolution imaging condition showed to compensate by the geometrical spreading, producing a similar effect than the diagonal elements of the pseudo-Hessian matrix. A multiscale approach was implemented, starting from a low-frequency band and introducing higher frequencies as we iterate. This technique produced a superior convergence to the model and the observed shots when compared to the option of migrating all frequencies in each iteration. In the scaling step, the Tarantola

and Pica's approach was compared to the backtracking and quadratic interpolation method. These methods are referred to as data validation procedures since they are built to minimize the data residuals. Both techniques produced similar step-lengths; however, the former has a smaller computational burden because it only needs one forward modelling to find the scalar. The FWI workflow was taken as the base on which the log-validated waveform inversion was developed from Chapter 3. Having recognized that the gradient in FWI can be obtained by the reverse time migration of the data residuals, it is argued that any depth migration method would be able to derive the update direction. This reasoning was put to test by implementing a one-way wave equation migration with a deconvolution imaging condition. The comparison between the RTM and the PSPI update directions brought to light that the PSPI update direction has a phase shift, which may limit its application in the waveform inversion process. Since PSPI migration with a deconvolution imaging condition generates reflectivity, it follows that the impedance inversion will lead to an impedance update, which is a velocity update in the constant density approximation. A similar result can be obtained by employing a time-integrated wavelet to generate the source wavefield, which allows avoiding the impedance inversion step. I adopted the impedance inversion approach in this research, assuming that the migrated stack approximates to normal-incidence reflectivity. The implications of this assumption (angle-dependent reflectivity and horizontal layers) were discussed in Chapter 3. The impedance inversion partially corrects the PSPI-update direction phase allowing to derive the velocity perturbation by applying a data validation procedure. A frequency-domain impedance inversion was adopted because it showed to be more stable in the presence of random noise than the time or depth domain options. In Chapter 4, I introduced the well-log validation procedure that converts the update direction into a velocity perturbation. This technique overcomes the remnant phase shift in the PSPI update direction and reduces the computational time because it does not need any forward modelling in the scaling step. Well-log validation consists in computing a matched filter that minimizes the difference between the update direction and the velocity residual at the well

location. A relevant finding, within synthetic examples, is that well-log validation tends to reduce the data residual norms, even though it is not set up to explicitly minimize them. The inversion procedure that incorporates a PSPI update direction and well-log validation is referred to as well-log validated waveform inversion (LVWI). The sensitivity of LVWI to a range of adverse conditions related to the well-log information was evaluated in Chapter 5. Numerical tests indicate that increasing geological complexity degrades the effectiveness of the log-validated waveform inversion, resulting in smoother models when inverting very complex models. In a second test, I observed variation in the matched filter required to produce the exact velocity perturbation away from that produced in the vicinity of the lateral position of the well, further quantifying the issue of lateral variation and structural complexity. However, the final inverted models for three different well locations turned out to be very similar, which suggests that log-validated inversion under this factor has remarkably little sensitivity. I noted that the best result came from a well that through some averaging process represents the velocity across the model. I also tried a matched filter computed by simultaneously using three well-logs at different locations; this scenario produced an average result when compared to the inversion obtained with the three wells, separately. In another test, I evaluated the impact of the log interval in the inversion. The best performance was obtained when the log interval is equal to or greater than 1.5 times the average wavelength determined for the first iteration. In a final test, the effect of moderate and strong amount of random noise to the log was investigated. It was noted that random noise may limit the calibration capability of log validation, especially when high frequencies are introduced in a multiscale approach. The sensitivity of well-log validated waveform inversion to the survey acquisition parameters was investigated in Chapter 6. The tests included varying the receiver interval (RI), source interval (SI) and maximum offset (MO). The receiver interval controls the bin size and impacts the trace distribution. A small RI contributes to the horizon continuity. The inversion is relatively insensitive to this parameter, if it is selected following the design recommendations. The source interval has the potential to damage the inversion

result especially in the shallow zone of the model because it controls how the horizons close to the surface are mapped. The inversion result is very sensitive to a large source interval because it is exposed to a strong acquisition footprint. Furthermore, the mute before stacking the migrated data residual has little influence for small source intervals, but it has to be properly selected when using large source intervals. The maximum offset not only contributes to imaging the steepest horizons but also incorporates long-wavelength information from long-offset traces that contributes to the construction of the model in the shallow zone. In a final test, it was found that a robust acquisition with high trace density reduces the negative effect of random noise in the seismic shots. The sensitivity of the waveform inversion to the initial model was analyzed in Chapter 7. The initial model is an important input that may determine the success or failure in the inversion process. A good starting model is able to complement the lack of low frequencies in the seismic data, assisting to avoid cycle skipping and being trapped in a local minimum. Synthetic tests showed that conventional FWI and log-validated waveform inversion are able to converge to the true model when a sufficiently accurate starting model is employed. However, both methods are sensitive, in a different degree, to a deficient initial model. RTM, in conventional FWI, is capable of better incorporating long-wavelengths in the first stages of the inversion, where low frequencies are employed in the multiscale approach. In another test, it was demonstrated that the source of the long wavelengths are the head and diving waves so that the recovery of low frequencies is limited to the depth of penetration of these seismic waves. The most promising results of this research are presented in Chapter 8. It was shown first that well-log validated waveform inversion, when exposed to errors in the initial wavelet estimation, is badly exposed to wavelet/model cross-talk. The log-validate waveform inversion workflow was modified in order to allow estimating amplitude and phase updates that when applied to the modelled reflectivity and the wavelet, contribute to diminishing the negative effects of a wrongly estimated wavelet. The new workflow was stably applied to field data (CREWES Hussar 2D land data set). The meaningful geological structures recovered through the inversion are

positive signs of this approach.

9.1 Future work

The well-log validated waveform inversion is open to expansion by including migration to angle gathers and updating with multiple elastic parameters. Within the lines of this thesis I have assumed constant density and invert directly for P-wave velocity; however, inverting for density looks like a straight forward step due to the direct link between log-validated waveform inversion with one-way equation migration and impedance inversion. The following is an idea to be developed:

1) Start the inversion with two initial models: one for velocity and another one for density. In the first stage, we iterate allowing the velocity model to be perturbed and keep the density model fixed. 2) After finding convergence to the true velocity model, we run another inversion, this time fixing the velocity model and updating the density model. In this stage, we assume that the reflectivity residual will have information mainly due to density variations, so we calibrate the update direction with a density residual in the well. The final density model is hopefully a better version of the initial model. 3) We can apply step (1) again using the new density model as a starting point in order to refine the velocity model. 4) We may run step (2) again with the refined velocity model.

Another idea is to add an extra forward modelling loop in each iteration in order to invert first for P-wave velocity keeping density fixed, and in the extra loop invert for density keeping the updated velocity model fixed. In this case, we assume that the modelled shots, generated in the extra loop, will produce a reflectivity residual that mainly contains the effect of density variations in the particular frequency band used in the current iteration. The update direction in the first loop is calibrated by using the velocity log. The update direction in the second loop is calibrated by using the density log.

In Chapter 3, I showed that applying a time-integrated wavelet to generate the source

wavefield in the PSPI migration process, produces a similar result than applying impedance inversion to the migrated stack. In future work, I will investigate the integrated wavelet approach to generate the PSPI update direction, avoiding the impedance inversion step. This branch for future research is expected to have advantages over the impedance inversion approach because we do not need to approximate reflectivity by normal-incidence reflection coefficient normalized by dz.

In Chapter 8, a modification of the well-log validated procedure was implemented in order to address amplitude and phase errors due to a wrong estimated wavelet. During the process, a constant-phase seismic data and a stationary wavelet were assumed, which may lead to instabilities in the updated wavelet. I will look into this issue in future work.

Bibliography

Aki, K. and P. G. Richards, 2002, Quantitative seismology.

AlTheyab, A., X. Wang, and G. T. Schuster, 2013, Time-domain incomplete gauss-newton full-waveform inversion of gulf of mexico data, *in* SEG Technical Program Expanded Abstracts 2013, 5175–5179. Society of Exploration Geophysicists.

Bleibinhaus, F., J. A. Hole, T. Ryberg, and G. S. Fuis, 2007, Structure of the California Coast Ranges and San Andreas Fault at SAFOD from seismic waveform inversion and reflection imaging: Journal of Geophysical Research: Solid Earth, **112**.

Brenders, A. and R. Pratt, 2007, Full waveform tomography for lithospheric imaging: results from a blind test in a realistic crustal model: Geophysical Journal International, **168**, 133–151.

Bunks, C., F. M. Saleck, S. Zaleski, and G. Chavent, 1995, Multiscale seismic waveform inversion: Geophysics, **60**, 1457–1473.

Castagna, J. P. and M. Backus, 1993, AVO analysis—Tutorial and review: Offset-dependent reflectivity—Theory and practice of AVO analysis: SEG Investigations in Geophysics, **8**, 3–36.

Chauris, H., M. Noble, and C. Taillander, 2008, Which initial model do we need for full waveform inversion: Presented at the Annual International Meeting.

Chen, Y., H. Chen, K. Xiang, and X. Chen, 2016, Geological structure guided well log interpolation for high-fidelity full waveform inversion: Geophysical Supplements to the Monthly Notices of the Royal Astronomical Society, **207**, 1313–1331.

Chopra, S., 2016, Inversion in depth?: CSEG Recorder, **41**, 34–35.

Claerbout, J. F., 1971, Toward a unified theory of reflector mapping: Geophysics, **36**, 467–481.

Cordsen, A., M. Galbraith, and J. Peirce, 2000, Planning land 3-D seismic surveys: Society of Exploration Geophysicists.

Crase, E., A. Pica, M. Noble, J. McDonald, and A. Tarantola, 1990, Robust elastic nonlinear waveform inversion: Application to real data: Geophysics, **55**, 527–538.

Datta, D. and M. Sen, 2016, Estimating a starting model for full-waveform inversion using a global optimization method: Geophysics, 81: R211–R223, http://doi.org/10.1190/geo2015-0339.1.

Etgen, J., S. H. Gray, and Y. Zhang, 2009, An overview of depth imaging in exploration geophysics: Geophysics, **74**, WCA5–WCA17.

Fatti, J. L., G. C. Smith, P. J. Vail, P. J. Strauss, and P. R. Levitt, 1994, Detection of gas in sandstone reservoirs using avo analysis: A 3-d seismic case history using the geostack technique: Geophysics, **59**, 1362–1376.

Ferguson, R. J. and G. F. Margrave, 1996, A simple algorithm for band-limited impedance inversion: CREWES annual report.

Finkl, C. W., 1988, The encyclopedia of field and general geology: Springer Science & Business Media.

Gao, F., A. Levander, R. G. Pratt, C. A. Zelt, and G.-L. Fradelizio, 2007, Waveform tomography at a groundwater contamination site: Surface reflection data: Geophysics, **72**, G45–G55.

Gauthier, O., 1986, Two-dimensional nonlinear inversion of seismic waveforms: Numerical results: Geophysics, **51**, 1387.

Gazdag, J., 1978, Wave equation migration with the phase-shift method: Geophysics, **43**, 1342–1351.

Gazdag, J. and P. Sguazzero, 1984, Migration of seismic data by phase shift plus interpola-

tion: Geophysics, **49**, 124–131.

Guarido de Andrade, M., 2017, Convergence of a full waveform inversion scheme based on pspi migration and forward modeling-free approximation: procedure and validation: PhD thesis, University of Calgary.

Guitton, A., G. Ayeni, and E. Diaz, 2012, Constrained full-waveform inversion by model reparameterization: Geophysics, **77**.

Henley, D. C., 1999, Coherent noise attenuation in the radial trace domain: Introduction and demonstration: CREWES Research Report, **11**.

Huang, Y. and G. T. Schuster, 2018, Full-waveform inversion with multisource frequency selection of marine streamer data: Geophysical Prospecting, **66**, 1243–1257.

Ikelle, L. T., J. P. Diet, and A. Tarantola, 1986, Linearized inversion of multioffset seismic reflection data in the ω-k domain: Geophysics, **51**, 1266–1276.

Innanen, K. A., 2014, Seismic AVO and the inverse Hessian in precritical reflection full waveform inversion: Geophysical Journal International, **199**, 717–734.

Isaac, J. H. and G. F. Margrave, 2011, Hurrah for Hussar! Comparisons of stacked datal: CREWES Research Report, **23**.

Jackson, D. D., 1972, Interpretation of inaccurate, insufficient and inconsistent data: Geophysical Journal International, **28**, 97–109.

Jaiswal, P., C. A. Zelt, A. W. Bally, and R. Dasgupta, 2008, 2-D traveltime and waveform inversion for improved seismic imaging: Naga Thrust and Fold Belt, India: Geophysical Journal International, **173**, 642–658.

Karimi, P., 2015, Structure-constrained relative acoustic impedance using stratigraphic coordinates: Geophysics, **80**, A63–A67.

Kazei, V., V. Troyan, B. Kashtan, and W. Mulder, 2013, On the role of reflections, refractions and diving waves in full-waveform inversion: Geophysical Prospecting, **61**, 1252–1263.

Kolb, P., F. Collino, and P. Lailly, 1986, Pre-stack inversion of a 1-d medium: Proceedings of the IEEE, **74**, 498–508.

Lailly, P., 1983, The seismic inverse problem as a sequence of before stack migration: SIAM, 206–220.

Lee, J. and C. Shin, 2015, Application of full waveform inversion to real marine dataset, *in* SEG Technical Program Expanded Abstracts 2015, 1080–1085. Society of Exploration Geophysicists.

Lee, K. H. and H. J. Kim, 2003, Source-independent full-waveform inversion of seismic data: Geophysics, **68**, 2010–2015.

Lindseth, R. O., 1979, Synthetic sonic logs—a process for stratigraphic interpretation: Geophysics, **44**, 3–26.

Lines, L. and P. Daley, 2009, The accuracy of dipole sonic logs with implications for synthetic seismograms and wavelet estimation: CREWES Research Report, **21**.

Lines, L. R. and R. T. Newrick, 2004, Fundamentals of geophysical interpretation: Society of Exploration Geophysicists.

Liu, F., L. Guasch, S. A. Morton, M. Warner, A. Umpleby, Z. Meng, S. Fairhead, and S. Checkles, 2012, 3-d time-domain full waveform inversion of a valhall obc dataset, *in* SEG Technical Program Expanded Abstracts 2012, 1–5. Society of Exploration Geophysicists.

Liu, S., X. Meng, and L. Fu, 2016, Source wavelet independent time-domain full waveform inversion (FWI) of cross-hole radar data: Annual International Meeting, IEEE, Geoscience and Remote Sensing Symposium (IGARSS), 2016 IEEE International, 7485–7488.

Ma, Y., D. Hale, B. Gong, and Z. Meng, 2012, Image-guided sparse-model full waveform inversion: Geophysics, **77**, R189–R198.

Malinowski, M., S. Operto, and A. Ribodetti, 2011, High-resolution seismic attenuation imaging from wide-aperture onshore data by visco-acoustic frequency-domain full-waveform inversion: Geophysical Journal International, **186**, 1179–1204.

Margrave, G. F., M. B. Bertram, D. C. Lawton, K. A. Innanen, K. W. Hall, L. Mewhort, and M. Hall, 2011a, The Hussar Low-Frequency Experimentl: CREWES Research Report, **23**.

Margrave, G. F., R. J. Ferguson, and C. M. Hogan, 2010, Full-waveform inversion with wave

equation migration and well control: CREWES Research Report, **22**.

——— 2011b, Full waveform inversion using one-way migration and well calibration.

Margrave, G. F., K. A. Innanen, and M. Yedlin, 2012a, A Perspective on Full-Waveform Inversionl: CREWES Research Report, **24**.

Margrave, G. F., M. P. Lamoureux, and D. C. Henley, 2011c, Gabor deconvolution: Estimating reflectivity by nonstationary deconvolution of seismic data: Geophysics, **76**, W15–W30.

Margrave, G. F., L. Mewhort, T. Phillips, M. Hall, M. B. Bertram, D. C. Lawton, K. Innanen, K. W. Hall, and K. Bertram, 2012b, The hussar low-frequency experiment: CSEG Recorder, **37**, 25–39.

Minkoff, S. E. and W. W. Symes, 1997, Full waveform inversion of marine reflection data in the plane-wave domain: Geophysics, **62**, 540–553.

Mondol, N. H., 2010, Seismic exploration, *in* Petroleum Geoscience, 375–402. Springer.

Mora, P., 1987, Nonlinear two-dimensional elastic inversion of multioffset seismic data: Geophysics, **52**, 1211–1228.

——— 1988, Elastic wave-field inversion of reflection and transmission data: Geophysics, **53**, 750–759.

Nocedal, J. and S. J. Wright, 2006, Line search methods: Numerical optimization, 30–65.

Operto, S., C. Ravaut, L. Improta, J. Virieux, A. Herrero, and P. Dell'Aversana, 2004, Quantitative imaging of complex structures from dense wide-aperture seismic data by multiscale traveltime and waveform inversions: A case study: Geophysical prospecting, **52**, 625–651.

Ostrander, W., 1984, Plane-wave reflection coefficients for gas sands at nonnormal angles of incidence: Geophysics, **49**, 1637–1648.

Paffenholz, J., J. Stefani, B. McLain, and K. Bishop, 2002, Sigsbee_2a synthetic subsalt dataset-image quality as function of migration algorithm and velocity model error: Presented at the Annual International Meeting.

Pan, W., Y. Geng, and K. A. Innanen, 2018, Interparameter trade-off quantification and reduction in isotropic-elastic full-waveform inversion: synthetic experiments and Hussar land data set application: Geophysical Journal International, **213**, 1305–1333.

Pan, W., K. Innanen, and G. Margrave, 2014a, A comparison of different scaling methods for least-squares migration/inversion.

——— 2014b, Full waveform inversion with phase encoded deconvolution imaging condition.

Pica, A., J. Diet, and A. Tarantola, 1990, Nonlinear inversion of seismic reflection data in a laterally invariant medium: Geophysics, **55**, 284–292.

Plessix, R.-E., G. Baeten, J. W. de Maag, M. Klaassen, Z. Rujie, and T. Zhifei, 2010, Application of acoustic full waveform inversion to a low-frequency large-offset land data set, *in* SEG Technical Program Expanded Abstracts 2010, 930–934. Society of Exploration Geophysicists.

Plessix, R.-E., G. Baeten, J. W. de Maag, F. ten Kroode, and Z. Rujie, 2012, Full waveform inversion and distance separated simultaneous sweeping: A study with a land seismic data set: Geophysical Prospecting, **60**, 733–747.

Pratt, R. G., 1999, Seismic waveform inversion in the frequency domain, Part 1: Theory and verification in a physical scale model: Geophysics, **64**, 888–901.

Pratt, R. G., C. Shin, and G. Hick, 1998, Gauss–Newton and full Newton methods in frequency–space seismic waveform inversion: Geophysical Journal International, **133**, 341–362.

Prieux, V., G. Lambaré, S. Operto, and J. Virieux, 2013, Building starting models for full waveform inversion from wide-aperture data by stereotomography: Geophysical Prospecting, **61**, 109–137.

Ravaut, C., S. Operto, L. Improta, J. Virieux, A. Herrero, and P. Dell'Aversana, 2004, Multiscale imaging of complex structures from multifold wide-aperture seismic data by frequency-domain full-waveform tomography: Application to a thrust belt: Geophysical Journal International, **159**, 1032–1056.

Ray, A., A. Sekar, G. M. Hoversten, and U. Albertin, 2016, Frequency domain full waveform elastic inversion of marine seismic data from the Alba field using a Bayesian trans-dimensional algorithm: Geophysical Journal International, **205**, 915–937.

Romahn, S., M. Guarido, and K. Innanen, 2018, Comparison between RTM gradient and PSPI gradient in the process of FWI: CSEG Convention Abstracts 2018.

Romahn, S. and K. A. Innanen, 2017a, Iterative modeling, migration, and inversion: Evaluating the well-calibration technique to scale the gradient in the ful waveform inversion process: SEG Technical Program Expanded Abstracts 2017, 1583–1587.

——— 2017b, Iterative modelling, migration and inversion (IMMI): the role of well calibration in the context of high geological complexity: CSEG Convention Abstracts 2017.

Russell, B. H., 1988, Introduction to seismic inversion methods: Society of Exploration Geophysicists.

Sheriff, R. E., 2002, Encyclopedic dictionary of applied geophysics: Society of exploration geophysicists.

Shin, C., S. Jang, and D.-J. Min, 2001a, Improved amplitude preservation for prestack depth migration by inverse scattering theory: Geophysical prospecting, **49**, 592–606.

Shin, C., K. Yoon, K. J. Marfurt, K. Park, D. Yang, H. Y. Lim, S. Chung, and S. Shin, 2001b, Efficient calculation of a partial-derivative wavefield using reciprocity for seismic imaging and inversion: Geophysics, **66**, 1856–1863.

Shipp, R. M. and S. C. Singh, 2002, Two-dimensional full wavefield inversion of wide-aperture marine seismic streamer data: Geophysical Journal International, **151**, 325–344.

Shuey, R., 1985, A simplification of the zoeppritz equations: Geophysics, **50**, 609–614.

Soubaras, R. and P. Whiting, 2011, Variable depth streamer—the new broadband acquisition system, *in* SEG Technical Program Expanded Abstracts 2011, 4349–4353. Society of Exploration Geophysicists.

Tarantola, A., 1984, Inversion of seismic reflection data in the acoustic approximation: Geophysics, **49**, 1259–1266.

——— 1987, Inversion of travel times and seismic waveforms, *in* Seismic Tomography, 135–157. Springer.

Vigh, D., J. Kapoor, and H. Li, 2011, Full-waveform inversion application in different geological settings, *in* SEG Technical Program Expanded Abstracts 2011, 2374–2378. Society of Exploration Geophysicists.

Vigh, D., E. W. Starr, and J. Kapoor, 2009, Developing earth models with full waveform inversion: The Leading Edge, **28**, 432–435.

Virieux, J. and S. Operto, 2009, An overview of full-waveform inversion in exploration geophysics: Geophysics, **74**, WCC1–WCC26.

Wang, K., J. R. Krebs, D. Hinkley, and A. Baumstein, 2009, Simultaneous full-waveform inversion for source wavelet and earth model, *in* SEG Technical Program Expanded Abstracts 2009, 2537–2541. Society of Exploration Geophysicists.

Warner, M., T. Nangoo, N. Shah, A. Umpleby, and J. Morgan, 2013, Full-waveform inversion of cycle-skipped seismic data by frequency down-shifting, *in* SEG Technical Program Expanded Abstracts 2013, 903–907. Society of Exploration Geophysicists.

Waters, K. H., 1987, Reflection seismology: A tool for energy resource exploration: Wiley New York.

Wenyong, P., G. Margrave, and K. Innanen, 2013, On the role of the deconvolution imaging condition in full waveform inversion: CREWES Research Report, **25**, 72–1.

Yang, P., J. Gao, and B. Wang, 2015, A graphics processing unit implementation of time-domain full-waveform inversion: Geophysics, **80**, F31–F39.

Yilmaz, Ö., 2001, Seismic data analysis: Processing, inversion, and interpretation of seismic data: Society of exploration geophysicists.

Youzwishen, C. F. and G. F. Margrave, 1999, Finite difference modeling of acoustic waves in matlab: the 11th Annual Research Report of the CREWES Project.

Yu, H. and S. M. Hanafy, 2014, An application of multiscale early arrival waveform inversion to shallow seismic data: Near Surface Geophysics, **12**, 549–557.

Zhang, Y., S. Xu, N. Bleistein, and G. Zhang, 2007, True-amplitude, angle-domain, common-image gathers from one-way wave-equation migrations: Geophysics, **72**, S49–S58.

Zhou, C., G. T. Schuster, S. Hassanzadeh, and J. M. Harris, 1997, Elastic wave equation traveltime and waveform inversion of crosswell data: Geophysics, **62**, 853–868.